Renormalized nucleon isovector couplings from 2+1 flavor lattice QCD

著者	Tsukamoto Natsuki
学位授与機関	Tohoku University
学位授与番号	11301甲第19010号
URL	http://hdl.handle.net/10097/00128444

Ph.D Thesis

Renormalized nucleon isovector couplings from 2+1 flavor lattice QCD

(**2+1 フレーバー格子 QCD による**
繰り込まれた陽子と中性子の結合定数の研究)

塚本　夏基

Department of Physics
Graduate School of Science
Tohoku University
2019

ABSTRACT

Background

The nucleon has been investigated in various aspects for a long time since Rutherford had discovered the proton about 100 years ago. Nowadays the nucleon is known to be composed of quarks and gluons that are described by Quantum Chromodynamics (QCD in short), the first principle of the strong interaction. This implies that any features of the nucleon can be theoretically understood based on QCD. However, in practice, it is difficult to calculate the nucleon structure in QCD analytically. Therefore numerical simulations are actively performed though realistic numerical simulations have been only recently achieved. In this sense, the nucleon structure is not yet well understood theoretically.

The nucleon scalar and tensor couplings (g_S and g_T) also should play important roles to constrain the limit of non-standard interactions mediated by undiscovered gauge bosons in the scalar and tensor channels. Furthermore, the tensor coupling has the same transformation properties under P and T discrete symmetries as the electric dipole moment (EDM) current. Thus the nucleon tensor isovector-coupling is also an important information regarding the size of neutron EDM.

The scalar and tensor isovector-couplings are so far not accessible in experiment. Although lattice determination of the scalar and tensor isovector-couplings have recently performed by several groups, the reliable value is given by a single group. Therefore further comprehensive studies of the nucleon isovector-couplings are still needed.

Content

The main purpose of this thesis is to evaluate the scalar and tensor couplings using domain-wall fermions (Chap. 4) and Wilson-clover fermions (Chap. 5). Our simulations using domain-wall fermions (DWFs) are performed at two different lattice spacings so that we can eliminate lattice artifacts from our lattice results. However, our DWF simulations are not performed at the physical point. Therefore there are a systematic uncertainties stemming from the chiral extrapolation.

On the other hand, our simulations using Wilson-clover fermions are performed at the physical point on a (10.8 fm)^4 lattice at a single lattice spacing. Because of a huge physical volume, the statistical uncertainties on our results are significantly suppressed. We then obtain the precise value of the nucleon coupling constants from the latter simulations without the chiral extrapolation. Although we cannot eliminate the systematic uncertainty due to the presence of the lattice discretization, a typical magnitude of this uncertainty might be estimated in the former simulations using domain-wall fermions. In this sense, two simulations are complementary to each other.

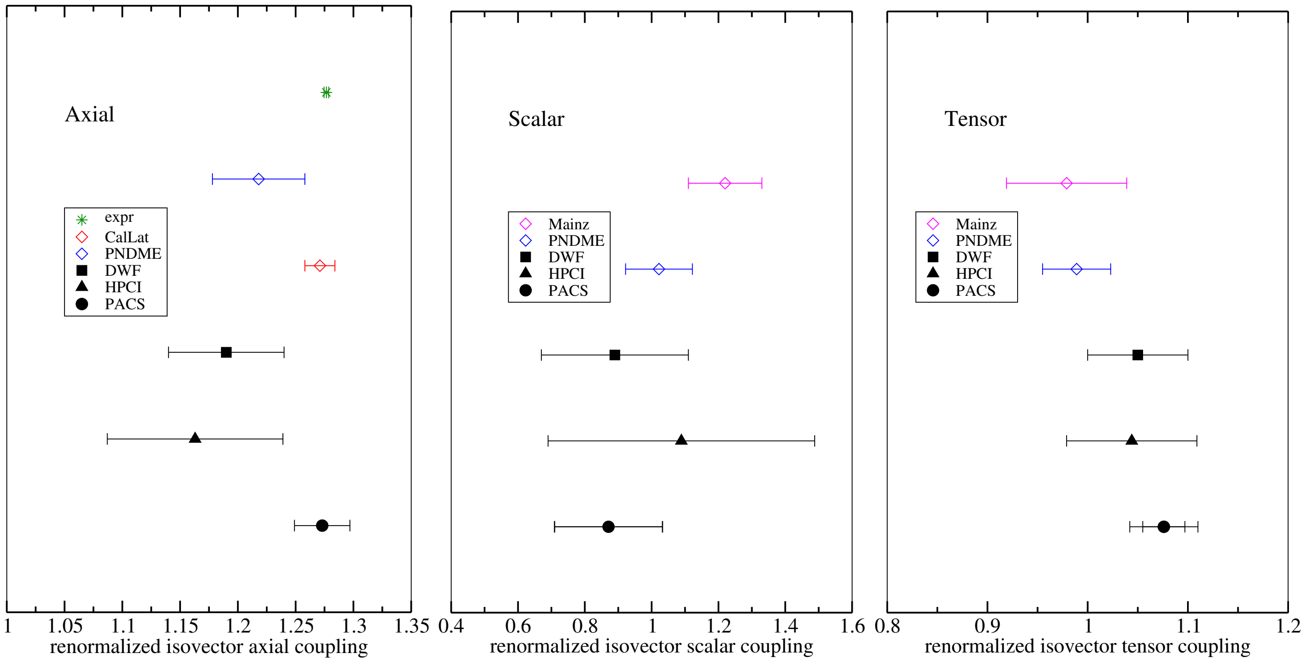

Fig. 1: Our results from the DWF (black square), HPCI (black triangle) and PACS10 (black circle) ensembles compared with the results from CalLat Collaboration (red diamond), PNDME Collaboration (blue diamond) and Mainz group (purple diamond). The inner error-bars for the result from the PACS10 ensembles represent the statistical uncertainties while the outer error-bars present the combined uncertainties.

Result

We summarize all obtained results of the isovector coupling constants in both cases of DWFs and the Wilson-clover fermions together with our previous results calculated with the HPCI configurations in Fig. 1. All our result (filled symbols) are barely consistent with the other group (open symbols) studies. It is worth noting that g_A measured with the PACS10 configuration is consistent with the experimental value within a few percent precision. Therefore it is expected that the present calculations in the scalar and tensor channels also accurately predict their nucleon couplings. Using our obtained values of the scalar and tensor coupling constants, we also estimate the impact of our results in the context of the new physics research in this thesis.

Contents

Chapter 1

Introduction

Ordinary matter is made of subatomic particles such as electrons, protons and neutrons. The latter two particles are regarded as two states of a single particle called nucleon. The nucleon has been investigated in various aspects for a long time since Rutherford had discovered the proton about 100 years ago [1]. Nowadays the nucleon is known to be composed of quarks and gluons that are described by Quantum Chromodynamics (QCD in short), the first principle of the strong interaction. This implies that any features of the nucleon can be theoretically understood based on QCD. However, in practice, it is difficult to calculate the nucleon structure in QCD analytically. Therefore numerical simulations are actively performed though realistic numerical simulations have been only recently achieved. In this sense, the nucleon structure is not yet well understood theoretically.

The standard model is said to be a triumph of modern physics and can explain almost all experimental results. On the other hand, the nuclear structure is not well understood in the framework of the standard model. Bridging a gap between high energy physics and nuclear physics should be worth exploring.

1.1 Current status of the measurement of nucleon couplings

Future and current precision β-decay measurements with cold and ultracold neutrons provide us an opportunity to study the sensitivity of the nucleon isovector matrix elements to new physics beyond the standard model (BSM). The neutron life-time puzzle associated with the nucleon axial coupling (g_A) [2] is one of such examples. The nucleon scalar and tensor couplings (g_S and g_T) should play important roles to constrain the limit of non-standard interactions mediated by undiscovered gauge bosons in the scalar and tensor channels if the BSM contributions are present [3, 4]. Especially the nucleon scalar isovector-coupling, which is related to the mass difference between the light quarks, is a phenomenologically interesting quantity [5]. On the other hand, the tensor coupling has the same transformation properties under P and T discrete symmetries as the electric dipole moment (EDM) current. Thus the nucleon tensor isovector-coupling is also an important information regarding the size of neutron EDM.

Although the vector and axial isovector-couplings (g_V and g_A) are well measured in both experiment and lattice QCD, the scalar and tensor isovector-couplings are so far not accessible in experiment. On the other hand, lattice determination of the scalar and tensor isovector-couplings have recently performed by several groups [6, 7, 8]. As shown in Fig. 1.1, the reliable value is given by a single group (PNDME Collaboration) [6] and their calculation had been performed with the mixed action simulations using the Wilson-clover valence quarks on the asgtad-improved gauge configurations with the highly improved staggered sea quarks (HISQ). This implies that their lattice QCD simulations are *not* fully dynamical one, but rather *partially quenched* one since they used the different action for the sea and valence quarks. Moreover they used the fourth-root-trick for reducing unwanted

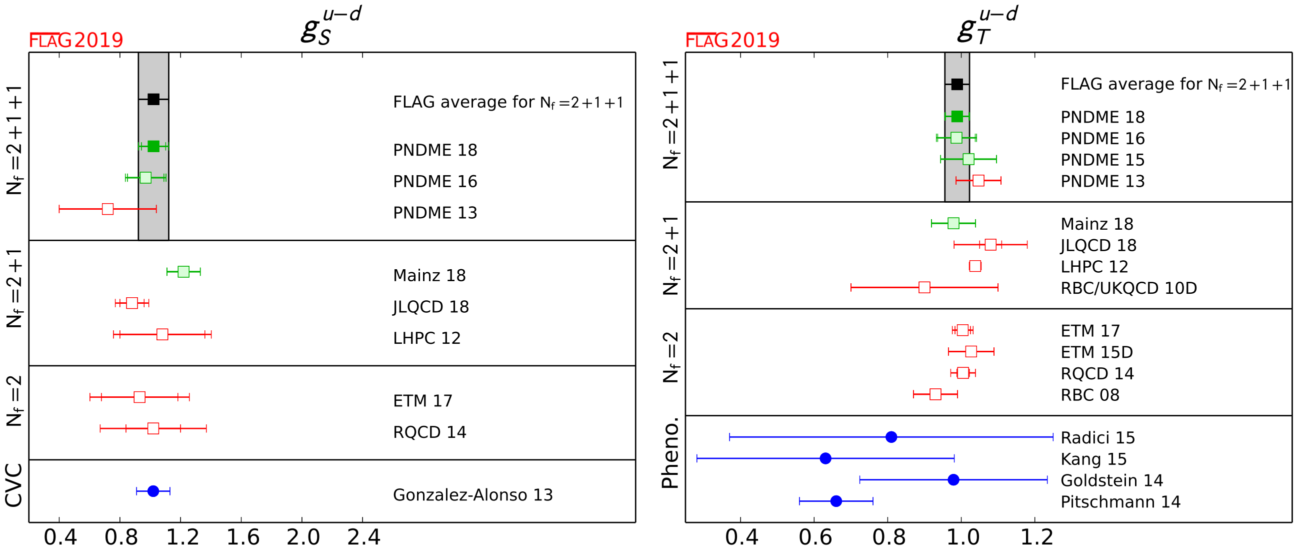

Fig. 1.1: The summarized isovector nucleon couplings including the phenomenological extracted values in FLAG Review 2019 [11].

degrees of freedom with the staggered quarks, which has the theoretical issue as summarized in [9, 10]. Even if we could not achieve to overwhelm the present precisions given by the PNDME Collaboration, it is worth to reproduce their results in *fully dynamical lattice QCD simulations* using more realistic fermion actions.

1.2 Nucleon matrix element and current

In general the isovector nucleon matrix elements in the vector (V), axial (A), scalar (S), pseudoscalar (P) and tensor (T) channels are expressed by

$$\langle p|V_\mu^+(x)|n\rangle = \overline{u}_p \left[\gamma_\mu F_V(q^2) + \sigma_{\mu\nu} q_\nu F_T(q^2)\right] u_n e^{iq\cdot x} \tag{1.1}$$

$$\langle p|A_\mu^+(x)|n\rangle = \overline{u}_p \left[\gamma_\mu \gamma_5 F_A(q^2) + i q_\mu F_P(q^2)\right] u_n e^{iq\cdot x} \tag{1.2}$$

$$\langle p|S^+(x)|n\rangle = \overline{u}_p \left[G_S(q^2)\right] u_n e^{iq\cdot x} \tag{1.3}$$

$$\langle p|P^+(x)|n\rangle = \overline{u}_p \left[\gamma_5 G_P(q^2)\right] u_n e^{iq\cdot x} \tag{1.4}$$

$$\langle p|T_{\mu\nu}^+(x)|n\rangle = \overline{u}_p \left[\sigma_{\mu\nu} G_T(q^2) + \left(\gamma_\mu q_\nu - \gamma_\nu q_\mu\right) F_{2,T}(q^2) + i\left(\sigma_{\mu\alpha} q_\nu - \sigma_{\nu\alpha} q_\mu\right) q_\alpha F_{3,T}(q^2)\right] u_n e^{iq\cdot x} \tag{1.5}$$

where V^+, A^+, S^+, P^+, T^+ are the quark charged (off-diagonal) currents $\overline{u}(x)\Gamma_O d(x)$ with the respective Dirac matrices Γ_O and $F_O, G_O, O = V, A, S, P, T$ are the form factors associated to the currents [12]. Especially, the value of the form factors at $q^2 = 0$ are associated to the net charge of the corresponding currents. For the vector and axial channels as the isovector vector charge and axial charge, which are important quantities in the β-decay process, we get

$$F_V(0) = g_V \qquad \text{and} \qquad F_A(0) = g_A. \tag{1.6}$$

Similarly one can define the scalar, pseudoscalar and tensor charge as

$$G_S(0) = g_S \qquad G_P(0) = g_P \qquad G_T(0) = g_T. \tag{1.7}$$

In this study, we focus on above charges rather than their form factors.

Under the exact isospin symmetry, we derive the relation between the off-diagonal current and the diagonal current,

$$\langle p|O^+(x)|n\rangle = \langle p|O^3(x)|p\rangle - \langle n|O^3(x)|n\rangle, \tag{1.8}$$

where the diagonal current is defined by

$$O^3 = \overline{u}(x)\Gamma_O u(x) - \overline{d}(x)\Gamma_O d(x). \tag{1.9}$$

Here we recall that the following relation between proton and neutron matrix elements

$$\langle n|\overline{u}(x)\Gamma_O u(x)|n\rangle = \langle p|\overline{d}(x)\Gamma_O d(x)|p\rangle \qquad \langle p|\overline{u}(x)\Gamma_O u(x)|p\rangle = \langle n|\overline{d}(x)\Gamma_O d(x)|n\rangle \tag{1.10}$$

under the exact isospin symmetry. For convenience, we write $g_O^q, q = u, d$ as the flavor contribution of the proton charge associated with the proton matrix element $\langle p|\overline{q}(x)\Gamma_O q(x)|p\rangle$.

These relation leads a simple connection between the weak(isovector) couplings and proton related charges

$$g_O = g_O^u - g_O^d. \tag{1.11}$$

Recall that for the vector $g_V = 1$ is satisfied under the exact isospin symmetry.

1.3 Remarkable phenomena

In this section, we focus on phenomena related to the nucleon charges rather than the individual features of g_A, g_S, g_T.

1.3.1 Neutron decay and BSM contribution

Among the various nucleon charges, the only axial charge is well-known experimentally. Although the axial charge dominates the weak decay of the neutron, there is no reason to forbid contributions from the other channels. In the useful notation [13], the effective Lagrangian density for the $d \to u$ transition is written in

$$\begin{aligned}\mathcal{L} = -\frac{G_F^{(0)}}{\sqrt{2}}\left(1+\epsilon_L+\epsilon_R\right)\Big[&\bar{l}\gamma_\mu(1-\gamma_5)\nu\cdot\overline{u}\left(\gamma^\mu-(1-2\epsilon_R)\gamma^\mu\gamma_5\right)d\\ &+\bar{l}(1-\gamma_5)\nu\cdot\overline{u}\left(\epsilon_S-\epsilon_P\gamma_5\right)d+\epsilon_T\bar{l}\gamma_\mu\gamma_\nu(1-\gamma_5)\nu\cdot\overline{u}\gamma^\mu\gamma^\nu(1-\gamma_5)d\Big].\end{aligned} \tag{1.12}$$

where G_F^0 is the Fermi constant determined by the mass of the weak boson.

- ϵ_L is further correction for the left-handed coupling.

- ϵ_R is the correction for the right-handed coupling.
- $\epsilon_{S,P,T}$ is the correction for the scalar, pseudoscalar or tensor type couplings mediated by the unknown gauge boson. $\epsilon_{S,P,T}$ is the inverse mass of the undiscovered gauge boson.

For convenience, we use the Lee-Yang parameters [14],

$$\overline{C}_V + \overline{C}'_V = 2g_V(1+\epsilon_L+\epsilon_R) \qquad \overline{C}_V - \overline{C}'_V = 2g_V(\tilde{\epsilon}_L+\tilde{\epsilon}_R) \tag{1.13}$$

$$\overline{C}_A + \overline{C}'_A = -2g_A(1+\epsilon_L-\epsilon_R) \qquad \overline{C}_A - \overline{C}'_A = 2g_A(\tilde{\epsilon}_L-\tilde{\epsilon}_R) \tag{1.14}$$

$$\overline{C}_S + \overline{C}'_S = 2g_S\epsilon_S \qquad \overline{C}_S - \overline{C}'_S = 2g_S\tilde{\epsilon}_S \tag{1.15}$$

$$\overline{C}_P + \overline{C}'_P = 2g_P\epsilon_P \qquad \overline{C}_P - \overline{C}'_P = -2g_P\tilde{\epsilon}_P \tag{1.16}$$

$$\overline{C}_T + \overline{C}'_T = 8g_T\epsilon_T \qquad \overline{C}_T - \overline{C}'_T = 8g_T\tilde{\epsilon}_T \tag{1.17}$$

where $C_i = \frac{G_F^{(0)}V_{ud}}{\sqrt{2}}\overline{C}_i$ and $\tilde{\epsilon}_i$ is negligible because of involving right-handed neutrinos [15]. In this definition, C'_i is nothing but C_i and the difference $C_i - C'_i$ is finite only if ϵ parameters are constraint by the various experiments involving $d \to u$ process. Especially in $n \to p$ process, the combinations of the nucleon couplings g_O and parameters ϵ_i are regulated by the most recent limit [15] as below

$$\begin{pmatrix} |C_V| \\ C_A/C_V \\ C_S/C_V \\ C_T/C_A \end{pmatrix} = \begin{pmatrix} 0.98595(34)G_F/\sqrt{2} \\ -1.2728(17) \\ 0.0014(12) \\ 0.0020(22) \end{pmatrix} \qquad \rho = \begin{pmatrix} 1.00 & & & \\ 0.08 & 1.00 & & \\ 0.94 & 0.08 & 1.00 & \\ -0.32 & 0.85 & -0.31 & 1.00 \end{pmatrix}, \tag{1.18}$$

where ρ is the normalized covariant matrix defined as $\rho_{ij} = C_{ij}/\sqrt{C_{ii}C_{jj}}$ using the covariant matrix C_{ij}.

1.3.2 Isospin breaking and scalar charge

The vector and axial current conservation laws are given by

$$\partial^\mu V^+_\mu(x) = (m_u - m_d)\, S^+(x) \tag{1.19}$$

$$\partial^\mu A^+_\mu(x) = (m_u + m_d)\, P^+(x). \tag{1.20}$$

Together with these conservation laws and the explicit form of the form factors, we derive the relation between the quark mass difference and the nucleon mass difference [5]

$$\delta m_q G_S(q^2) = \delta M_N^{\rm QCD} F_V(q^2) + \frac{q^2}{2M_N}F_S(q^2) \tag{1.21}$$

$$\overline{m}_q G_P(q^2) = M_N F_A(q^2) + \frac{q^2}{4M_N}F_P(q^2), \tag{1.22}$$

where $\delta m_q = m_u - m_d$, $\overline{m}_q = m_u + m_d$ and $\delta M_N^{\rm QCD}$ is the mass difference between the proton and the neutron without the QED effect. The latter equation is also known as the Goldberger-Triemann relation. At $q^2 = 0$, we

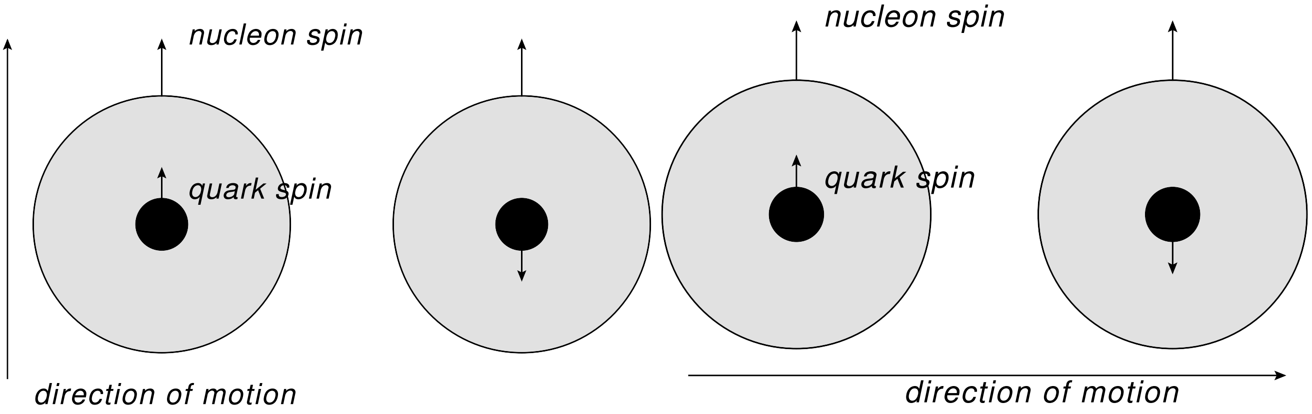

Fig. 1.2: The image of the quark helicity(left) and transversity(right) distribution function.

hold

$$g_S = \frac{\delta M_N^{QCD}}{\delta m_q} g_V, \qquad g_P = \frac{M_N}{\overline{m}_q} g_A. \tag{1.23}$$

1.3.3 Distribution functions and nucleon charge

The quark as the fragment of the proton is characterized by three distribution functions, namely $q(x)$, $\Delta q(x)$ and $\delta q(x)$ as a function of the momentum fraction x defined as the ratio between the momentum carried by the quark and the proton net momentum (by definition, $0 < x < 1$).

- The quark distribution function $q(x)$ is the probability density function of the quark with the momentum fraction x.
- The helicity distribution functions $\Delta q^{\uparrow}(x), \Delta q^{\downarrow}(x)$ are the probability density functions of the polarized quark with the momentum fraction x as illustrated on the left panel of Fig. 1.2.
- The transversity distribution functions $\delta q^{\rightarrow}(x), \delta q^{\leftarrow}(x)$ are the probability density functions of the transverse polarized quark with the momentum fraction x as illustrated on the right panel of Fig. 1.2.

The difference between the helicity and transversity distribution functions are schematically depicted in Fig. 1.2. The helicity distribution function is defined as the probability density function of the quark which is polarized in the direction of the nucleon motion while the momentum distribution function is defined as the probability density function of the quark which is polarized in the perpendicular direction of the nucleon motion. By definition, the quark distribution function is given by

$$q(x) = \Delta q^{\uparrow}(x) + \Delta q^{\downarrow}(x), \qquad q(x) = \delta q^{\leftarrow}(x) + \delta q^{\rightarrow}(x). \tag{1.24}$$

We also define

$$\Delta q(x) = \Delta q^{\uparrow}(x) - \Delta q^{\downarrow}(x), \qquad \delta q(x) = \delta q^{\leftarrow}(x) - \delta q^{\rightarrow}(x). \tag{1.25}$$

Integrating the distribution function over x, we obtain the total quark number and total quark spin $\Delta\Sigma$.

$$3 = \int_0^1 dx \sum_{q=u,d,s,\ldots} q(x), \qquad \Delta\Sigma = \int_0^1 dx \sum_{q=u,d,s,\ldots} \Delta q(x) \tag{1.26}$$

where $\Delta\Sigma$ partly contributes the total spin of the nucleon J as

$$J = \frac{1}{2}\left(\Delta\Sigma + \Delta G + \Delta L\right). \tag{1.27}$$

Here ΔG, ΔL denote contributions from gluons and the relative angular momentum respectively. If these contributions are negligible, we obtain $\Delta\Sigma = 1$. Moreover the axial and tensor charge is given as the zeroth order moment of the helicity and transversity distribution functions.

$$g_A^q = \int_0^1 dx \Delta q(x) \qquad g_T^q = \int_0^1 dx \delta q(x) \tag{1.28}$$

$$g_T = \langle 1 \rangle_{\delta u - \delta d} = \int_0^1 dx \left(\delta u(x) - \delta d(x)\right) \tag{1.29}$$

Recent semi-inclusive deep inelastic scattering (SIDIS) experiments [16, 17, 18] give us the knowledge about the quark distribution functions including δq. However the tensor charge can be phenomenologically evaluated using the above relation, the phenomenological value of g_T is not consistent with the result from the lattice QCD in general, while the results from the lattice QCD are consistent with each others [11].

Compared with the quark model

Assuming the SU(6) quark model, we obtain the isovector axial coupling $g_A = \frac{5}{3} \approx 1.66$ [19] which is barely consistent with the experimental value $g_A = 1.2732(23)$ [20]. The nucleon isoscalar coupling $g_A^{\text{isoscalar}} = g_A^u + g_A^d$ is also predicted to be unity [19] corresponding to $\Delta\Sigma = 1$ while the phenomenological extraction as the sum of the quark spin is below 0.5 [21]. The difference between the naive estimations and the experimental values is mainly originated from assuming the quark model assumption where all quantum corrections including gluons are neglected. In the case of the vector current, g_V does not receive any quantum correction exceptionally because of the conservation of the vector current. In other words, the charge in other channels should be evaluated in the fully quantum approach.

1.3.4 Anomalous magnetic moment and quark EDM

Anomalous magnetic moment

The quark is believed to be a point-like Dirac particle having the magnetic moment $\frac{e_q}{2m_q}$ without the QED correction where e_q denotes the electric charge of the quark. If the quark has substructure, there is a "anomalous" part of quark magnetic moment as well. The the quark anomalous magnetic moment may couple to the electromagnetic field $F_{\mu\nu}$ as

$$\mathcal{L}_{\text{AMDM}} = \frac{1}{4} \sum_{q=u,d,s\cdots} \kappa_q \bar{q} \gamma_\mu \gamma_\nu q F^{\mu\nu} \tag{1.30}$$

where $F_{\mu\nu} = \partial_\mu A_\nu - \partial_\nu A_\mu$ is the field strength and κ_q denotes the anomalous magnetic moment of quark. The anomalous contributions to the nucleon magnetic moment can be evaluated to be $\sum_q \kappa_q g_T^q$. In practice, it is hard to evaluate κ_q because we cannot distinguish the intrinsic and anomalous contributions to the nucleon magnetic moment within the current precision.

Quark EDM

In one of the BSM scenario, the quark has the non-vanishing electric dipole moment which couples to the electromagnetic field through the following interaction

$$\mathcal{L}_{\mathrm{EDM}} = \frac{1}{4} \sum_{q=u,d,s\cdots} d_q \bar{q} \gamma_5 \gamma_\mu \gamma_\nu q F^{\mu\nu}, \tag{1.31}$$

which is proportional to the intrinsic electric dipole moment of the quark d_q. As similar as the case of the magnetic moment, the contribution to nucleon EDM [*1] is given by $d_n = d_u g_T^d + d_d g_T^u + d_s g_T^s$ for the neutron and $d_p = d_u g_T^u + d_d g_T^d + d_s g_T^s$ for the proton. It is worth mentioning that d_p and d_n can not be estimated without knowledge for each tensor coupling for a given flavor. The experimental bound is estimated by $d_n < 2.9 \times 10^{-26} e\mathrm{cm}$ [22] and $d_p < 2.1 \times 10^{-25} e\mathrm{cm}$ [20] while the other contributions such as the θ-vacuum [23] or the chromo-magnetic coupling [24] are also possible.

1.4 Contents

The main purpose of this thesis is to evaluate the scalar and tensor couplings and to estimate the impacts of these couplings with respects of the research of the new physics. Firstly we will briefly summarize the lattice and continuum theory of QCD in Chap. 2. We then will discuss the renormalization in lattice QCD in Chap. 3.

Next Chap. 4 and 5, we will show some results from 2+1 lattice QCD simulations using domain-wall fermions (Chap. 4) and Wilson-clover fermions (Chap. 5). Our simulations using domain-wall fermions (DWFs) are performed at two different lattice spacings so that we can eliminate lattice artifacts from our lattice results. However, our DWF simulations are not performed at the physical point. Therefore there are a systematic uncertainties stemming from the chiral extrapolation.

On the other hand, our simulations using Wilson-clover fermions are performed at the physical point on a $(10.8\mathrm{fm})^4$ lattice at a single lattice spacing. Because of a huge physical volume, the statistical uncertainties on our results are significantly suppressed. We then obtain the precise value of the nucleon coupling constants from the latter simulations without the chiral extrapolation. Although we cannot eliminate the systematic uncertainty due to the presence of the lattice discretization, a typical magnitude of this uncertainty might be estimated in the former simulations using domain-wall fermions. In this sense, two simulations are complementary to each other.

We then will estimate the impact of our results in the context of the new physics research in Chap. 6. Chap. 7. is devoted to summary.

[*1] Here, heavy quark contributions are ignored

Chapter 2

Lattice QCD

The nucleon is composed of three valence quarks interacting with gluons. Therefore, the nucleon structure strongly depends on the interplay between quarks and gluons. In other words, the physical quantity of the nucleon structure that depends on the quark degrees of freedom are highly influenced by presence of gluons since the gauge coupling between quarks and gluons become very strong at low energies.

The fundamental theory of the interaction between quarks and gluons is known as Quantum Chromodynamics (QCD in short) which is defined as the non-Abelian SU(3) gauge theory. Although at a glance QCD is quite simply formulated, it is difficult to study the nucleon structure based only on the analytical calculation using the perturbation theory.

In this chapter, we briefly review QCD and then introduce lattice QCD method which allows us to perform non-perturbative and numerical QCD calculations.

2.1 Quantum Chromodynamics

The QCD lagrangian density is composed of two sectors,

$$\mathcal{L}_{\rm QCD}(x) = \mathcal{L}_Q(x) + \mathcal{L}_G(x), \tag{2.1}$$

where $\mathcal{L}_Q(x)$ represents the quark sector, while $\mathcal{L}_G(x)$ represents the gluon sector. We first focus on the quark sector

$$\mathcal{L}_Q(x) = \sum_f \overline{q}_{i,f}(x)(iD^\mu\gamma_\mu - M)q_{i,f}(x), \tag{2.2}$$

which represents the quark kinetic term that contains the gauge interaction through the covariant derivative D_μ. Here f denotes the flavor index, while i denotes the color degrees of freedom with the SU(3) gauge symmetry. Since the quark fields transform in the fundamental representation under the SU(3) gauge transformation, i runs from 1 to 3. The covariant derivative is defined by

$$D_\mu = \partial_\mu - igA^a_\mu(x)T^a, \tag{2.3}$$

which acts on the quark fields as

$$D_\mu q_i(x) = \partial_\mu q_i(x) - igA^a_\mu(x)(T^a)_{ij}q_j(x), \tag{2.4}$$

where T^a_{ij} is the generator of SU(3) Lie group and a runs from 1 to 8. The gluon sector is given by

$$\mathcal{L}_G(x) = -\frac{1}{4}F^{\mu\nu a}F^a_{\mu\nu} \tag{2.5}$$

where the field strength tensor $F^a_{\mu\nu}$ is defined by

$$\begin{aligned} F^a_{\mu\nu}T^a &= \frac{i}{g}[D_\mu, D_\nu] && (2.6)\\ &= \partial_\mu A^a_\nu T^a - \partial_\nu A^a_\mu T^a - ig[T^a, T^b]A^a_\mu A^b_\nu. && (2.7) \end{aligned}$$

Next one can easily confirm that the lagrangian density $\mathcal{L}_{\mathrm{QCD}}(x)$ is invariant under the following local gauge transformation for quark fields

$$q_i(x) \to q'_i(x) = U_{ij}(x)q_j(x) \tag{2.8}$$

and for gluon fields

$$A^a_\mu(x)T^a \to A'^a_\mu(x)T^a = U(x)A^a_\mu(x)T^aU^{-1}(x) - \frac{i}{g}U(x)\partial_\mu U^{-1}(x), \tag{2.9}$$

where the gauge transformation function $U(x)$ is given by

$$U(x) = \exp\left(-ig\theta^a(x)T^a\right) \tag{2.10}$$

where $\theta^a(x)$ is an arbitrary “gauge angle”. Recall that the quark fields transform in the fundamental representation of SU(3) Lie group, while the gauge fields transform in the adjoint representation.

Although a theory with this classical lagrangian should be quantized in order to evaluate the quantum expectation value, we follow the path integral formulation quantization approach in Ref. [25]. The expectation value of some observable $\mathcal{O}$ is schematically represented as

$$\langle\mathcal{O}[q,\overline{q},A_\mu]\rangle = \frac{\int[\mathcal{D}\overline{q}\mathcal{D}q\mathcal{D}A_\mu]\mathcal{O}[q,\overline{q},A_\mu]\exp\left(i\int d^4x\mathcal{L}_{\mathrm{QCD}}\right)}{Z} \tag{2.11}$$

with

$$Z = \int[\mathcal{D}\overline{q}\mathcal{D}q\mathcal{D}A_\mu]\exp\left(i\int d^4x\mathcal{L}_{\mathrm{QCD}}\right), \tag{2.12}$$

which represents the partition function of QCD. In this formulation, the expectation value is given as the functional integration over the quark and gluon fields, which are the Grassmann- or classical- valued functions of the space-time.

2.2 Lattice formulation

Although the path integral formulation of the quantum field theory looks similar to the partition function in the quantum statistical physics, there are some difficulties to perform numerical computation for the following three reasons.

- fermionic variables in the action
- rapidly oscillating term
- uncountably infinite degrees of freedom

The problem indicated in the first point is overcome by integration over the fermionic variables. A possible solution for the second and third problems is that the gauge theory is formulated on the lattice in the Euclidean space-time.

2.2.1 Wick rotation

The action is given by

$$S_{\mathrm{QCD}}[\overline{q}, q, A_\mu] = \int d^4x \mathcal{L}_{\mathrm{QCD}}[\overline{q}, q, A_\mu], \tag{2.13}$$

which should be real-valued. Thus the expectation value of the observable $\mathcal{O}$

$$\langle \mathcal{O} \rangle = \int [\mathcal{D}\overline{q}\mathcal{D}q\mathcal{D}A_\mu]\mathcal{O}[\overline{q}, q, A_\mu] \exp\left(iS_{\mathrm{QCD}}\right)/Z, \tag{2.14}$$

which can not be evaluated in the probabilistic way due to the rapid oscillating term $\exp\left(iS_{\mathrm{QCD}}\right)$. In order to regularize this oscillation, we use the analytic continuation with respect to x_0 and then perform the Wick rotation ($x_0 \to -ix_4$). Under the Wick rotation, the inner product of four vectors is rewritten as

$$\eta_{\mu\nu}x^\mu x^\nu = -x_0^2 + x_1^2 + x_2^2 + x_3^2 \to \delta_{\mu\nu}x_E^\mu x_E^\nu = x_1^2 + x_2^2 + x_3^3 + x_4^2, \tag{2.15}$$

where $\eta_{\mu\nu} = \mathrm{diag}(-1, 1, 1, 1)$ is the metric tensor in Minkowski space and $\delta_{\mu\nu} = \mathrm{diag}(1, 1, 1, 1)$ denotes Kronecker delta. The action in Minkowski space is replaced by the Euclidean action with the pure imaginary prefactor

$$S_{\mathrm{QCD}} = \int \mathcal{L}_{\mathrm{QCD}} d^4x \to -iS_{\mathrm{QCD}}^E = \int -i\mathcal{L}_{\mathrm{QCD}} d^4x_E, \tag{2.16}$$

while the lagrangian density remains unchanged. Then, S_{QCD}^E becomes positive definite. As a result, the expectation value can be evaluated in the probabilistic way

$$\langle \mathcal{O} \rangle = \int [\mathcal{D}\overline{q}\mathcal{D}q\mathcal{D}A_\mu]\mathcal{O}[\overline{q}, q, A_\mu]P\left[\overline{q}, q, A\right] \tag{2.17}$$

with

$$P\left[\overline{q},q,A\right]=\frac{\exp\left(-S^E_{QCD}\left[\overline{q},q,A\right]\right)}{\int\left[\mathcal{D}\overline{q}\mathcal{D}q\mathcal{D}A_\mu\right]\exp\left(-S^E_{QCD}\left[\overline{q},q,A\right]\right)}, \tag{2.18}$$

which obeys $0\leq P[\overline{q},q,A]\leq 1$.

2.2.2 Action in the discretized space-time

Let us consider the discretized 4 dimensional isotropic box with a lattice spacing a. The lattice spacing a has the inverse mass-dimension, is the primal parameter that determines the scale of this dynamical system. All quantities measured in numerical simulations are dimensionless, therefore the physical quantities are supposed to satisfy the scaling relation $a^d\mathcal{O}_{\mathrm{phys}}=\mathcal{O}_{\mathrm{lat}}$ with d being the mass dimension of $\mathcal{O}$.

The four vector $n=(n_1,n_2,n_3,n_4)$ whose components are given by an integer represents the physical site on the lattice as $x=an=(n_1a,n_2a,n_3a,n_4a)$. First of all, let us define the link variable

$$U(x,x+\hat{\mu}a)=e^{iagA_\mu(x)}, \tag{2.19}$$

where $\hat{\mu}$ denotes an unit four vector in the direction of μ. Here we rewrite $U(x,x+\hat{\mu}a)=U(n,n+\hat{\mu})$ for notational simplicity. Next, we consider the gauge transformation. Under this transformation, the link variable transforms in the adjoint representation as below

$$\begin{aligned}U(n,n+\hat{\mu})\rightarrow U'(n,n+\hat{\mu})&=e^{iagA'_\mu(n)}\\&=\exp\left(-iag\theta^a(n)T^a\right)U(n,n+\hat{\mu})\exp\left(-iag\theta^a(n+\hat{\mu})T^a\right)^\dagger,\end{aligned} \tag{2.20}$$

which indicates that the link variable was defined as the gauge-covariant variable that connects the nearest neighbor sites on the lattice. We can also define the link variable between the remote sites. The product of the two link variables is also gauge-covariant as

$$\begin{aligned}&U(n,n+\hat{\mu})U(n+\hat{\mu},n+\hat{\mu}+\hat{\nu})\rightarrow\left(U(n,n+\hat{\mu})U(n+\hat{\mu},n+\hat{\mu}+\hat{\nu})\right)'\\&=\exp\left(-iga\theta^a(n)T^a\right)U(n,n+\hat{\mu})U(n+\hat{\mu},n+\hat{\mu}+\hat{\nu})\exp\left(-iga\theta^a(n+\hat{\mu})T^a\right)^\dagger.\end{aligned} \tag{2.21}$$

Therefore we can easily construct the gauge invariant quantity by a closed loop of link variables with a trace operation (See also Fig. 2.1) as

$$G=\mathrm{Tr}\prod_{i,\mathrm{closed}}U(n,n_i)=\mathrm{Tr}U(n,n_i)U(n_i,n_{i+1})\cdots U(n_N,n). \tag{2.22}$$

The smallest closed loop forms a "plaquette"[*1] as

$$\begin{aligned}\mathrm{Tr}U_{\mu\nu}(n)&=\mathrm{Tr}\left[U(n,n+\hat{\mu})U(n+\hat{\mu},n+\hat{\mu}+\hat{\nu})U(n+\hat{\mu}+\hat{\nu},n+\hat{\nu})U(n+\hat{\nu},n)\right] &(2.23)\\&=\mathrm{Tr}\left[U(n,n+\hat{\mu})U(n+\hat{\mu},n+\hat{\mu}+\hat{\nu})U^\dagger(n+\hat{\nu},n+\hat{\nu}+\hat{\mu})U^\dagger(n,n+\hat{\nu})\right]. &(2.24)\end{aligned}$$

[*1] A square in French

We then call this closed loop plaquette value. In the naive continuum limit ($a \to 0$), the plaquette values are expressed in terms of the field strength $F_{\mu\nu}$ as

$$\begin{aligned}
&\mathrm{Tr}\left[U(n, n+\hat{\mu})U(n+\hat{\mu}, n+\hat{\mu}+\hat{\nu})U(n+\hat{\mu}+\hat{\nu}, n+\hat{\nu})U(n+\hat{\nu}, n)\right] && (2.25)\\
&= \mathrm{Tr}\left\{\exp\left[iag\left(A_\mu\left(n+\frac{\hat{\mu}}{2}\right) + A_\nu\left(n+\hat{\mu}+\frac{\hat{\nu}}{2}\right) + \frac{iag}{2}\left[A_\mu, A_\nu\right]\right) + \mathcal{O}(a^3)\right]\right. && (2.26)\\
&\left.\times \exp\left[-iag\left(A_\mu\left(n+\hat{\mu}+\frac{\hat{\mu}}{2}\right) + A_\nu\left(n+\frac{\hat{\nu}}{2}\right) + \frac{iag}{2}\left[A_\mu, A_\nu\right]\right) + \mathcal{O}(a^3)\right]\right\} && (2.27)\\
&= \mathrm{Tr}\left\{\exp\left[ia^2 gF_{\mu\nu} + \mathcal{O}(a^3)\right]\right\} = \mathrm{Tr}\left(1 + ia^2 gF_{\mu\nu} + \frac{1}{2}\left(ia^2 gF_{\mu\nu}\right)^2 + \mathcal{O}(a^6)\right). && (2.28)
\end{aligned}$$

Here we used the Baker-Campbell-Hausdorff formula

$$\exp A \exp B = \exp\left(A + B + \frac{1}{2}\left[A, B\right] + \cdots\right), \tag{2.29}$$

and $A_\mu(x + a\hat{\nu}) = A_\mu(x) + a\partial_\nu A_\mu(x) + \mathcal{O}(a^2) = A_\mu(x) + \mathcal{O}(a)$. Using this closed loop, we define the plaquette gauge action S_{plaq}

$$S_{\mathrm{plaq}} = \beta \sum_{n,\mu<\nu}\left[1 - \frac{1}{2N_c}\mathrm{Tr}\left(U_{\mu\nu}(n) + U^\dagger_{\mu\nu}(n)\right)\right] \tag{2.30}$$

where β is defined by $\beta = \frac{2N_c}{g_0^2}$ with the bare coupling g_0 and N_c is defined as $N_c = \mathrm{Tr}1$ and corresponding to 3 in the case of the SU(3) gauge theory. The plaquette gauge action reproduces the gauge action in the continuum in the limit of $a \to 0$ as

$$\begin{aligned}
S_{\mathrm{plaq}} &= a^4 \sum_{n,\mu<\nu}\left(\mathrm{Tr}F_{\mu\nu}F_{\mu\nu}(n) + \mathcal{O}(a^2)\right)\\
&= a^4 \frac{1}{2}\mathrm{Tr}\sum_{n,\mu,\nu} F_{\mu\nu}F_{\mu\nu}(n) + \mathcal{O}(a^6). \qquad (2.31)
\end{aligned}$$

Recall that the lattice spacing a is the primal parameter to determine the scale of the system. Although a has not explicitly appeared in the above formula (Eq. 2.30), the overall factor $\beta = \frac{6}{g_0^2}$ can specify the scale of the system. In the continuum perturbation theory, the coupling constant g and the renormalization scale μ should obey the renormalization group equation

$$\mu\frac{\partial g}{\partial \mu} = -g^3 + \mathcal{O}(g^4). \tag{2.32}$$

Although this equation is derived in the continuum theory, the bare coupling constant g_0 should be determined as the solution of the renormalization group equation in the boundary $\mu = a^{-1}$ for the small a. Therefore, the lattice spacing a also can be obtained as the function of g_0 and then we write the physical quantities measured in lattice QCD as functions of a.

Now we can evaluate the expectation value by the simple multiple integral without violating the gauge symmetry on the lattice. The $\mathcal{O}(a^6)$-terms in Eq. 2.31 are called “lattice artifact” which indicates the difference between the action in the continuum theory and the one defined on the lattice.

2.2.3 Lattice spacing and the continuum limit

As we stressed that the lattice spacing a is the primal parameter in lattice QCD simulations, the measured value in lattice QCD should obey the scaling behavior $\mathcal{O}_{\rm lat}(a) = a^d \mathcal{O}_{\rm phys}$ where d denotes the mass dimension of $\mathcal{O}_{\rm phys}$. Therefore the continuum (physical) value can be obtained from $\frac{\mathcal{O}_{\rm lat}(a)}{a^d} \to \mathcal{O}_{\rm phys}$ in the limit of $a \to 0$, keeping the physical lattice volume $(aL)^3 \times (aT)$ fixed.

In the continuum limit, the bare coupling constant g_0 vanishes and β diverges because a^{-1} is corresponding to the scale of the bare coupling. The scale dependence of g_0 is determined using the perturbation theory and the asymptotic freedom behavior, one of the key features of QCD indicates that g_0 is dramatically changing in the low energy region. So the lattice spacing can be easily read matching $\beta = \frac{6}{g_0^2}$ and $g_0(a)$.

2.2.4 Improvement of the discretized action

The improvement of the lattice action can be achieved by eliminating the lattice artifact. For example, "$\mathcal{O}(a^2)$ improvement" indicates that the $\mathcal{O}(a^6)$ lattice artifacts in the lattice QCD action is eliminated. In order to improve the lattice action, let us add the higher dimensional terms that vanish in the continuum limit into the plaquette action

$$S = c_0 S_{\rm plaq} + a^{4+k} \int dx^4 \sum_{k\geq 1, i} \sum_n c_{4+k,i}(g) \mathcal{O}_{4+k,i}(n), \tag{2.33}$$

where $\mathcal{O}_{4+k,i}(n)$ is the $4+k$ dimensional operator corresponding to the closed line composed with $4+k$ link variable. Note that odd power vanishes due to non-gauge-invariance. In the continuum limit, $\mathcal{O}(a^4)$-term becomes the continuum action. Therefore we call the $\mathcal{O}(a^k)$-level artifacts. In the case of $k=2$, the possible forms are classified into three types [26]. We show these closed loop in Fig. 2.1. The operators $\mathcal{O}_{6,1}(n)$, $\mathcal{O}_{6,2}(n)$ and $\mathcal{O}_{6,3}(n)$ correspond to the rectangular (Fig. 2.1(b)), L-shape (Fig. 2.1(c)), and twister (Fig. 2.1(d)) respectively.

In the continuum, the dimension 6 operators are also given as the combination of the covariant derivative and the field strength [27],

$$\mathcal{O}_1(n) = \sum_{\mu,\nu} {\rm tr}\left(D_\mu F_{\mu\nu} D_\mu F_{\mu\nu}\right)(n) \quad \mathcal{O}_2(n) = \sum_{\mu,\nu,\rho} {\rm tr}\left(D_\mu F_{\nu\rho} D_\mu F_{\nu\rho}\right)(n) \quad \mathcal{O}_3(n) = \sum_{\mu,\nu,\rho} {\rm tr}\left(D_\mu F_{\mu\rho} D_\nu F_{\nu\rho}\right)(n). \tag{2.34}$$

Therefore, up to $\mathcal{O}(a^4)$-level, the lattice action can be represented with additional three operators with parameters c_0, c_1, c_2, c_3

$$S = c_0 S_{\rm plaq} + a^6 \sum_n \left\{ -\frac{2}{3} c_2 \mathcal{O}_1 - \left(2c_1 - 2c_3 + \frac{1}{6}\right) \mathcal{O}_2 - \left(\frac{2}{3} c_2 + 2c_3\right) \mathcal{O}_3 + \mathcal{O}(a^4) \right\}. \tag{2.35}$$

Although choice of c_i is not uniquely determined, they should satisfy the following relation

$$c_0 + 8c_1 + 8c_2 + 16c_3 = 1 \tag{2.36}$$

so that S can reproduce the continuum action in the limit of $a \to 0$. The coefficients $c_{2,3}$ are known to be small

(a) plaquette (b) rectangular

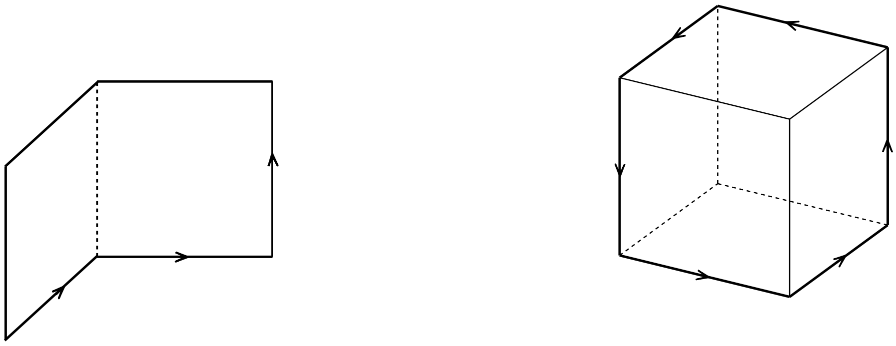

(c) L-shape (d) twister

Fig. 2.1: Illustrated the closed loop from Ref. [28] : Fig. (a) shows the plaquette shape while other figures (b), (c) and (d) show what are composed of six link variables.

and then $\mathcal{O}_{6,2}$ and $\mathcal{O}_{6,3}$ are usually omited in Eq. (2.33). In $\mathcal{O}(a^2)$-level, the major variants of the improved action are two-fold.

- The Symanzik action [29] is one of the variants of the $\mathcal{O}(a^2)$-improved gauge action based on the Callan-Symanzik equation.
- The Iwasaki action [28] is another variant of the $\mathcal{O}(a^2)$-improved gauge action based on the block spin transformation. The block spin transformation is defined as a sort of the renormalization group relation

$$A^{(1)}_{\mu}(n) = \frac{1}{8}\left[A_{\mu}(2n) + \sum_{\nu=1}^{4} A_{\mu}(2n+\tilde{\nu}) + \sum_{\nu\neq\rho} A_{\mu}(2n+\tilde{\nu}+\tilde{\rho}) + \sum_{\nu\neq\rho\neq\lambda\neq\nu} A_{\mu}(2n+\tilde{\nu}+\tilde{\rho}+\tilde{\lambda})\right]$$

  on the lattce. Under the this transformation, one can obtain the $\mathcal{O}(a^2)$-improved action whose parameters are given as $c_1 = -0.331$, $c_0 = 1 - 8c_1$ when the coefficients $c_{2,3}$ are fixed to be zero.

2.3 Fermion action

2.3.1 Wilson Fermion and fermion doubling

Next we introduce the lattice formulation of the fermion action. The fermion propagator defined on the lattice inevitably receives the additional unphysical poles. This is so-called the "doubling" problem. The fermions on the lattice are supposed to be defined so as to avoid this problem. The definition of the lattice action is arbitrary if and only if the continuum limit of the action can reproduce the continuum QCD action. Then we can add the dimension 5 or higher dimension operators to the lattice action so that unwanted doublers are decoupled.

The Wilson fermion is one of the fermion definitions avoiding the doubling problem but the chiral symmetry in the action is explicitly broken down at $\mathcal{O}(a)$-level. Thus the $\mathcal{O}(a)$ improvement is required to restore the chiral symmetry up to $\mathcal{O}(a^2)$-level. Nowadays, the $\mathcal{O}(a)$-improved Wilson fermions (also known as the Wilson-clover fermions) are often used in practice as the fermion with no doubler, mild explicit breaking of chiral symmetry up to $\mathcal{O}(a^2)$.

On the other hand, a large effort had been devoted to find the definition of the exact chiral fermion with no doubler and no explicit breaking of chiral symmetry in the lattice community. We will later introduce the chiral fermion on the lattice.

Fermion doubling

For convenience, we omit the link variable in the fermion action. The fermionic action S_F on the lattice is derived by replacing the derivatives with the finite-differences.

$$S_F = \sum_{n,m} \overline{\psi}(n) D_{nm} \psi(m), \tag{2.37}$$

where the Dirac operator can be represented by

$$D_{nm} = M\delta_{nm} + \frac{1}{2}\sum_{\mu} \left(\gamma_\mu \delta_{n+\hat{\mu},m} - \gamma_\mu \delta_{n-\hat{\mu},m}\right). \tag{2.38}$$

Here we recall that the propagator is determined by the inversion of D_{nm}. We then can easily derive the free fermion propagator $D^{-1}(p)$ in the momentum space [30]. We first get the Fourier transform of D_{mn} as

$$\tilde{D}_{nm} = \int_{-\pi/a}^{\pi/a} \frac{d^4p}{(2\pi)^4} e^{ip(n-m)a} \left[ma + \gamma_\mu \sin p_\mu a\right] \tag{2.39}$$

Therefore we get

$$D^{-1}(p) = \frac{1}{ma + \gamma_\mu \sin p_\mu a} = \frac{ma - \gamma_\mu \sin p_\mu a}{(ma)^2 - \sin^2(p_\mu a)}, \tag{2.40}$$

We can read off the lattice dispersion relation in Minkowski space from the zero of denominator of Eq. 2.40.

$$\sinh^2\left(E(\mathbf{p})a\right) = \sum_{i=1,2,3} \sin^2\left(p_i a\right) + (ma)^2. \tag{2.41}$$

We consider the limit of $a \to 0$, then we get the dispersion relation in the continuum form around $a\mathbf{p} = \mathbf{0}$ as

$$E^2(\mathbf{p}) = \mathbf{p}^2 + m^2. \tag{2.42}$$

However the lattice momentum p_μ typically takes the value from $p_\mu = -\pi/a$ to $p_\mu = \pi/a$ and $E(\mathbf{p})$ becomes the multi-valued function of $\mathbf{p}$. The lattice dispersion relation shows that the additional states propagate in the lattice fermion propagator at low energies. This problem is called "doubling problem".

Wilson fermions

In order to overcome the doubling problem, we add the higher dimensional operator (Wilson-term) into the action,

$$S_W = -ar \int d^4x \overline{\psi}(x) \mathcal{D}^2 \psi(x) \tag{2.43}$$

which vanishes in the limit of $a \to 0$ and is not harmful to get the continuum theory. Then the quark propagator is modified by the presence of the Wilson term,

$$\begin{aligned} D_W(p) &= \frac{1}{ma + r\sum_\mu (1 - \cos p_\mu a) + \gamma_\mu \sin p_\mu a} && (2.44) \\ &= \frac{\Big(ma + r\sum_\mu (1 - \cos p_\mu a)\Big) - \gamma_\mu \sin p_\mu a}{\Big(ma + r\sum_\mu (1 - \cos p_\mu a)\Big)^2 - \sin^2 p_\mu a}. && (2.45) \end{aligned}$$

where the term $r\sum_\mu (1 - \cos p_\mu a)$ that appears in the denominators of Eq. (2.45) comes from the higher dimension term in the action.

The lattice dispersion relation of the Wilson fermions becomes a bit complicated

$$\sinh^2 (E(\mathbf{p}a)) = \sum_i \sin^2 (p_i a) + M^2(\mathbf{p}) a^2 \tag{2.46}$$

where $M(\mathbf{p}) = (ma + r\sum_i (1 - \cos (p_i a)) + r (1 - \cosh (E(\mathbf{p})\, a))$ is the momentum-dependent mass that approaches ma in the limit of $\mathbf{p} \to \mathbf{0}$ and $a \to 0$, it again reproduces the dispersion relation in the continuum theory and the unphysical state propagation is suppressed by the $\cos(\mathbf{p}a)$-terms. We compared the dispersion relation in Fig. 2.2.

The Wilson fermion action $S_F^W = S_F + S_W$ is summarized as below

$$\begin{aligned} S_F^W &= (ma + 4r) \sum_n \overline{\psi}(n)\psi(n) \\ &- \frac{1}{2} \sum_{n,\hat{\mu}} \left[\overline{\psi}(n) (r - \gamma_\mu) U(n, n+\hat{\mu}) \psi(n+\hat{\mu}) \overline{\psi}(n+\hat{\mu}) (r + \gamma_\mu) U^\dagger(n, n+\hat{\mu}) \psi(n) \right]. \end{aligned} \tag{2.47}$$

For further convenience, we introduce the parameter $\kappa = \frac{1}{8r+4ma}$ so that S_F^W is rewritten with κ rather than m

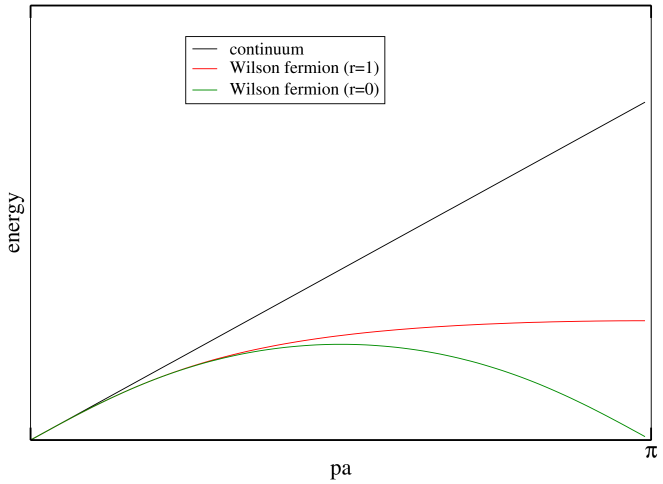

Fig. 2.2: The difference between the continuum and lattice (Wilson) dispersion relation for the massless case ($m = 0$).

and r

$$\begin{aligned} S_F^W = 2\kappa \Bigg\{ & \sum_n \overline{\psi}(n)\psi(n) \\ & - \frac{1}{4\kappa} \sum_{n,\hat{\mu}} \left[\overline{\psi}(n) \left(r - \gamma_\mu\right) U(n, n+\hat{\mu})\psi(n+\hat{\mu}) + \overline{\psi}(n+\hat{\mu}) \left(r + \gamma_\mu\right) U^\dagger(n, n+\hat{\mu})\psi(n) \right] \Bigg\}. \end{aligned} \tag{2.48}$$

The hopping parameter κ is often used as the parameter corresponding to the mass of the fermion instead of m. In the conventional notation, the overall factor 2κ can be eliminated by rescaling the quark field:

$$\psi(n) \to \sqrt{2\kappa}\psi(n) \qquad \overline{\psi}(n) \to \sqrt{2\kappa}\overline{\psi}(n). \tag{2.49}$$

2.3.2 Improved Wilson fermions (also known as Wilson-clover fermions)

In the previous section, the $\mathcal{O}(a)$-improvement was not achieved, rather the doublers are decoupled from the action.

Improvement in the action

The chiral symmetry in the Wilson fermion action is explicitly broken down due to the presence of the $\mathcal{O}(a)$ Wilson term. To eliminate this $\mathcal{O}(a)$ artifact, we consider the dimension 5 clover term (also known as Sheikholeslami-Wohlert term [31])

$$S_{SW} = S_F + S_W - \frac{iac_{SW}\kappa r}{4} \int d^4x \overline{\psi}(x)\sigma_{\mu\nu}F_{\mu\nu}\psi(x), \tag{2.50}$$

where $F_{\mu\nu}$ is defined by the sum of four plaquettes as depicted in Fig. 2.3 and its hermitian conjugate (and that is reason why this term is called by “clover term”). Considering the quark-gluon vertex function at the

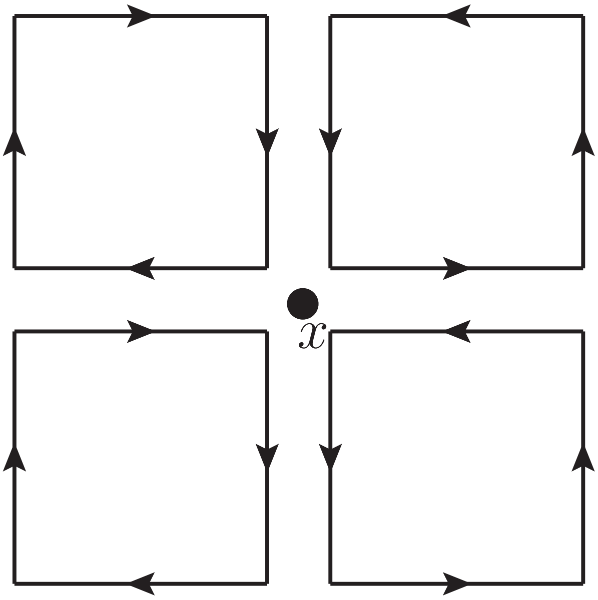

Fig. 2.3: The clover term composed of four link variables.

tree-level [32], c_{SW} can be determined at the tree-level.

$$\Lambda_\mu(p,q) = -gT^a \left\{ i\gamma_\mu + \frac{r}{2}\left(p_\mu a + q_\mu a\right) \right\} - g\frac{rc_{SW}^{(0)}}{2} T^a \sigma_{\mu\nu}\left(p_\nu - q_\nu\right) a + \mathcal{O}(a^2). \tag{2.51}$$

Sandwitching the vertex function by the Dirac spinors and using the Gordon identity, we obtain

$$\overline{u}(p)\Lambda_\mu(p,q)u(p) = -gT^a \overline{u}(p) \left\{ i\gamma_\mu + \left(1 - c_{SW}^{(0)}\right) \frac{ar}{2}\left(p_\mu + q_\mu\right) \right\} u(p) + \mathcal{O}(a^2). \tag{2.52}$$

By taking $c_{SW}^{(0)} = 1$, the $\mathcal{O}(a)$ lattice artifact is canceled at the tree-level. This is called by the "tree-level" $\mathcal{O}(a)$ improvement. In the higher loop calculation, c_{SW} should be expanded in terms of g_0

$$c_{SW} = c_{SW}^{(0)} + c_{SW}^{(1)} \frac{g_0^2}{4\pi} + \cdots \tag{2.53}$$

so that the higher loop correction in the vertex could be eliminated.

Improvement in the current

In the case of the improvement of the fermion action, the current operators are supposed to be improved at the same order. The lattice artifacts appear in the current operator mainly through quantum corrections. So the coefficients of the improvement terms should be evaluated in the perturbation theory or some techniques in lattice QCD such as the Schrödinger functional method. For the $\mathcal{O}(a)$-improved Wilson actions, we consider $\mathcal{O}(a)$ improvement of the bilinear current for the axial channel [33, 34]

$$A_\mu^{\mathrm{imp}}(x) = A_\mu(x) + c_A \partial_\mu P(x), \tag{2.54}$$

and for the tensor channel [33, 34]

$$T_{\mu\nu}^{\mathrm{imp}}(x) = T_{\mu\nu}(x) + c_T\left(\partial_\mu V_\nu(x) + \partial_\nu V_\mu(x)\right), \tag{2.55}$$

where A_μ, P, S, $T_{\mu\nu}$ are usual quark bilinear currents. The coefficients $c_{A,T}$ can be expressed in terms of g_0 similar to c_{SW}

$$c_{A,T} = c_{A,T}^{(0)} + c_{A,T}^{(1)}\frac{g_0^2}{4\pi} + \cdots, \tag{2.56}$$

where $c_{A,T}^{(0)}$ is known to be close to zero from the perturbation theory [35, 34, 36]. The non-perturbative determination can be performed using the Schrödinger functional method introduced later.

Smeared Wilson-clover fermions

In practice, the higher g_0^2 contributions in c_{SW} and $c_{A,T}$ are known to be suppressed by using the smeared link variable technique [37], which makes the link variables thick. The Wilson-clover fermion action with the thickened link variables is often called the smeared Wilson-clover fermions. In fact, the value of c_{SW} measured with the smeared Wilson-clover fermion action is close to unity as expected in the tree-level calculation.

2.3.3 Chiral fermions

A large effort was devoted to formulate the exact chiral fermion or the chiral gauge theory on the lattice. However, the no-go theorem has been proved by Nielsen and Ninomiya [38]. This theorem states that we cannot define the exact chiral fermion with no doubler on the lattice. The history of the lattice formulation of the chiral gauge theory is summarized in Ref. [39]. Recently, it is found that there is a way to evade the no-go theorem through the modification of the chiral symmetry on the lattice.

Domain-wall fermions

Kaplan suggested a novel method [40] for simulating chiral fermions on the lattice without violating the no-go theorem. Kaplan's idea is following. Introducing the extra fifth dimension, we can define the modified chiral symmetry defined by the five dimensional lattice and then the chiral fermions with no doublers can be constructed on the four dimensional boundary in the five dimension while the doubler modes are still alive in the extra dimension. This is a formulation of so-called "Domain-wall" fermions (DWFs). In the definition in Ref. [41], the Dirac operator of the domain-wall fermion is given by the five dimensional Wilson-like action

$$\begin{aligned}
D_{n,s;n',s'} &= \delta_{s,s'}D^{\parallel}_{n,n'} + \delta_{n,n'}D^{\perp}_{s,s'} && (2.57)\\
D^{\perp}_{s,s'} &= \frac{1}{2}\sum_{\mu=1}^{4}\left[(1-\gamma_\mu)U(n,n+\hat{\mu})\delta_{n+\hat{\mu},n'} + (1+\gamma_\mu)U^\dagger(n',n'+\hat{\mu})\delta_{n-\hat{\mu},n'}\right]\\
&\quad + (M_5-4)\delta_{n,n'} && (2.58)\\
D^{\parallel}_{n,n'} &= \frac{1}{2}\left[(1-\gamma_5)\delta_{s+1,s'} + (1+\gamma_5)\delta_{s-1,s'} - 2\delta_{s,s'}\right]\\
&\quad - \frac{m_f}{2}\left[(1-\gamma_5)\delta_{s,L_s-1}\delta_{0,s'} + (1+\gamma_5)\delta_{s,0}\delta_{L_s-1,s'}\right] && (2.59)
\end{aligned}$$

with the fifth direction s, s' ($0 \leq s, s' \leq L_s - 1$ with L_s assumed to be even). M_5 is the mass in the fifth dimensional direction and also corresponding to the height of the domain-wall, while m_f is the ordinary fermion mass in the four dimension and is given as the coupling between two domain-walls with different chiralities. The chiral fermion is almost located in the four dimensional boundary at $s = 0, L_s - 1$ as a soliton (domain-wall) solution of the domain-wall Dirac operator. As result, the Dirac fermions $\psi(n), \overline{\psi}(n)$ on the four dimensional lattice are given by the five-dimensional fermions $\Psi(n, s)$ at the boundaries ($s = 0, L_s - 1$)

$$\psi(n) = P_L \Psi(n, 0) + P_R \Psi(n, L_s - 1) \tag{2.60}$$

$$\overline{\psi}(n) = \overline{\Psi}(n, L_s - 1) P_L + \overline{\Psi}(n, 0) P_R. \tag{2.61}$$

That is why this method is called the “Domain-wall” fermion method. Since the fifth dimensional length L_s is finite, the fermion dynamically couples to the fermion with the opposite chirality without the presence of m_f. Therefore, the fermion mass may receive the finite L_s correction. We will revisit this issue in Chap. 3.

Although QCD is not a chiral gauge theory but a vector gauge theory, the chiral symmetry is the basic feature of QCD and plays the important role in the hadron physics. Although the DWFs has its complex definition that requires more expensive computational cost as typically L_s times larger than the Wilson fermions.

There are some remarkable benefits using DWFs in practice:

- The conserved axial current can be defined in DWFs. Then the renormalization constant Z_A for the local axial current can be determined.
- The renormalization constants for the local vector and axial currents satisfy $Z_V = Z_A$ in the limit of the vanishing fermion mass.

2.4 Observable

We introduced the lattice formulation of QCD in the previous section. In this section, we will discuss the general measurement in lattice QCD. We also give a brief review of analysis on the measured values.

The expectation value of an “observable” $\mathcal{O}$ which should be the gauge invariant operator is denoted by $\langle \mathcal{O} \rangle$. We focus on the correlation functions of hadron operators as the colorless, gauge invariant operators. As discussed earlier, we should integrate out the fermionic variables before evaluating the expectation value. As a result of the functional integration over the fermionic variables, we obtain the hadron correlation functions that are expressed in terms of the quark two-point correlation function.

2.4.1 Configuration and measurement

Before moving on the details of the measurement in the next section, we briefly review how to measure the expectation value of $\mathcal{O}$ in the background of the gauge configurations $\{U_i\}$. In lattice QCD simulations, we evaluate the observable $\mathcal{O}$ using the path integral method

$$\langle \mathcal{O} \rangle = \int [DU] \mathcal{O}[U] P[U] \tag{2.62}$$

with

$$P\left[U\right]=\frac{\exp\left(-S_{QCD}^{E}\left[U\right]\right)}{\int[DU]\exp\left(-S_{QCD}^{E}\left[U\right]\right)}. \tag{2.63}$$

Similar to the case of the statistical problem, we can evaluate the expectation value of the observable, using the Monte-Carlo integration approach [42]

$$\langle\mathcal{O}\rangle=\frac{1}{N}\sum_{i}^{N}\mathcal{O}[U_i], \tag{2.64}$$

where U_i is a configuration of the link variables which is generated with the probability $P\left[U\right]$. Once a sequence of the configuration $\{U_i\}$ is given, any observable depending on U_i is computable.

2.4.2 Hadron correlation function

Mesonic operator and two-point function

The hadron operator can be constructed with its specific quantum numbers such as the number of valence quark. total-spin and flavor (iso-spin). The meson and baryon operators are given by the bilinear and trilinear quark interpolating operators:

$$\mathcal{O}_M=q\Gamma\overline{q} \qquad\qquad \mathcal{O}_B=\epsilon_{abc}(q_a^TC\Gamma_1\gamma_5q_b)\Gamma_2q_c. \tag{2.65}$$

The twp-point function of hadrons is one of the simplest observables in lattice QCD. In general, the hadron operator can be overlaped with a towers of all states with the same quantum numbers.

$$\langle\mathcal{O}_M(t')\mathcal{O}_M^\dagger(t)\rangle=\sum_i\langle\mathcal{O}_M(t')|i\rangle\langle i|\mathcal{O}_M(t)\rangle \tag{2.66}$$

$$=\sum_i\left|\langle\mathcal{O}_M(0)|i\rangle\right|^2e^{-M_i(t'-t)} \tag{2.67}$$

$$\to\left|\langle\mathcal{O}_M(0)|0\rangle\right|^2e^{-M_0(t'-t)} \tag{2.68}$$

where M_i denotes the mass of the i-th excited state.

Although all states propagate in the hadron two-point function, the contributions from the excited state exponentially decrease in large time separation. The ground state contribution dominates the hadron two-point function in the region where $(t'-t)/a\gg1$ We can define the "effective" mass of the ground state which shows the mass of the ground state M_0 after the ground state saturation $(t'-t)/a\gg1$.

$$E_{\text{eff}}(t',t)=\ln\frac{\langle\mathcal{O}_M(t')\mathcal{O}_M^\dagger(t)\rangle}{\langle\mathcal{O}_M(t'+1)\mathcal{O}_M^\dagger(t)\rangle}\to M_0 \tag{2.69}$$

We show the two-point function and the effective mass of the pion measured using DWFs as typical examples in Fig. 2.4. Because of the periodic boundary condition on the lattice $A(t+L)=A(t)$, the contribution from the state propagating backward in time such as $e^{-M_i(T-t)}$ is also present as shown in the left panel of Fig. 2.4.

Three-point function

The three-point function can be computed by inserting the operator $\mathcal{O}$ between the source and sink hadron operators.

$$\begin{aligned}
\langle \mathcal{O}_M(t_{\text{sink}}) O(t) \mathcal{O}_M^\dagger(t_{\text{src}}) \rangle &= \sum_{i,j} \langle \mathcal{O}_M(t_{\text{sink}}) | j \rangle \langle j | O(t) | i \rangle \langle j | \mathcal{O}_M(t_{\text{src}}) \rangle && (2.70) \\
&= \sum_{i,j} \langle \mathcal{O}_M | j \rangle \langle j | O | i \rangle \langle i | \mathcal{O}_M \rangle \exp\left[-M_i(t_{\text{sink}} - t) - M_j(t - t_{\text{src}})\right] && (2.71) \\
&\to \sum_i \left| \langle \mathcal{O}_M | i \rangle \right|^2 \langle i | O | i \rangle \exp\left[-M_i t_{\text{sep}}\right] && (2.72) \\
&\to \left| \langle \mathcal{O}_M | 0 \rangle \right|^2 \langle 0 | O | 0 \rangle \exp\left[-M_0 t_{\text{sep}}\right] && (2.73)
\end{aligned}$$

where $t_{\text{sep}} = t_{\text{sink}} - t_{\text{src}}$. The hadron matrix element $\langle 0|O|0\rangle$ is determined by

$$\frac{\langle \mathcal{O}_M(t_{\text{sink}}) O(t) \mathcal{O}_M^\dagger(t_{\text{src}}) \rangle}{\langle \mathcal{O}_M(t_{\text{sink}}) \mathcal{O}_M^\dagger(t_{\text{src}}) \rangle} \to \langle 0|O|0\rangle \qquad \text{for } t_{\text{sink}} \gg t \gg t_{\text{src}}. \tag{2.74}$$

Baryon correlation function

The two-point function of the baryon is described by the 4×4 matrix in terms of the spinor space. Although the baryon operator is specified by its parity, the propagator which is constructed of the local baryon propagator also receives the contribution from the opposite parity state. Here $\mathcal{O}_B^\eta(\mathbf{x}, t)$ is the baryon operator which has the intrinsic parity $\eta(=\pm)$ and transforms as following

$$\mathcal{P} \mathcal{O}_B^\eta(\mathbf{x}, t) \mathcal{P}^\dagger = \eta \gamma_4 \mathcal{O}_B^\eta(-\mathbf{x}, t) \tag{2.75}$$

where we use the parity transformation of quark field $\mathcal{P} q(\mathbf{x}, t) \mathcal{P}^\dagger = +\gamma_4 q(-\mathbf{x}, t)$. Considering the relation between the negative and positive parity operator $\mathcal{O}_B^+(x) = \gamma_5 \mathcal{O}_B^-(x)$, we derive the relation between the two-point functions

$$\langle \mathcal{O}_B^+(x) \overline{\mathcal{O}}_B^+(y) \rangle = -\gamma_5 \langle \mathcal{O}_B^-(x) \overline{\mathcal{O}}_B^-(y) \rangle \gamma_5 \tag{2.76}$$

which indicates that the two-point function has overlap with both parity states. Then the two-point function can be decomposed by both of the positive and negative parity state contributions [43] as

$$\langle \mathcal{T} \mathcal{O}_B^+(t_{\text{sink}}) \overline{\mathcal{O}}_B^+(t_{\text{src}}) \rangle = \frac{1 + \text{sign}(t_{\text{sep}})\gamma_4}{2} \sum_i C_i^+ e^{-M_i^+ |t_{\text{sep}}|} - \frac{1 - \text{sign}(t_{\text{sep}})\gamma_4}{2} \sum_i C_i^- e^{M_i^- |t_{\text{sep}}|} \tag{2.77}$$

where $t_{\text{sep}} = t_{\text{sink}} - t_{\text{src}}$ and $\frac{1+\text{sign}(t_{\text{sep}})\gamma_4}{2}$ is a projector which appears in the asymptotic form of the two-point function [44]. Here $C_i^{+(-)}$ denotes the amplitude of the baryon operator and the i-th excited positive (negative) parity state while $M_i^{+(-)}$ denotes the mass of the i-th excited positive (negative) parity state. In the case of the proton operator, M_0^+ corresponds the mass of the ground state of the proton. Note that the opposite parity

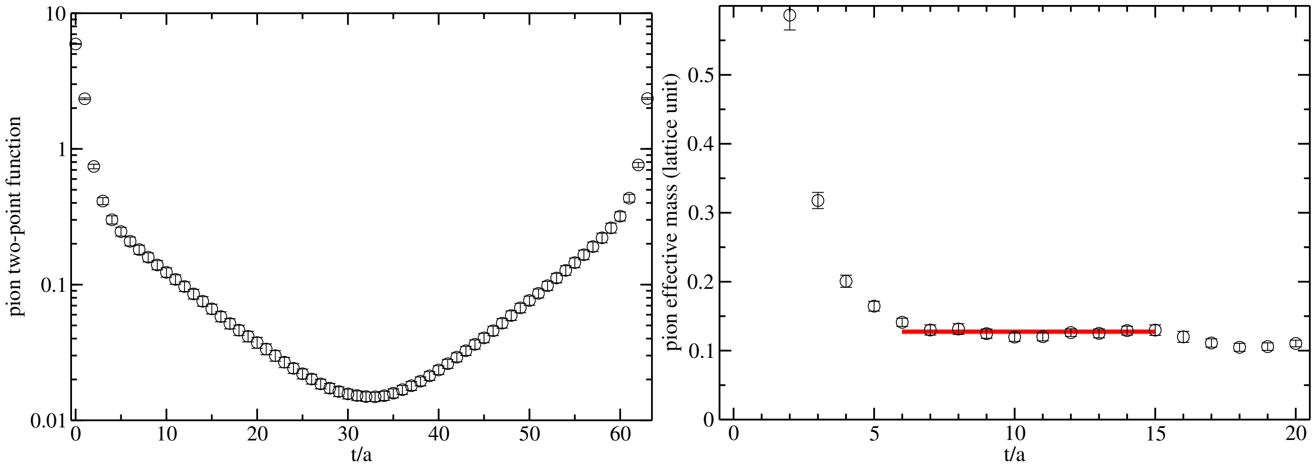

Fig. 2.4: The two-point function and the effective mass measured in lattice QCD. The left figure shows the pion two-point function measured in DWFs while the right figure shows the effective mass obtained from the pion two-point function.

states are also propagating forward in time [43]. Using the parity projection operator $\mathcal{P}_\pm = \frac{1\pm\gamma_4}{2}$, we obtain

$$\frac{1}{4}\mathrm{tr}\left\{\mathcal{P}_\pm \langle \mathcal{O}_B(t_{\mathrm{sink}})\overline{\mathcal{O}}_B(t_{\mathrm{src}})\rangle\right\} = \theta(t_{\mathrm{sep}})\sum_i C_i^+ e^{-M_i^+ t_{\mathrm{sep}}} - \theta(-t_{\mathrm{sep}})\sum_i C_i^- e^{M_i^- t_{\mathrm{sep}}}. \tag{2.78}$$

Even after the parity projection, contributions of the opposite parity state propagating backward in time are not eliminated.

Chapter 3

Renormalization in lattice QCD

In continuum, the vector and axial local currents in the chiral limit are not renormalized such that $Z_V = Z_A = 1$ because of the chiral symmetry. However, the renormalization constants Z_V and Z_A must be evaluated on the lattice, where the local currents are not conserved and $Z_V \neq Z_A$ in general. The renormalized vector charge g_V^{ren}, whose value is scheme independent, must be unity. Therefore, we can easily estimate Z_V as an inverse of the bare value of the vector charge g_V^{bare} calculated on the lattice. On the other hand the renormalized axial charge g_A^{ren} is not unity even in the chiral limit due to the spontaneous chiral symmetry breaking. However the relation of $Z_V = Z_A$ can be satisfied for the chiral fermion on the lattice such as domain-wall-fermions

For other currents such as the scalar and tensor currents, we have to compute the renormalization constants, Z_S and Z_T in a certain scheme. We adopt the Regularization Independent (RI) scheme to determine the normalization constant of the local current non-perturbatively.

3.1 Regularization Independent (RI) scheme in lattice QCD

The general idea for the renormalization of the quark operator is discussed in Ref. [45]. In this thesis, we concentrate on the renormalization for the quark bilinear operator. We first define the renormalized bilinear operator with the Dirac gamma matrix Γ_O with the current renormalization constant Z_O

$$\left(\overline{q}\Gamma_O q\right)_R = Z_O \left(\overline{q}\Gamma_O q\right)_B \tag{3.1}$$

where the subscripts R and B represent "renormalized" and "bare" operators respectively. The most simple observable involving the bilinear current is the quark three-point correlation which is given by the bilinear current operator computed between two external quark line, carrying momentum p_1 and p_2. Its Feynman diagram up to one-loop order in the perturbation theory is given by

$\langle p_1|\,(\overline{q}\Gamma_O q)\,(x)|p_2\rangle =$

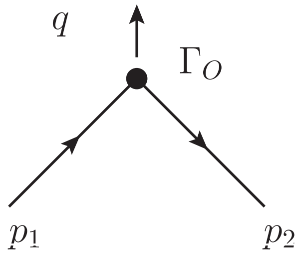

$+$

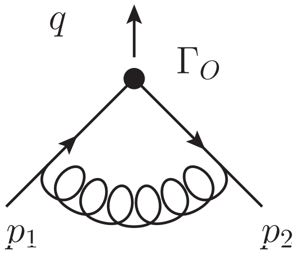

(3.2)

$+$

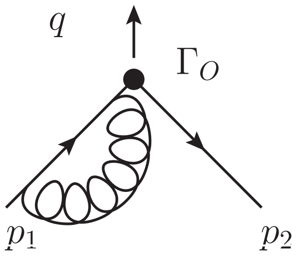

$+$

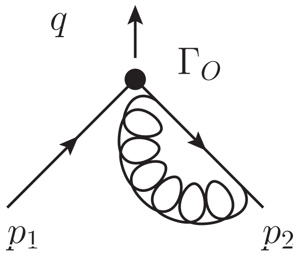

$+\cdots,$ (3.3)

where the solid straight line represents the quark propagator while the curly lines denote gluons. Its amputated correlation function called as the vertex function is defined by

$$\begin{aligned}\Lambda_O(p_1,p_2) &= \langle G(p_1;x)\rangle^{-1}\langle p_1|\overline{q}\Gamma_O q(x)|p_2\rangle\langle G(p_2;x)\rangle^{-1}\\ &= \langle G(p_1;x)\rangle^{-1}\langle G(p_1;x)\Gamma_O G^{\dagger}(p_2;x)\rangle\langle G(p_2;x)\rangle^{-1}\end{aligned} \tag{3.4}$$

where $G(p;x)$ is the one-side Fourier-transformed quark propagator

$$G(p;x) = \int dy\,\exp(-ip\cdot y)\langle q(y)\overline{q}(x)\rangle. \tag{3.5}$$

Note that the renormalized vertex function is given by

$$(\Lambda_O)_R = \frac{Z_O}{Z_q}\,(\Lambda_O)_B\,, \tag{3.6}$$

where Z_q is the field renormalization constant. In the Regularization Independent (RI) scheme, we impose the following formula as the renormalization condition

$$(\Lambda_O)_R = (\Lambda_O)_{\text{tree}} = \Gamma_O \tag{3.7}$$

with $p_1^2 = p_2^2 = \mu_0^2$ being the scale of the renormalization. The renormalization constants Z_O and Z_q calculated from

$$\mathrm{Tr}\frac{Z_O}{Z_q}\,(\Lambda_O)_B\,\mathcal{P}_O = \mathrm{tr}\Gamma_O\mathcal{P}_O, \tag{3.8}$$

where the symbol “Tr” denote the trace over color and spinor with the appropriate projection operator $\mathcal{P}_O$. The choice of the projection operators and momenta p_1 and p_2 is not unique. There are some variants of the RI

type	kinematics	projection operator
RI/MOM	$p_1 = p_2, q = 0$	equal to Γ_O
RI/SMOM	$p_1^2 = p_2^2 = q^2$	Eq. 3.9
RI/SMOM$_\gamma$	$p_1^2 = p_2^2 = q^2$	equal to Γ_O

Table 3.1: Summary of types of the RI schemes.

scheme as followings.

3.1.1 Momentum subtraction (MOM) scheme

The RI/MOM (MOM stands for momentum) scheme is the most intuitive and conventional approach with $p_1 = p_2$ momentum configuration. In this scheme, we choose the the projection operator $\mathcal{P}_O$ equal to Γ_O as the projector. As discussed in Ref. [46], this scheme behave worse in the infrared region because of the vanishing momentum for the external field such as $q = p_1 - p_2 = 0$.

3.1.2 Symmetric momentum (SMOM) scheme

In the RI/SMOM scheme, we impose the symmetric momentum configuration $p_1^2 = p_2^2 = q^2 \neq 0$. Therefore we expect the better infrared behavior than the conventional RI/MOM scheme.

The projection operators are chosen as below [47].

$$\mathcal{P}_O = \begin{cases} \frac{q^\nu \gamma_\nu q_\mu}{q^2} & \text{for } \Gamma^O = \gamma_\mu \\ \frac{q^\nu \gamma_\nu q_\mu \gamma_5}{q^2} & \text{for } \Gamma^O = \gamma_\mu \gamma_5 \\ \gamma_\mu \gamma_\nu & \text{for } \Gamma^O = \gamma_\mu \gamma_\nu \\ (\gamma_5) & \text{for } \Gamma^O = (\gamma_5) \end{cases} \tag{3.9}$$

There is another variant of the RI/SMOM scheme, namely RI/SMOM$_\gamma$. In the RI/SMOM$_\gamma$ scheme, we also impose the symmetric momentum configuration while the projection operators are chosen as the same as the RI/MOM scheme.

The RI/SMOM$_\gamma$ scheme was introduced [46] to overcome the infrared behavior in the RI/MOM scheme whose the momentum transfer q vanishes. The RI/SMOM scheme is the more theoretically improved scheme where the renormalization conditions satisfy Ward-Takahashi identities for the vector and axial channel up to $\mathcal{O}(\alpha_s)$.

The kinematics and the choice of the projection operators are summarized in the Tab. 3.1.

3.1.3 Conversion and evolving

In order to convert Z_O ($O = S$ and T) from the RI scheme to the $\overline{\text{MS}}$ scheme, we use the conversion factor computed in the perturbation theory with help of the renormalization group. Two-loop conversion factor C_Γ^{SMOM} which can convert an operator from the RI scheme to the $\overline{\text{MS}}$ scheme in the Landau gauge has been already given in Ref. [48]. The evolution factor in the $\overline{\text{MS}}$ scheme for $Z_\Gamma^{\overline{\text{MS}}}(2\text{GeV})/Z_\Gamma^{\overline{\text{MS}}}(\mu_0)$ is evaluated with the three-loop beta function and the three-loop anomalous dimension. Combining the conversion factor and the evolution factor, we get the conversion factor at two-loop level.

Finally, the total matching factor is given by

$$Z_O^{\overline{\mathrm{MS}}}(\mu) = \frac{Z_O^{\overline{\mathrm{MS}}}(\mu)}{Z_O^{\overline{\mathrm{MS}}}(\mu_0)} \frac{Z_O^{\overline{\mathrm{MS}}}(\mu_0)}{Z_O^{\mathrm{MOM}}(\mu_0)} Z_O^{\mathrm{MOM}}(\mu_0). \tag{3.10}$$

3.2 Residual scale dependence

The scale of the renormalization should be kinematically determined. For example, in both of cases of the RI/MOM and RI/SMOM schemes, the scale is only given by the external momenta $\mu_0^2 = p_1^2 = p_2^2$. Moreover, the renormalization constant should obey the scaling behavior as expected in the perturbation theory. Therefore the renormalization constant in the appropriate scale (typically 2 GeV) should be uniquely determined, not depending on the matching scale μ_0.

In practice, the renormalization constant still depends on the matching scale μ_0 even after the conversion and evolution due to three reasons :

1. the presence of lattice artifacts at higher μ_0 like $(a\mu_0)^i$.
2. non-perturbative artifact at lower μ_0 like $(a\mu_0)^{-i}$.
3. the truncation of the perturbative series at lower μ_0.

The first point is purely originated from the lattice discretization effects. Our aim in this section is to extract the relevant μ_0-independent value c_0 for the continuum perturbation theory. In order to eliminate the residual μ_0 dependence, we first focus on the lattice discretization artifacts.

The problem indicated in the second and third points can be avoided if we choose the appropriate scale μ_0. Thus we will discuss the second and third points later.

3.2.1 Lattice artifacts

There are two types of the lattice artifacts. One is stemming from the difference between the lattice dispersion relation and the continuum one (denoted as ordinary lattice artifact). Another is associated with the SO(4) breaking effect on the lattice (denoted as hypercubic artifact).

Ordinary lattice artifact

As describe earlier, the size of momentum is only a choice of typical kinematical scale μ_0 in determination of the renormalization constant from the vertex function. The ordinary lattice artifacts can be described by the polynomial of the dimensionless variable $(a\mu_0)$ as the discretization effects

$$Z_O(\mu_0) = c_0 + \sum_{i>0} c_i (a\mu_0)^i \tag{3.11}$$

where the odd power terms do not present under the symmetry $p \to -p$ for the external momentum. We will adopt the above functional form to extract the relevant μ_0-independent value c_0.

Hypercubic artifact

In this section, we introduced the scale $\mu_0^2 = p_1^2 = p_2^2$ as the Lorentz scalar in this kinematics. Actually the physical quantity on the lattice depends on not only the Lorentz scalar under the SO(4) symmetry such as the inner product of four vectors $p_\mu p^\mu$ but also the invariant value under the H(4) symmetry in general. In the case of the quark vertex function, H(4) invariant values are given by the composition of two external momenta p_1 and p_2. Then the values can be classified by the configuration of p_1 and p_2. We call this class a "orbit" [50]. The orbit contains all combinations of p_1 and p_2 which have the same hypercubic parameters $C^S_{4,i}, C^A_{4,i} \cdots$ as will be introduced later. Let us start with the simplified kinematics $p = p_1 = p_2$ in the RI/MOM scheme. Since the rotational symmetry is partly broken on the lattice, the renormalization constant may depend not only on the Euclidean norm but also on the $2n$-norm [50, 49, 51] that is defined as

$$p^{[2n]} = \sum_\mu p_\mu^{2n}. \tag{3.12}$$

Note that in the case of $n = 1$, $p^{[2]} = p^2$. The orbit can be defined as a set of the momentum configurations

$$\{p = (p_1, p_2, p_3, p_4) | p^{[4]} = c_4 (p^2)^2, p^{[6]} = c_6 (p^2)^3, \cdots\} \tag{3.13}$$

which is specified by the parameters c_i. In general, the renormalization constant depends c_i as well as p^2. Once parameters c_i are chosen, $p^{[2n]}$ terms are automatically absorbed into the ordinary lattice artifact that is proportional to $(ap)^{2n}$. The explicit expansion in terms of $p^{[2n]}$ is given as following

$$c_4 a^4 p^{[4]} + c_6 a^6 p^{[6]} + \left(c_8 a^8 p^{[8]} + c_{44} a^8 p^{[4]} p^{[4]}\right) + \mathcal{O}(a^{10}). \tag{3.14}$$

Averaging over the momentum configurations that provide the same value of p^2 is often adopted conventionally. As a result, the observed quantity is expected to behave a function of p^2, however the result given by this method is known to be a non-smooth function of p^2 but rather a function suffered from the "fishbone" structure described in Ref. [51]. This particular behavior as the non-smooth p^2 dependence is critical for precise determination of the renormalization constant.

In the case of the non-exceptional kinematics, such as $p_1^2 = p_2^2 = q^2$ with $p_1 \neq p_2$, the renormalization factor seems to be much suffered from more complicated terms that contain both of two momenta p_1 and p_2 [6]. $q^{[2n]}$ can be expanded in terms of $P^{[2n,k]}$

$$q^{[2n]} = \sum_\mu \left({p_1}_\mu - {p_2}_\mu\right)^{2n} = \sum_{k=0}^{2n} {}_{2n}C_k P^{[2n,k]} \tag{3.15}$$

where $P^{[2n,k]}$ can be defined as

$$P^{[2n,k]} = \sum_\mu \left({p_1}_\mu^{2n-k} {p_2}_\mu^{k}\right). \tag{3.16}$$

Note that $q^{[2]} = q^2$, and q^2 can be expand in terms of $P^{[2n,k]}$ as

$$q^2 = \sum_{\mu} \left(p_{1\mu} - p_{2\mu}\right)^2 \tag{3.17}$$

which is rewritten by

$$\mu_0^2 = \mu_0^2 - 2P^{[2,1]} + \mu_0^2 \tag{3.18}$$

when the scale μ_0 is chosen as $q^2 = \mu_0^2$. Therefore $P^{[2,1]}$ is proportional to the Euclid norm with the non-exceptional momentum configuration $p_1^2 = p_2^2 = q^2 = \mu_0^2$

$$P^{[2,1]} = \frac{\mu_0^2}{2}. \tag{3.19}$$

Then the contribution from $P^{[2,1]}$ is absorbed into the ordinary lattice artifacts as $(a\mu_0)^2$.

We define the symmetric and anti-symmetric hypercubic parameters with referring to Ref. [6],

$$S_{2n,k} = \frac{1}{2}\left(\frac{P^{[2n,k]}}{p^{2n}} + \frac{P^{[2n,2n-k]}}{p^{2n}}\right) \qquad k = 0, \cdots, n \tag{3.20}$$

$$A_{2n,k} = \frac{1}{2}\left(\frac{P^{[2n,k]}}{p^{2n}} - \frac{P^{[2n,2n-k]}}{p^{2n}}\right) \qquad k = 0, \cdots, n-1 \tag{3.21}$$

so that $S(A)$ is (anti)symmetric under the exchange $p_1 \to p_2$.

$$S_{2n,k} \to +S_{2n,k} \tag{3.22}$$

$$A_{2n,k} \to -A_{2n,k} \tag{3.23}$$

$$S_{2n,k}S_{2n',j} \to +S_{2n,k}S_{2n',j} \tag{3.24}$$

$$S_{2n,k}A_{2n',j} \to -S_{2n,k}A_{2n',j} \tag{3.25}$$

$$A_{2n,k}A_{2n',j} \to +A_{2n,k}A_{2n',j} \tag{3.26}$$

Then we can expand the lattice artifacts in terms of $(a\mu_0)^{2n}$ with above defined S and A. Up to $\mathcal{O}((a\mu_0)^8)$, we can thus generalize the lattice artifact part of $\sum_{i>0} c_i(a\mu_0)^i$ in Eq. 3.11 by

$$\begin{aligned}
&c_2(a\mu_0)^2\\
&+c_4(a\mu_0)^4 + \sum_{k=0}^{4}(a\mu_0)^4 c_{4,k}^{(S)} S_{4,k}\\
&+c_6(a\mu_0)^6 + \sum_{k=0}^{6}(a\mu_0)^6 c_{6,k}^{(S)} S_{6,k}\\
&+c_8(a\mu_0)^8 + \sum_{k=0}^{8}(a\mu_0)^8 c_{8,k}^{(S)} S_{8,k} + \sum_{k>j\geq 0}^{4} (a\mu_0)^8 c_{8,8,k,j}^{(SS)} S_{4,k}S_{4,j} + \sum_{k>j\geq 0}^{4} (a\mu_0)^8 c_{8,8,kj}^{(AA)} A_{4,k}A_{4,j},
\end{aligned} \tag{3.27}$$

which is taken into account the hypercubic corrections.

3.2.2 Eliminating the hypercubic artifact

Once a orbit is chosen, the hypercubic artifacts are automatically absorbed into the ordinary lattice artifacts $(a\mu_0)^{2n}$ because $S_{2n,i}, A_{2n,i}$ are not variables anymore. Although strictly choosing the orbit is an ideal solution, a orbit contains only few momentum configurations. Therefore we should perform a sort of a fit in order to eliminate the hypercubic artifact.

Averaging method

As introduced earlier, the renormalization constant only depending on μ_0 can be obtained from averaging over the different orbits,

$$Z_O^{\mathrm{ave}}(a\mu_0) = \sum_{p_1,p_2} Z_O(a\mu_0, S_{4,i}, A_{4,i}\cdots). \tag{3.28}$$

The averaging method in general can not eliminate the hypercubic artifact. Therefore the obtained function $Z_O^{\mathrm{ave}}(a\mu_0)$ usually does not behave as the smooth function of μ_0.

Subtracting method

The subtracting method is introduced in the case of the gluon propagator [52, 53], but it is also applicable for the quark vertex [50]. We can expand the renormalization constant with the hypercubic artifact

$$\begin{aligned} Z_O(a\mu_0, S_{4,i}, A_{4,i}\cdots) = &\; Z_O(a\mu_0, S_{4,i}, A_{4,i}\cdots)|_{S_{4,i}=0,\cdots} \\ &+ \sum_{i,n} \frac{\partial}{\partial S_{2n,i}} Z_O(a\mu_0, S_{4,i}, A_{4,i}\cdots)\bigg|_{S_{4,i}=0,\cdots} S_{2n,i} \\ &+ \sum_{i,n} \frac{\partial}{\partial A_{2n,i}} Z_O(a\mu_0, S_{4,i}, A_{4,i}\cdots)\bigg|_{S_{4,i}=0,\cdots} A_{2n,i} \end{aligned} \tag{3.29}$$

where the subtracted value $Z_O(a\mu_0, S_{4,i}, A_{4,i}\cdots)|_{S_{4,i}=0,\cdots}$ is independent on the hypercubic artifacts. After the subtraction, we adopt the functional form Eq. (3.11) only depending on $a\mu_0$. Recall that there is no momentum configuration which satisfies $S_{2n,i} = 0, A_{2n,i} = 0$. Therefore the subtracted value would be often away from the original data.

3.2.3 Non-perturbative effect

There are further corrections from non-perturbative effects associated with the vacuum condensation. In the case of the Landau gauge, $\langle A^2\rangle$ condensate may couple to the quark propagator [49]. Then the renormalization constant also receives from the dimension two condensate contribution $\frac{\langle A^2\rangle}{\mu_0^2}$. However, such power divergence behavior becomes serious only if simulations are performed in the large lattice volume, where the lower momentum can be accessible. Moreover, the perturbation theory does not work in the low μ_0 region, and then the data points affected by non-perturbative effects are often truncated during the conversion from the RI scheme to the $\overline{\mathrm{MS}}$ schemes. Therefore, we will omit this term in the case of the results of DWFs that are not calculated at large enough lattice volume.

3.3 Summary of the RI scheme

In this section, we briefly summarize how to determine the renormalization constant in the RI scheme. At first, we can obtain the renormalization constant in the RI scheme using the following procedure:

- compute bare amputated vertex functions $(\Lambda_O)_B$.
- obtain the projected vertex function $\mathrm{Tr}\mathcal{P}_O\left(\Lambda_O\right)_B$ with the appropriate projection operator and the momentum configuration that specify types of the RI scheme summarized in Tab. 3.1.
- calculate the ratio $\mathrm{Tr}\mathcal{P}_{A,V}\left(\Lambda_{V,A}\right)_B/\mathrm{Tr}\mathcal{P}_O\left(\Lambda_O\right)_B = Z_O/Z_{V,A}$ where the renormalization constants $Z_{V,A}$ can be measured in other schemes and known to be scale and scheme -independent.
- the individual renormalization constant $Z_O^{\mathrm{RI}}(\mu_0)$ can be obtained at the renormalization scale of μ_0 which is kinematically determined.

To be compared with the experimental value, the renormalization constant in $\overline{\mathrm{MS}}$ scheme at an appropriate scale (typically 2 GeV) $Z_O^{\overline{\mathrm{MS}}}(2\text{ GeV})$ should be obtained. With the help of the perturbation theory, we can determine $Z_O^{\overline{\mathrm{MS}}}(2\text{ GeV})$ as followings:

- convert the renormalization constant into $Z_O^{\overline{\mathrm{MS}}}(\mu_0)$ using the matching factor $\frac{Z_O^{\overline{\mathrm{MS}}}(\mu_0)}{Z_O^{\mathrm{RI}}(\mu_0)}$ obtained from the perturbation theory.
- evolve $Z_O^{\overline{\mathrm{MS}}}(\mu_0)$ to $Z_O^{\overline{\mathrm{MS}}}(2\text{ GeV})$ using the β-function and anomalous dimension in the $\overline{\mathrm{MS}}$ scheme.

The evaluated $Z_O^{\overline{\mathrm{MS}}}(2\text{ GeV})$ is still depending on the scale μ_0 in practice due to (1) lattice artifacts (2) non-perturbative effects (3) the truncation of the perturbation theory. The relevant renormalization constant which is independent on the matching scale μ_0 can be obtained using the following methods :

1. eliminate the residual dependence on the choice of the matching scale by the fit ansatz.
2. taking the continuum limit if necessary.

The evaluated $Z_O^{\overline{\mathrm{MS}}}(2\text{ GeV})$ is also depending on the choice of the momentum configuration. This type of the artifact is often called by the “hypercubic” artifact. To eliminate the hypercubic artifact, the several methods can be applicable:

- Averaging method : The single-valued function of μ_0 can be obtained however the result is known to be still highly contaminated from the hypercubic artifacts.
- Subtracting method : In this method, the hypercubic artifact is eliminated by using the ansatz.

3.4 Renormalization in other schemes

3.4.1 Conserved axial-vector current in Domain-wall fermions

In the domain-wall fermion formalism the five-dimensional current $\mathcal{A}_\mu$ is defined by

$$\mathcal{A}_\mu(x) = \sum_{s=0}^{L_s-1} \left(s - \frac{L_s - 1}{2} \right) j^a_\mu(x, s) \tag{3.30}$$

with

$$\begin{aligned} j^a_\mu(n, s) = \frac{1}{2} \big[& \overline{\Psi}(n + \hat{\mu}, s)(1 + \gamma_\mu)U^\dagger(n + \hat{\mu}, n)t^a\Psi(n, s) \\ & -\overline{\Psi}(n, s)(1 - \gamma_\mu)U(n, n + \hat{\mu})t^a\Psi(n + \hat{\mu}, s) \big], \end{aligned} \tag{3.31}$$

which obeys the following divergence condition [41].

$$\Delta_\mu \mathcal{A}^a_\mu(n) = 2m_f J^a_5(n) + 2J^a_{5q}(n) \tag{3.32}$$

Here the derivative Δ_μ is defined by the forward difference as $\Delta_\mu f(n) = f(n) - f(n - \hat{\mu})$. The J^a_5 and J^a_{5q} operators are defined by

$$J^a_5(n) = -\overline{\Psi}(n, L_s - 1)P_L t^a \Psi(n, 0) + \overline{\Psi}(n, 0)P_R t^a \Psi(n, L_s - 1) \tag{3.33}$$

$$= \overline{q}(n)t^a\gamma_5 q(n) \tag{3.34}$$

$$J^a_{5q}(n) = -\overline{\Psi}(n, L_s/2 - 1)P_L t^a \Psi(n, L_s/2) + \overline{\Psi}(n, L_s/2)P_R t^a \Psi(n, L_s/2 - 1) \tag{3.35}$$

where J^a_5 is a pseudoscalar density made up of quark fields on the boundary of the fifth dimension while J^a_{5q} is a pseudoscalar density containing quark fields of the intermediate layers in the fifth dimension. Even in the limit $m_f = 0$, a non-vanishing divergence of the axial current is caused by the presence of J_{5q}, which will vanish as $L_s \to \infty$. However, such an anomalous term, provides the residual chiral symmetry breaking effect, which can be described by an additive quark mass in the four-dimensional low energy action for QCD. The current $\mathcal{A}_\mu$ approximately obeys the continuum type Ward-Takahashi identity as

$$\partial_\mu \mathcal{A}^\mu(x) = 2(m_{\text{res}} + m_f)J^a_5(n). \tag{3.36}$$

The conserved axial current $\mathcal{A}$ should be proportional to the non-conserved local axial current operator A with proportionality constant Z_A which is the renormalization constant for the local axial current as $Z_A A_\mu = \mathcal{A}_\mu$. Using the following correlation functions of $\mathcal{A}$ and A

$$C(t + 1/2) = \sum_n \langle \mathcal{A}^a_0(\vec{n}, t)\pi^a(\vec{0}, 0)\rangle \tag{3.37}$$

$$L(t) = \sum_n \langle A^a_0(\vec{n}, t)\pi^a(\vec{0}, 0)\rangle, \tag{3.38}$$

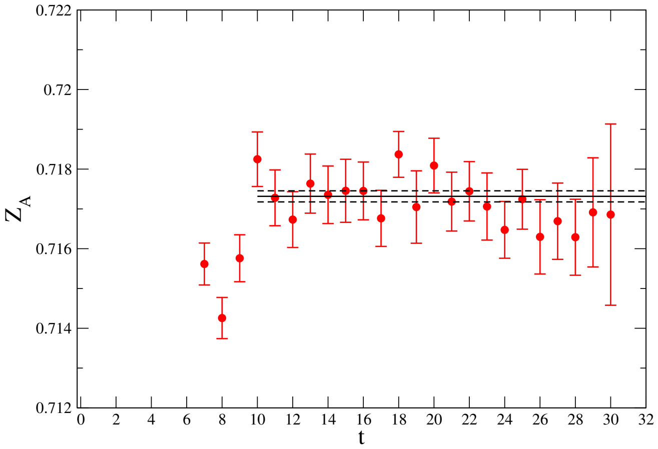

Fig. 3.1: The determination of Z_A using the conversed axial-vector current defined in DWFs. This figure is taken from Ref. [54].

we can evaluate the axial renormalization constant Z_A as the ratio of above two correlators

$$Z_A(t) = \frac{1}{2}\left\{\frac{C(t+1/2)+C(t-1/2)}{2L(t)} + \frac{2C(t+1/2)}{L(t)+L(t+1)}\right\}. \tag{3.39}$$

Chapter 4

Numerical results (Domain-Wall Fermions)

We will report the renormalized nucleon coupling constants from lattice QCD simulations in this and the next chapters. In this chapter, we present some results obtained from 2 + 1 flavor domain-wall fermions ensembles generated by RBC+UKQCD Collaborations. As summarized in Tab. 4.1, Our simulations are performed at two different lattice spacings corresponding to $a \approx 0.114$ fm (coarse) and $a \approx 0.086$ fm (fine). The light quark masses are $am_l = 0.005, 0.010, 0.020$ (0.004, 0.006, 0.008) and the strange quark mass is $am_s = 0.04$ (0.03) on the coarse (fine) lattice. The residual fermion masses are measured to be $am_{\rm res} = 0.003152(43)$ for the coarse lattice and 0.0006664(76) for the fine lattice with fifth dimensional extent $L_s = 16$ and the Domain-wall height of $M_5 = 1.8$.

Although the simulated pion mass is heavier than the physical pion mass, we can perform the chiral and continuum extrapolation to obtain the continuum value at the physical point since the simulations are performed at three different quark masses at two different lattice spacings. It is worth mentioning that DWFs action is one of lattice fermion actions that posses the chiral symmetry. There are good properties of DWFs in practice:

- $\mathcal{O}(a)$-improvement is not needed since the chiral symmetry is not explicitly broken down.
- Z_A can be precisely determined because of the presence of the conserved axial currents.

4.1 Nucleon matrix element

4.1.1 three-point function

In order to calculate the nucleon matrix element in lattice QCD simulations, we compute the three-point correlation functions consisting of the smeared proton source and sink operators (N and $\overline{N}$) with a given bilinear

β	$L^3 \times T$	L_5	aM_5	a^{-1} [GeV]	Z_A	$am_{\rm res}$	am_s	am_l	M_π [GeV]
2.13	$24^3 \times 64$	16	1.8	1.73(3)	0.71651(46) [54]	0.003152(43)	0.04	0.005	0.3294(13)
								0.010	0.4164(12)
								0.020	0.5550(12)
2.25	$32^3 \times 64$	16	1.8	2.28(3)	0.74475(12) [54]	0.0006664(76)	0.03	0.004	0.2902(41)
								0.006	0.3445(47)
								0.008	0.3926(53)

Table 4.1: Simulation parameters of each ensemble used in this thesis. Further information is available in Ref. [55].

operator $O = \overline{u}\Gamma^O u - \overline{d}\Gamma^O d$

$$C_O^{\mathcal{P}}(t) = \frac{1}{4}\mathrm{Tr}\left\{\mathcal{P}_O\langle N(t_{\mathrm{sink}})O(t)\overline{N}(t_{\mathrm{src}})\rangle\right\}, \tag{4.1}$$

where $\mathcal{P}_O$ is an appropriate projection operator defined as

$$\mathcal{P}_O^i = \begin{cases} \mathcal{P}_+\gamma_i\gamma_5 & \text{for the axial and tensor channels} \\ \mathcal{P}_+\gamma_4 & \text{for the vector and scalar channels.} \end{cases} \tag{4.2}$$

Note that γ_i corresponds to the polarized direction of the nucleon that is usually chosen as $i = 3$.

As described in the previous chapter, a well-known procedure for determining the couplings is to calculate the following ratio for the three-point and two-point correlation functions with zero momentum transfer

$$\frac{C_O^{\mathcal{P}}(t)}{C_{\mathrm{2pt}}(t_{\mathrm{sink}} - t_{\mathrm{src}})} \to g_O^{\mathrm{bare}} \qquad \text{for} \qquad t_{\mathrm{sink}} \gg t \gg t_{\mathrm{src}}, \tag{4.3}$$

where $C_{\mathrm{2pt}}(t_{\mathrm{sink}} - t_{\mathrm{src}})$ represents the proton two-point correlation function with the same smeared source and sink at the rest frame. Recall that the ratio vanishes unless $\Gamma^O = 1(S)$, $\gamma_4(V)$, $\gamma_i\gamma_5(A)$, and $\sigma_{ij}(T)$ with $i, j = 1, 2, 3$ [56]. The non-vanishing ratio gives an asymptotic plateau corresponding to the bare value of the coupling g_O relevant for the O channel. In this study we focus on the axial (A), scalar (S) and tensor (T) channels.

4.1.2 Smeared operator

In order to statistically improve the operator, the smearing technique is often adopt. In general, smeared nucleon operator is given by

$$N(x) = \int d\mathbf{y}_1 \int d\mathbf{y}_2 \int d\mathbf{y}_3 \left(q(\mathbf{y}_1, x_4)^T C\gamma_5 q(\mathbf{y}_2, x_4)\right) q(\mathbf{y}_3, x_4) \prod_i \theta(\mathbf{x} - \mathbf{y}_i) \tag{4.4}$$

where the function θ specify the shape of the smeared operator. If $\theta(\mathbf{x} - \mathbf{y}_i) = \delta(\mathbf{x} - \mathbf{y}_i)$, $N(x)$ is nothing but a local source $\left(q(x)^T C\gamma_5 q(x)\right) q(x)$. In this simulation, we use the local source and the Gauss-smeared source at $\mathbf{y}_1 = \mathbf{y}_2 = \mathbf{y}_3$ with the iterative technique [57] which keeps the smeared operator gauge-covariant. Using the smeared and local source, we can calculate three types of correlators by the choice of the source and sink operator. For example,

$$C_{\mathrm{2pt}}^{LL}(t_{\mathrm{sink}} - t_{\mathrm{src}}) = \frac{1}{4}\mathrm{Tr}\left\{\mathcal{P}_+\langle N_L(x_{\mathrm{sink}})\overline{N}_L(x_{\mathrm{src}})\rangle\right\} \tag{4.5}$$

$$C_{\mathrm{2pt}}^{LS}(t_{\mathrm{sink}} - t_{\mathrm{src}}) = \frac{1}{4}\mathrm{Tr}\left\{\mathcal{P}_+\langle N_L(x_{\mathrm{sink}})\overline{N}_S(x_{\mathrm{src}})\rangle\right\} \tag{4.6}$$

$$C_{\mathrm{2pt}}^{SS}(t_{\mathrm{sink}} - t_{\mathrm{src}}) = \frac{1}{4}\mathrm{Tr}\left\{\mathcal{P}_+\langle N_S(x_{\mathrm{sink}})\overline{N}_S(x_{\mathrm{src}})\rangle\right\} \tag{4.7}$$

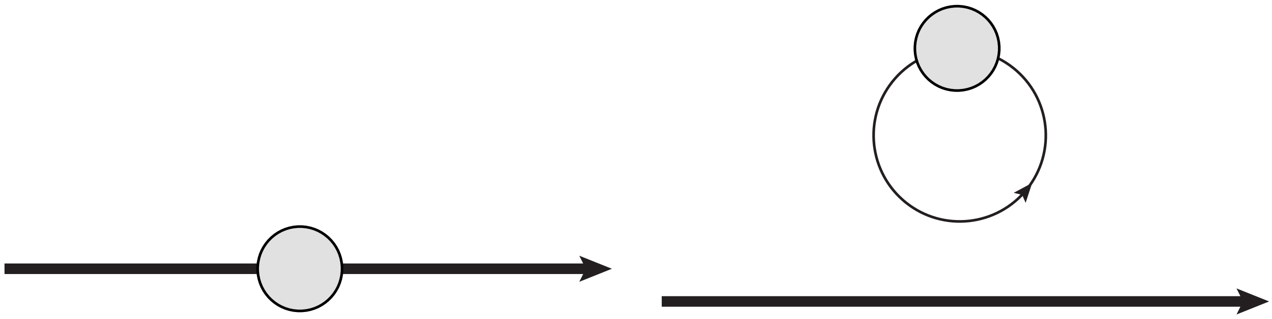

Fig. 4.1: The connected (left) and disconnected (right) diagram contributing the nucleon three-point function. The thick solid line represents the nucleon propagator while the thin solid line represents the quark propagator. The gray shaded circle also represents the bilinear current such as $\overline{\psi}\Gamma_O\psi$. In the case of the connected diagram, we only have to calculate the valence quark diagram while we also have to calculate the quark loop diagram in the case of the disconnected diagram. The computation of operator-inserted quark loop diagram is time consuming because we have to calculate the quark propagator with unfixed source and sink.

where $N_L(S)$ denote the local (smeared) nucleon operator. We also define the smeared-to-smeared three-point function as

$$C^{SS}_{3\text{pt},O}(t_{\text{sink}}, t, t_{\text{src}}) = \frac{1}{4}\text{Tr}\left\{\mathcal{P}_O\langle N_S(t_{\text{sink}})O(t)\overline{N}_S(t_{\text{src}})\rangle\right\}. \tag{4.8}$$

The coupling constant for the O channel is given by

$$\frac{C^{SS}_{3\text{pt},O}(t_{\text{sink}}, t, t_{\text{src}})}{C^{SS}_{2\text{pt}}(t_{\text{sink}} - t_{\text{src}})} \to g_O \qquad \text{for} \qquad t_{\text{sink}} \gg t \gg t_{\text{src}} \tag{4.9}$$

as similar as the case for the local source.

4.1.3 Connected and disconnected diagram

The nucleon three-point functions are given by the two Feynman diagrams in Fig. 4.1. Although the disconnected diagram can contribute flavor diagonal charge g^q_O, $q = u, d, s$ as the sea quark effect, such contributions to the isovector charges $g^u_O - g^d_O$ are canceled out under the exact isospin symmetry. Then we had computed only the connected diagram in calculating the nucleon three-point function to obtain the isovector charges of the nucleon from 2+1 flavor lattice QCD where the up and down quark masses are equal.

4.1.4 Bare coupling

We show the bare couplings in the vector (V), axial (A), scalar (S) and tensor (T) channels with 3 different quark masses $am_l = 0.020, 0.010, 0.005$ $(0.008, 0.006, 0.004)$ on the coarse (fine) lattice $\beta = 2.13, (2.25)$. As shown in Fig. 4.2, 4.3 and Fig. 4.4, 4.5, all of four bare couplings, which are calculated from the relevant three-point correlation functions divided by the nucleon two-point function using the Gauss-smearing method, show asymptotic plateau behaviors in the middle region between the source and sink points. Therefore, we chose the range $4 \leq t/a \leq 8$ $(5 \leq t/a \leq 10)$ for determining the bare coupling in each channel through a constant fit on the coarse (fine) lattice. The obtained values of the bare couplings for the vector, axial, tensor and scalar are summarized in Tab. 4.2.

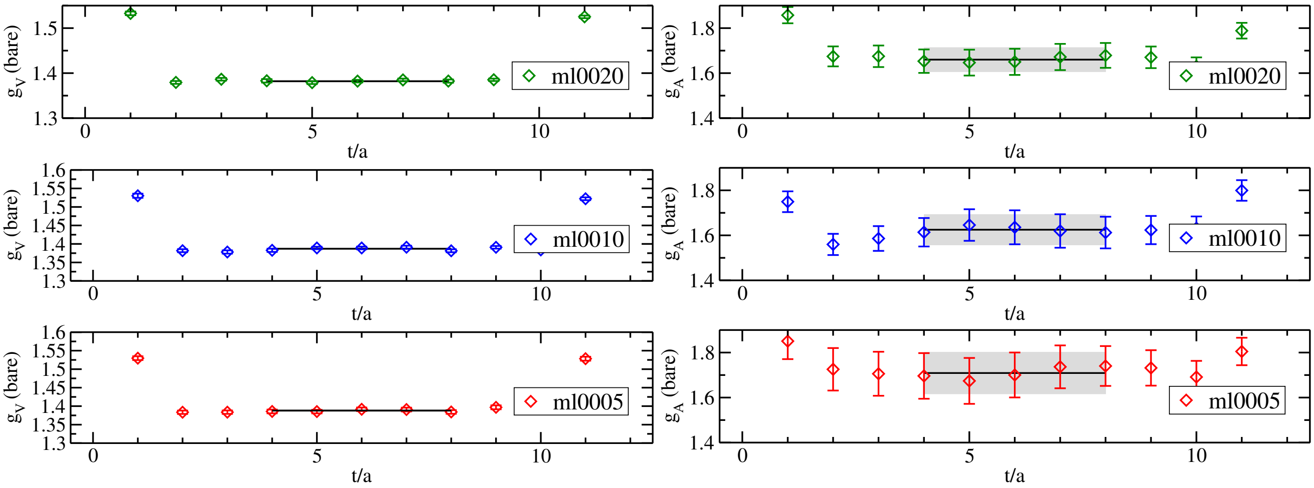

Fig. 4.2: Bare couplings at $\beta = 2.13$ for $\Gamma = V$ (left) and A (right) as a function of the current insertion time slice.

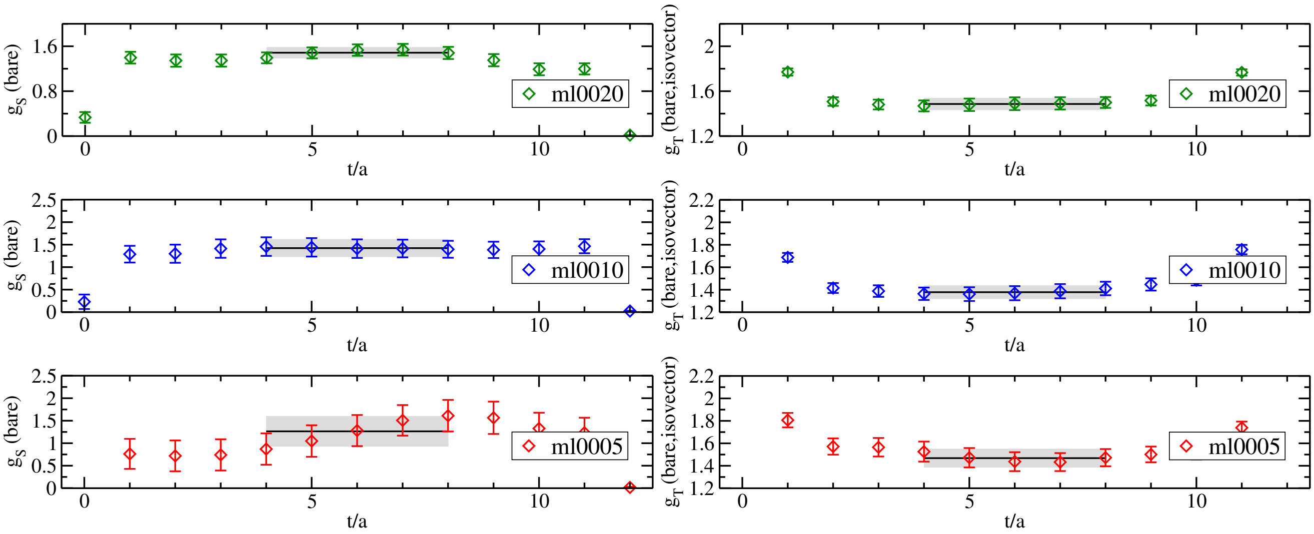

Fig. 4.3: Bare couplings at $\beta = 2.13$ for S (left) and T (right lower) as a function of the current insertion time slice.

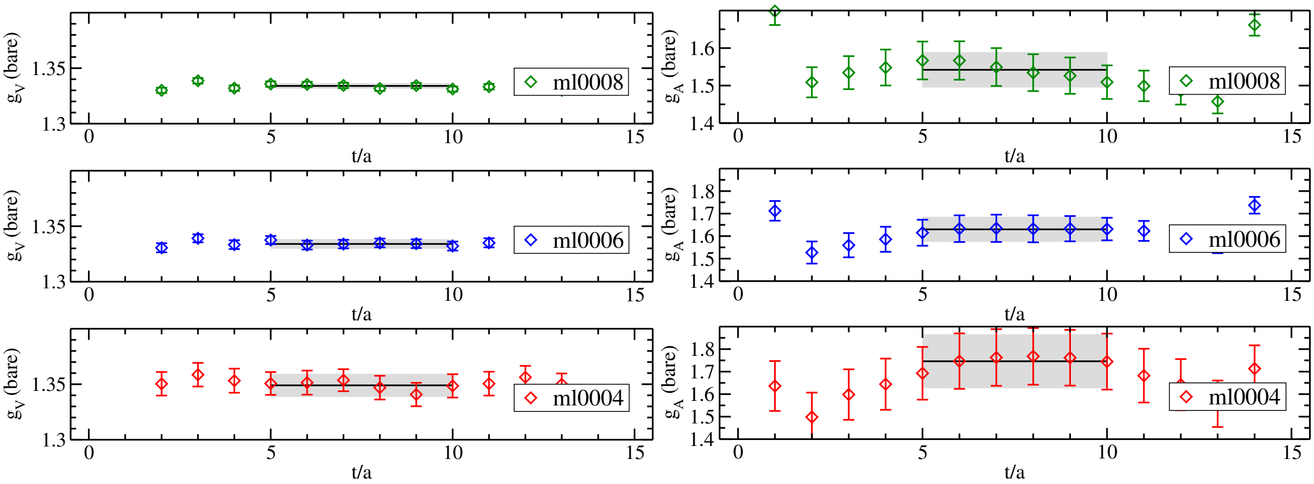

Fig. 4.4: Bare couplings at $\beta = 2.25$ for $\Gamma = V$ (left) and A (right as a function of the current insertion time slice.

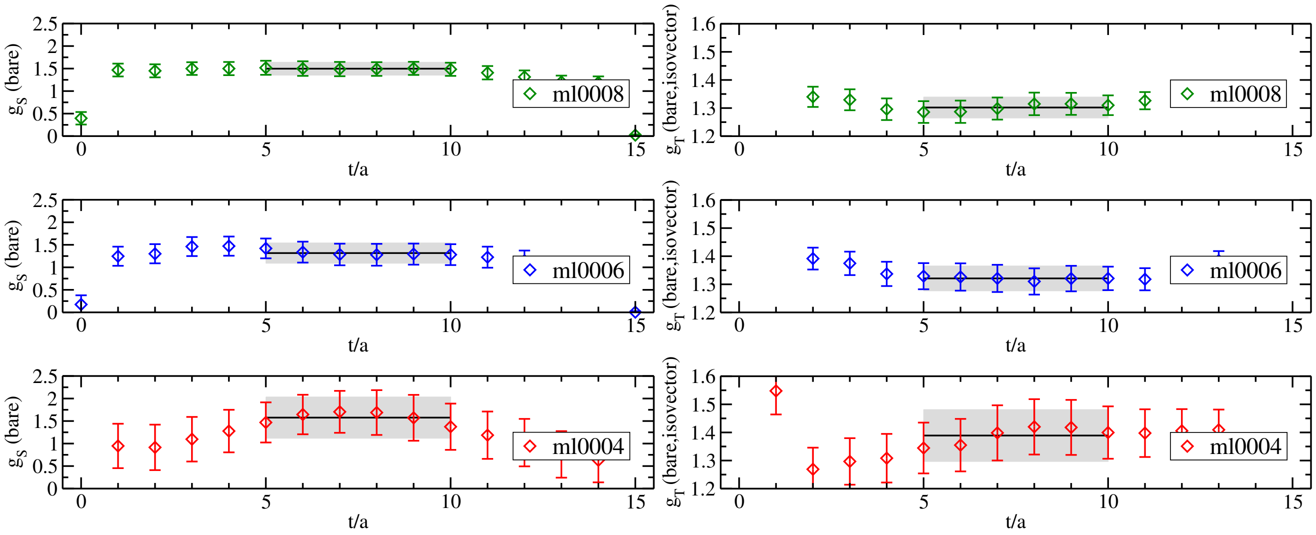

Fig. 4.5: Bare couplings at $\beta = 2.25$ for S (left) and T (right) as a function of the current insertion time slice.

β	m_f	$g_V^{\rm bare}$	$g_A^{\rm bare}$	$g_T^{\rm bare}$	$g_S^{\rm bare}$	Fit range	# of conf.	# of meas.
2.25	0.004	1.349(10)	1.746(118)	1.389(92)	1.576(456)	[5:10]	120	960
	0.006	1.334(4)	1.630(54)	1.321(44)	1.316(224)	[5:10]	120	960
	0.008	1.334(2)	1.542(46)	1.302(37)	1.497(142)	[5:10]	120	960
2.13	0.005	1.388(3)	1.709(92)	1.468(80)	1.264(331)	[4:8]	240	1920
	0.010	1.387(2)	1.625(67)	1.378(57)	1.424(190)	[4:8]	120	960
	0.020	1.382(2)	1.660(53)	1.486(51)	1.485(93)	[4:8]	80	640

Table 4.2: Measured bare couplings with each fermion masses.

4.2 Renormalization constant

As mentioned earlier, Z_A can be precisely measured using the non-local conserved axial current for DWF quarks. We thus use the value of Z_A at each lattice spacing given by this method [58, 54] for the final estimation of the renormalized axial-vector charge. The values of Z_A are tabulated in Tab. 4.1. For the other currents such as the scalar and tensor currents, we have to compute the renormalization constants, Z_S and Z_T in a certain scheme. We adopt the RI/SMOM scheme to non-perturbatively determine the normalization factor of those local currents through the following procedure. Together with the precisely determined Z_A, we can evaluate individual values of $Z_{T,S}$ at the scale of μ

$$Z_{S(T)}^{\rm RI/SMOM}(\mu) = \frac{Z_{S(T)}^{\rm RI/SMOM}(\mu)}{Z_A} Z_A = \frac{\Lambda_A^{\rm Tr,RI/SMOM}(\mu)}{\Lambda_{S(T)}^{\rm Tr,RI/SMOM}(\mu)} Z_A \tag{4.10}$$

where we define $\Lambda_O^{{\rm Tr},i}$ as the traced three-point function

$$\Lambda_O^{\rm Tr,RI/SMOM} = \frac{1}{3\cdot 4} {\rm Tr}\left[\mathcal{P}_O \Lambda_O\right]_{\rm RI/SMOM}. \tag{4.11}$$

Recall that there are three different variants of the RI scheme, namely RI/MOM, RI/SMOM and RI/SMOM$_\gamma$. Except for the RI/MOM scheme which behaves worse in the low energy region, these are good candidates of the intermediate scheme in order to determine the renormalization constant in the $\overline{\mathrm{MS}}$ scheme. The difference between different intermediate schemes should be regarded as lattice discretization uncertainties. In this sense, we may quote the systematic uncertainty stemmed from the lattice artifact through the difference between two schemes. Since we performed simulations at two different lattice spacings, the systematic uncertainties due to the discretization can be eliminated by the continuum extrapolation. Therefore we calculate the renormalization constant only in the RI/SMOM scheme in this chapter.

The previous studies for the renormalization constant are summarized in Tab. 4.3.

	β	Z_V	Z_A	$Z_T^{\overline{\mathrm{MS}}}(2\ \mathrm{GeV})$	$Z_m^{\overline{\mathrm{MS}}}(2\ \mathrm{GeV})$
RBC	2.13	0.7179(9) [59]	0.7161 [58]	0.783(6) [60]	1.578(2)[*3] ,1.534(10)[*4] [54]
+			0.71651(46)[*1],0.71689(51)[*2] [54]		
UKQCD	2.25	-	0.74475(12)[*1],0.74469(13)[*2] [54]	-	1.573(2)[*3] ,1.541(7)[*4] [54]
LHP	2.13	0.7161(1)[*5] [61]	0.7161(1)[*5] [61]	-	-
	2.25	0.7468(39)[*6] [61]	0.74521(2)[*6] [61]	-	-

Table 4.3: Previous studies on the renormalization by RBC+UKQCD Collaboration [54, 59, 60] and LHP Collaboration [61]. Z_m is defined as $Z_m = \frac{2}{Z_P+Z_S}$.

4.2.1 Measurement

Source

We calculated the Fourier-transformed quark propagator on each gauge configuration. Recall that the point-like source can equally overlap with all modes in the momentum space. Thus the Fourier-transformed propagator can be obtained from the single point-to-point correlator. The more statistically improved correlator could be given by the smearing method applying in the momentum space. However such approach requires to calculate the correlators for each fixed momentum, therefore it is practically unrealistic within our limited computational resource. We thus adopt the former approach where single point-to-point correlator is used to be well-balanced between the reasonable statistical uncertainty and the computational costs.

Momentum

The accessible momentum states are of course limited on the lattice with lattice spacing a. The typical maximum value of the momentum is given by $ap_{\max} \sim 2\pi$. We choose the common $p_{\max} \sim 5$ GeV. We also note that the momentum configuration should be carefully chosen for the RI/SMOM scheme where the symmetric momentum configuration $p_1^2 = p_2^2 = (p_1 - p_2)^2$ is required. Especially in the case at $\beta = 2.13$, the discretized momenta are given by

$$ap_i = \begin{cases} \frac{2\pi n_i}{24} & i = 1, 2, 3 \\ \frac{2\pi n_i}{64} & i = 4. \end{cases} \tag{4.12}$$

[*1] chiral limit

[*2] chiral limit and physical sea s quark mass

[*3] via RI/SMOM$_{\gamma_\mu}$ scheme

[*4] via RI/SMOM scheme

[*5] $m_l = 0.005, m_s = 0.004$

[*6] $m_l = 0.004, m_s = 0.003$

ID	β	$L^3 \times T$	a^{-1} [GeV]	am_l	N_{conf}	(ap_{max})
ml0005	2.13	$24^3 \times 64$	1.73(3)	0.005	59	8
ml0010				0.010	60	8
ml0020				0.020	27	8
ml0004	2.25	$32^3 \times 64$	2.28(3)	0.004	59	6
ml0006				0.006	60	6
ml0008				0.008	60	6

Table 4.4: We summarized the parameters for the computation on the renormalization constant.

Since ap_1 is not proportional to ap_4 with any combination of n_i if $n_i < 8$, the symmetric momentum configuration cannot be easily chosen. Then we have chosen $ap_{\text{max}} = 8$ for $\beta = 2.13$, $ap_{\text{max}} = 6$ for $\beta = 2.25$ (Tab. 4.4). As a result, we obtain the renormalization constant in the range of $0.64 < \sqrt{p^2} < 5.5$ [GeV] for $\beta = 2.13$ and $0.63 < \sqrt{p^2} < 4.2$ [GeV] for $\beta = 2.25$. From a viewpoint of the perturbation theory, the data point below $\sqrt{p^2} \sim 0.8$ [GeV] should be removed. On the other hand $\sqrt{p^2} \sim 5.5$ seems to be too large compared with the lattice cutoff corresponding to $a^{-1} \sim 1.73$ [GeV] for the coarse lattice. In this sense, we have no concrete criterion on determining the fit window. We directly examine the fit-range dependence later.

We show measured values of the ratio of the renormalization constants Z_T/Z_A in Fig. 4.6.

4.2.2 Test for the chiral symmetry

In the case of DWFs, the relation $Z_V = Z_A$ may be satisfied because of the chiral symmetry in the chiral limit. In fact, the previous research summarized in Tab. 4.3 indicates that the relation $Z_V = Z_A$ is satisfied within the statistical uncertainty. To examine the relation in the RI scheme, we define the parameter c_{A-V}

$$c_{A-V} \equiv 2 \times \frac{1/\Lambda_A^{\text{Tr},i} - 1/\Lambda_V^{\text{Tr},i}}{1/\Lambda_A^{\text{Tr},i} + 1/\Lambda_V^{\text{Tr},i}} = \frac{Z_A - Z_V}{\frac{1}{2}(Z_V + Z_A)} \tag{4.13}$$

that should vanish in the chiral limit. We show c_{A-V} in Fig. 4.7 and we observed that c_{A-V} is consistent with zero with the statistical uncertainties except a few lowest momentum points.

4.2.3 Dependency on the scale

The residual scale dependence should be taken into account as one of the lattice artifacts. Our simulations are performed with two difference lattice spacings. We thus can take the continuum limit of the results obtained from the coarse and fine lattice. After taking the continuum limit, all lattice artifacts are supposed to vanish automatically. Then it is not necessary to examine the residual scale dependence of the renormalization constant given at each lattice spacing carefully. Nevertheless, we evaluate the μ_0-independent value of individual renormalization constants at given lattice spacing for following reasons:

1. It is worth measuring the possible systematic uncertainties due to the different ansatz for μ_0-dependence.
2. The individual renormalization constant at each lattice spacings can be used for other purposes.

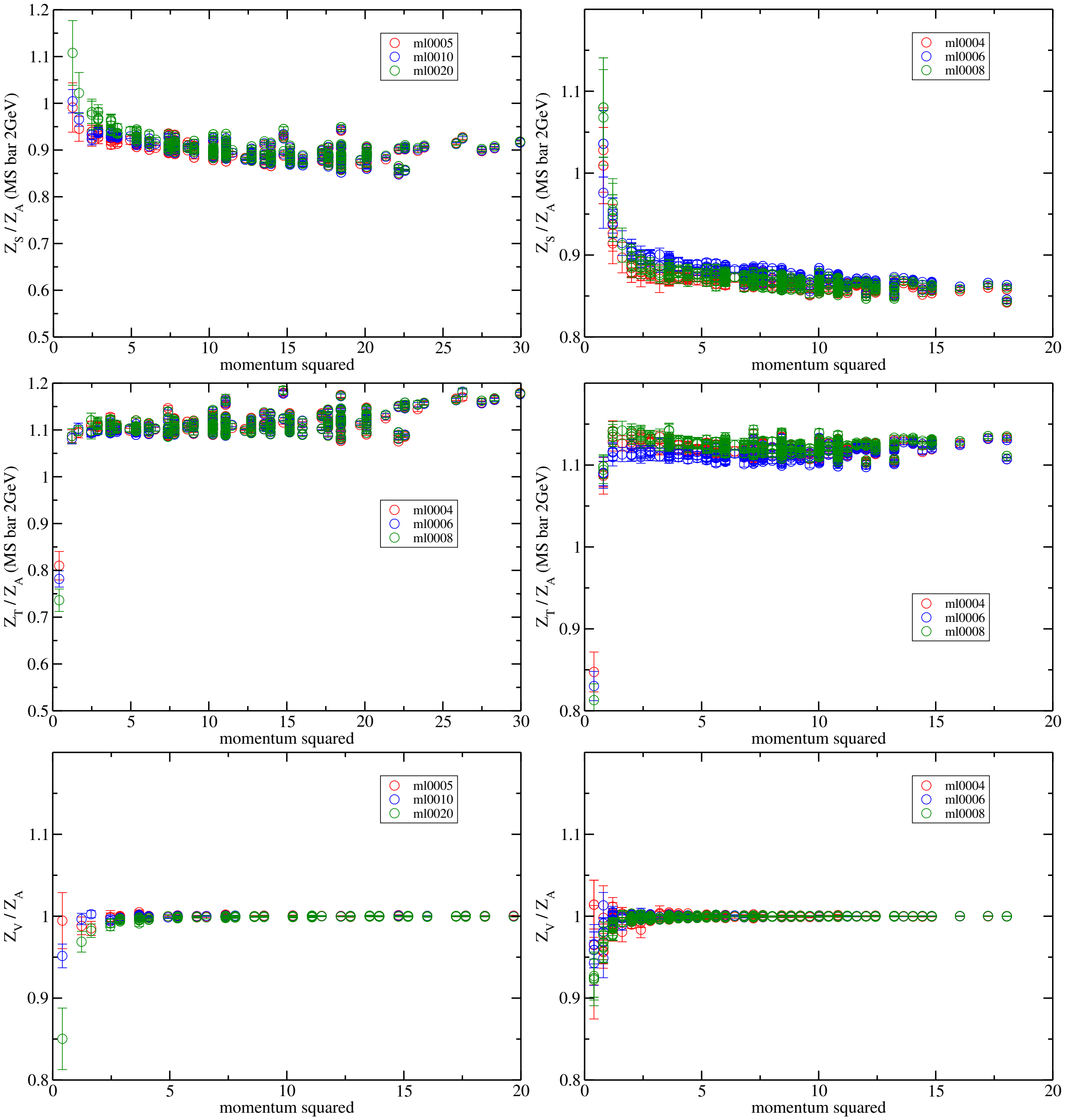

Fig. 4.6: Measured renormalization constants in the $\overline{\mathrm{MS}}$ scheme at 2 GeV as functions of the matching scale μ_0 with the three different light quark masses (red, blue, green circle respectively).

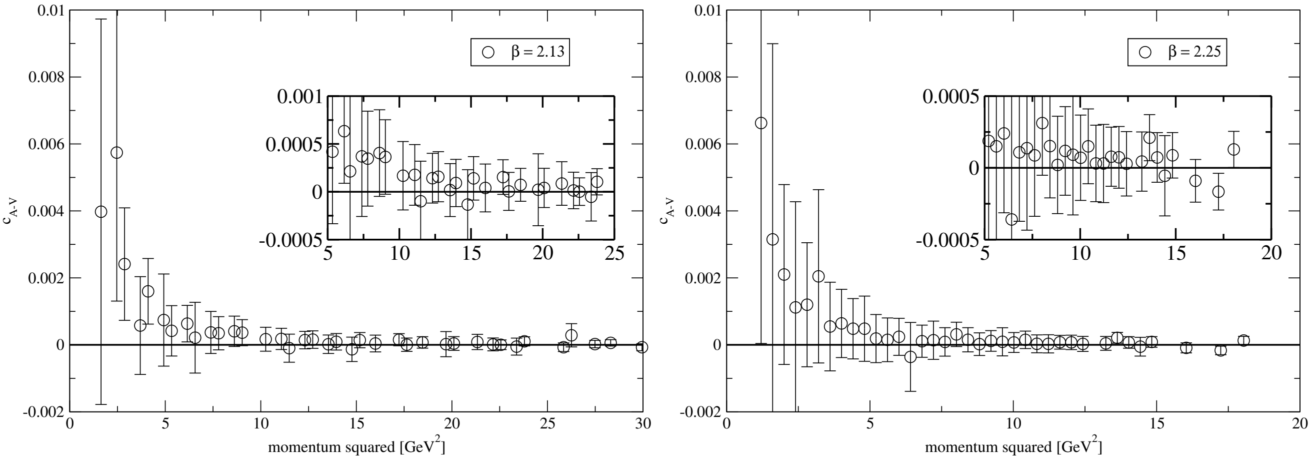

Fig. 4.7: The measured c_{A-V} in the chiral limit.

Chiral extrapolation

While the renormalization constant slightly depends on the mass of the fermion within the RI/SMOM scheme, we may evaluate the mass-independent part of Z_O^0 using following form

$$Z_O = Z_O^0 + c_O^1 m_{\text{val}} + c_O^2 m_{\text{val}}^2, \qquad \text{with} \quad m_{\text{val}} = m_l + m_{\text{res}}. \tag{4.14}$$

Even after the chiral extrapolation, the renormalization constant still depends on the matching scale μ_0. To eliminate the residual scale dependence, we adopt the fit ansatz as a function of μ_0 introduced in the previous chapter.

Hypercubic artifact

We demonstrate how large hypercubic artifacts are in bare vertex functions (Fig. 4.8) and ratios of renormalization constants (Fig. 4.9). In both cases, we observed the significant deviation between the raw data and the averaged data. Therefore we should eliminate hypercubic artifacts using the methods introduced in the previous chapter. Let us briefly summarize these methods again :

1. Averaging method : The single-valued function of μ_0 can be obtained by averaging the momentum configurations, though the result would be still highly contaminated from the hypercubic artifacts.
2. Subtracting method (used in Fig. 4.10) : In this method, the hypercubic artifact is eliminated by using the fit ansatz.

The difference between two methods can expose the hidden hypercubic artifacts. Here we will performed the global fit using the generalized ansatz,

$$\begin{aligned} Z(\mu_0) = {} & c_0 + c_2(a\mu_0)^2 \\ & + c_4(a\mu_0)^4 + (a\mu_0)^4 c_{4,i}^{(S)} S_{4,i} \\ & + c_6(a\mu_0)^6 + (a\mu_0)^6 c_{6,i}^{(S)} S_{6,i} \\ & + c_8(a\mu_0)^8 + (a\mu_0)^8 c_{8,i}^{(S)} S_{8,i} + (a\mu_0)^8 c_{8,8,ij}^{(SS)} S_{4,i} S_{4,j} + (a\mu_0)^8 c_{8,8,ij}^{(AA)} A_{4,i} A_{4,j}. \end{aligned} \tag{4.15}$$

channel	β	method	n	value	χ^2/D.O.F.	method	n	value	χ^2/D.O.F.
S	2.13	Averaging method	4	0.9586(266)	1.104	Subtracting method	4	0.9442(273)	0.4447
	2.13		6	0.9668(420)	1.129		6	0.9587(419)	0.05427
	2.13		8	0.9532(610)	1.155		8	0.9672(562)	0.02614
	2.25		4	0.8914(412)	0.1416		4	0.8905(378)	0.04154
	2.25		6	0.9185(667)	0.1143		6	0.8904(583)	0.01550
	2.25		8	0.9016(977)	0.1135		8	0.9089(875)	0.009537
T	2.13	Averaging method	4	1.1135(183)	2.419	Subtracting method	4	1.0984(195)	0.5567
	2.13		6	1.0929(265)	2.389		6	1.0985(284)	0.1503
	2.13		8	1.0777(369)	2.438		8	1.1039(369)	0.04829
	2.25		4	1.1195(284)	0.2554		4	1.1229(271)	0.07432
	2.25		6	1.1462(438)	0.1958		6	1.1266(403)	0.02334
	2.25		8	1.1092(610)	0.1541		8	1.1301(527)	0.01238

Table 4.5: The evaluated value of c_0 using the averaging and subtracting methods including up to $\mathcal{O}(\mu_0^n)$ terms.

with hypercubic parameters $c_{4,i}^{(S)}, c_{6,i}^{(S)}, c_{8,i}^{(S)} \cdots$ used in the subtracting method. As shown in Fig. 4.9, the result from the averaging method does not provide a smooth function of the matching scale squared μ_0^2 since it is not a single-valued function of μ_0. As shown in Fig. 4.10, using the subtracting method, the results become more smooth as including the higher power terms. We also summarize the evaluated value of c_0 in Tab. 4.5 using the averaging and subtracting methods. According to Tab. 4.5, the statistical uncertainties are comparable with each other, while the value of χ^2/D.O.F. becomes smaller for the subtracting method. As described in Ref. [54], the issue of the large χ^2 value hinders the precise determination of c_0. We have demonstrated that this problem can be overcome using the subtracting method especially for the case of the tensor channel at $\beta = 2.13$. We also found that the inclusion of higher order terms from $\mathcal{O}(\mu_0^4)$ to $\mathcal{O}(\mu_0^8)$ is not sensitive to the estimation of μ_0-independent term c_0. Therefore, we use the results from the subtracting method including up to $\mathcal{O}(\mu_0^4)$ terms as the final estimation.

Fit range dependence

We next examine the fit range dependence with a variation of $(\mu_0)_{\rm min}$ which is an infrared cutoff for a function of μ_0 since there are other two sources of the residual μ_0 dependence at the lower μ_0. Recall that μ_0 is the scale where we measured the renormalization constant in the RI scheme and then it is converted into the renormalization constant in the $\overline{\rm MS}$ scheme at the scale of 2 GeV. In this sense, the systematic error stemming from the truncation of the perturbation theory should be minimized near $\mu_0 = 2$ GeV. Therefore we should not exclude the data point with $\mu_0 \sim 2$ GeV. In other words, we should set the minimum value of μ_0 below 2 GeV. However, if the minimum value of μ_0 becomes too small, the non-perturbative effects that is represented by the negative power term of μ_0^2 can be non-negligible. We therefore examine the $(\mu_0)_{\rm min}$ dependence of the extracted c_0 value as shown in Fig. 4.11. We observed that there are no apparent fit range dependences with respect to the choice of $(\mu_0)_{\rm min}$. This fact implies that the systematic uncertainties stemming from the matching procedure with the perturbation theory are negligible compared with statistical uncertainties, and we thus quote only the statistical

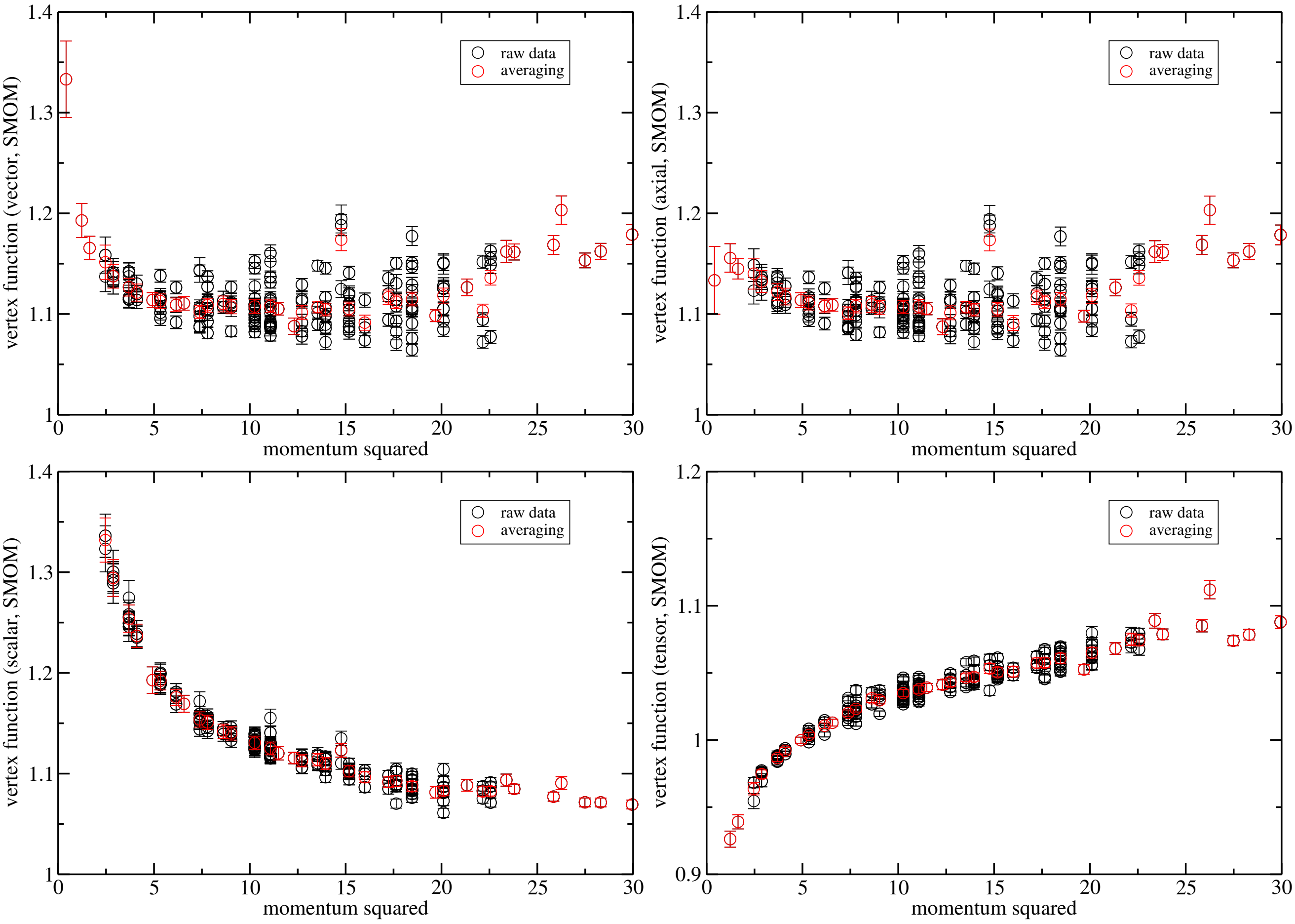

Fig. 4.8: Vertex functions in the vector(upper, left), axial(upper, right), scalar(bottom, left) and tensor(bottom, right) channel in the ml0020 ensemble.

error on the following relevant ratios

$$\frac{Z_S^{\overline{\mathrm{MS}}}(2\ \mathrm{GeV})}{Z_A} = 0.9442(273)_{\mathrm{stat}} \qquad \frac{Z_T^{\overline{\mathrm{MS}}}(2\ \mathrm{GeV})}{Z_A} = 1.0984(195)_{\mathrm{stat}} \qquad \beta = 2.13 \tag{4.16}$$

$$\frac{Z_S^{\overline{\mathrm{MS}}}(2\ \mathrm{GeV})}{Z_A} = 0.8905(378)_{\mathrm{stat}} \qquad \frac{Z_T^{\overline{\mathrm{MS}}}(2\ \mathrm{GeV})}{Z_A} = 1.1229(271)_{\mathrm{stat}} \qquad \beta = 2.25. \tag{4.17}$$

Together with $Z_A = 0.71651(46)$ for $\beta = 2.13$ and $Z_A = 0.74475(12)$ for $\beta = 2.25$ measured by RBC+UKQCD Collaboration [54], we finally obtained the renormalization constants for the scalar and tensor channels

$$Z_S^{\overline{\mathrm{MS}}}(2\ \mathrm{GeV}) = 0.6765 \pm 0.0196_{\mathrm{stat}} \qquad \beta = 2.13 \tag{4.18}$$

$$Z_T^{\overline{\mathrm{MS}}}(2\ \mathrm{GeV}) = 0.7870 \pm 0.0140_{\mathrm{stat}} \qquad \beta = 2.13 \tag{4.19}$$

$$Z_S^{\overline{\mathrm{MS}}}(2\ \mathrm{GeV}) = 0.6632 \pm 0.0282_{\mathrm{stat}} \qquad \beta = 2.25 \tag{4.20}$$

$$Z_T^{\overline{\mathrm{MS}}}(2\ \mathrm{GeV}) = 0.8362 \pm 0.0202_{\mathrm{stat}} \qquad \beta = 2.25. \tag{4.21}$$

These renormalization constants can be regarded as the continuum values. Therefore both results obtained from the coarse and fine lattices should be consistent with each other. There seem to be discrepancies between the measured values at different lattice spacings. Two results are still consistent with each others within large

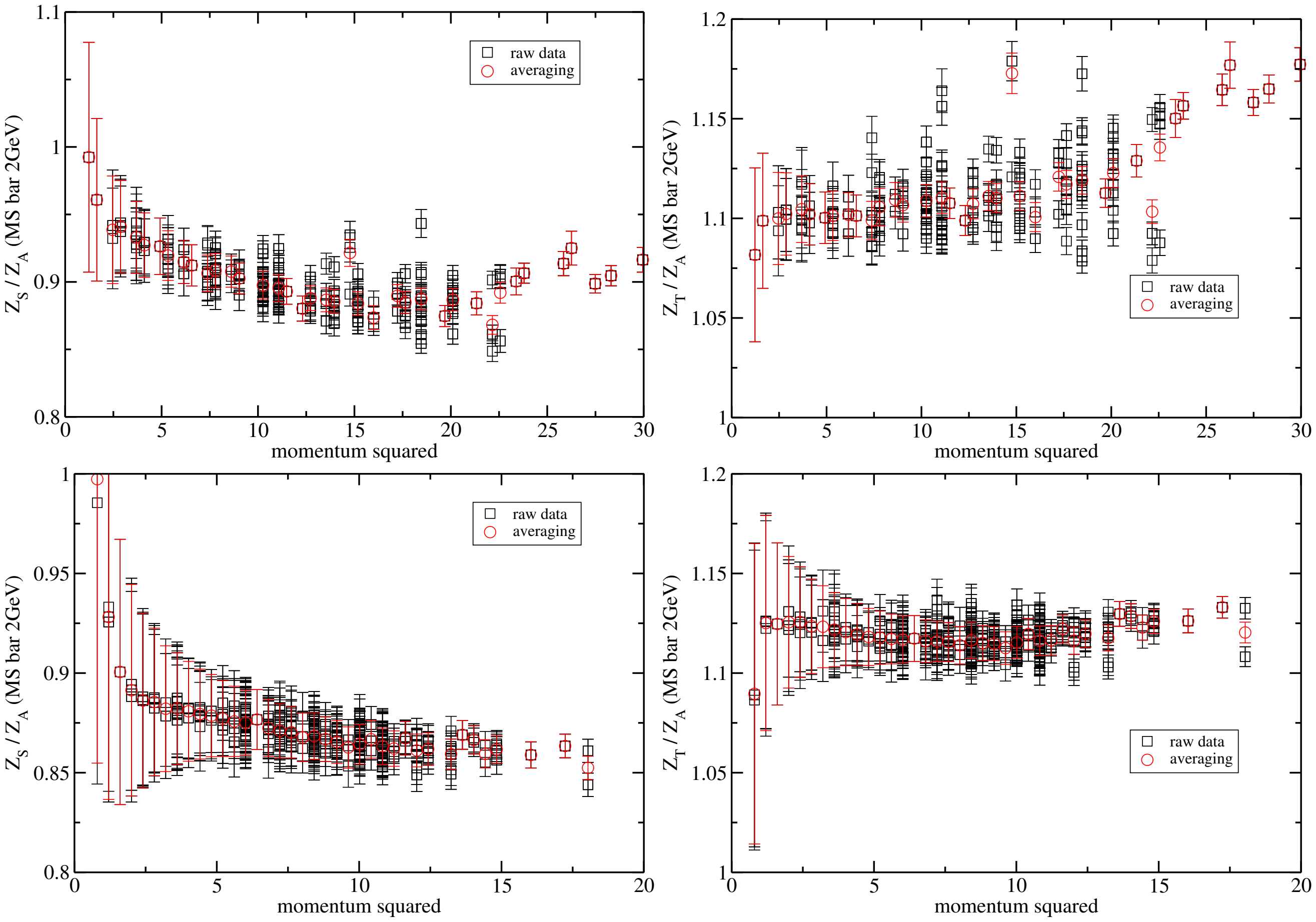

Fig. 4.9: Observed hypercubic artifacts at $\beta = 2.13$ (upper) and $\beta = 2.25$ (bottom). We compared the raw data and averaged data.

systematic uncertainties.

4.2.4 Renormalized coupling

The renormalized coupling constants calculated at each quark mass are summarized in Tab. 4.6. Although the $(a\mu_0)$-independent value obtained from the fit is regarded as the value in continuum theory, the bare coupling potentially receives the lattice discretization errors. In this sense, the renormalized coupling constant $g_O^{\text{ren}} = Z_O g_O^{\text{bare}}$ calculated at each lattice spacing might receive the lattice discretization error before taking the continuum limit. We also have to perform the chiral extrapolation because our simulated pion masses are heavier than the physical pion mass. Therefore, we have performed the combined chiral-continuum extrapolation with all data calculated with six different combinations of quark mass and lattice spacing.

Chiral & continuum extrapolation

In order to extract the value at the physical pion mass $m_\pi = 0.135$ [GeV], we should perform the chiral extrapolation. The physical quantity measured at the simulated pion mass m_π and the lattice spacing a

$$g_O(m_l \approx m_\pi^2, a) = C + Am_\pi^2 + Bm_\pi^4 + a^2\left(C' + A'm_\pi^2\right) + \cdots . \qquad (4.22)$$

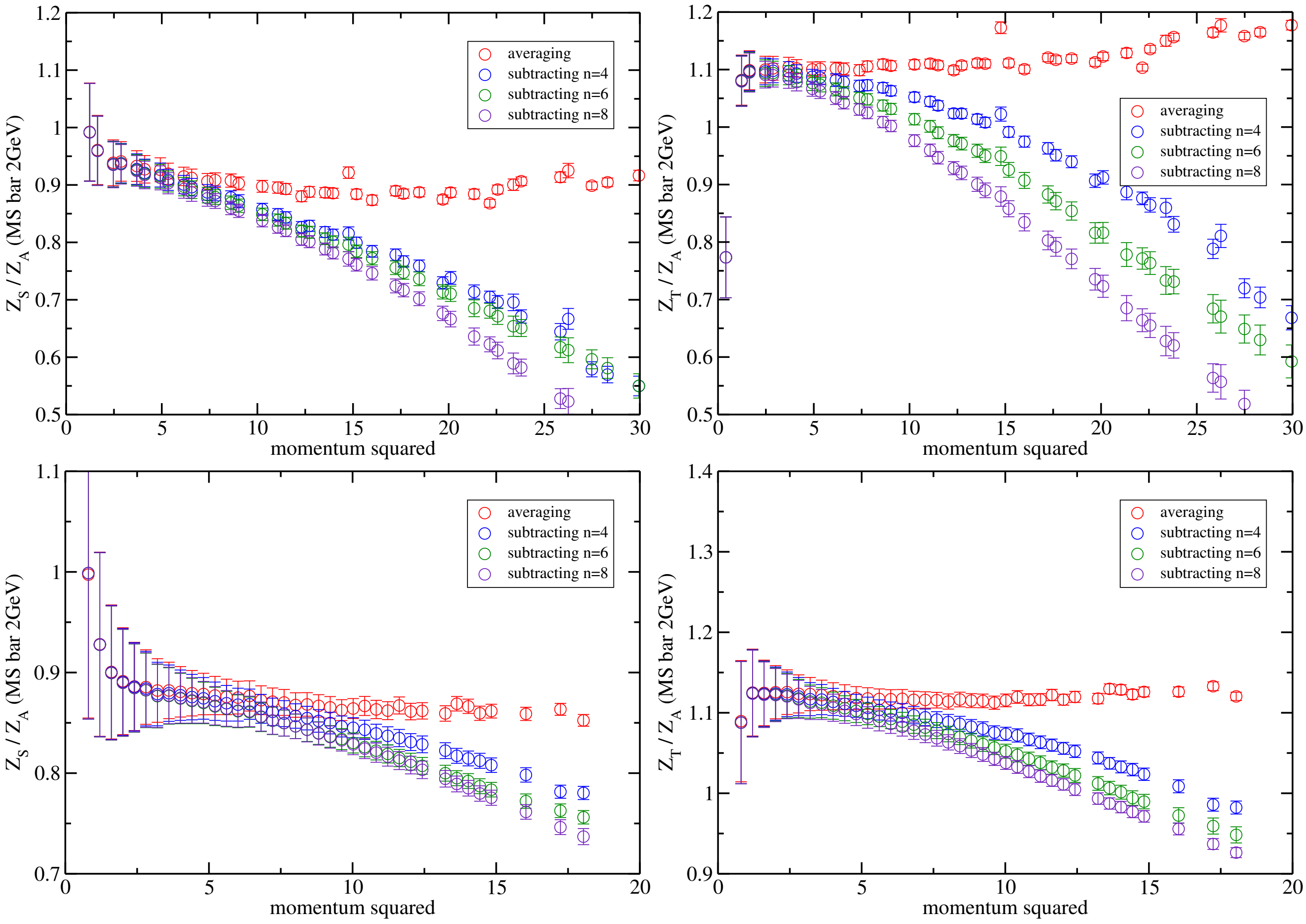

Fig. 4.10: Eliminating the hypercubic artifact at $\beta = 2.13$ (upper) and $\beta = 2.25$ (bottom): The black square represents the raw data in the chiral limit while the red circle is the result from the averaging method. The blue, green, and purple circle represent the data subtracted by the hypercubic artifact in $\mathcal{O}(a{\mu_0}^n)$ level respectively using the extrapolation method.

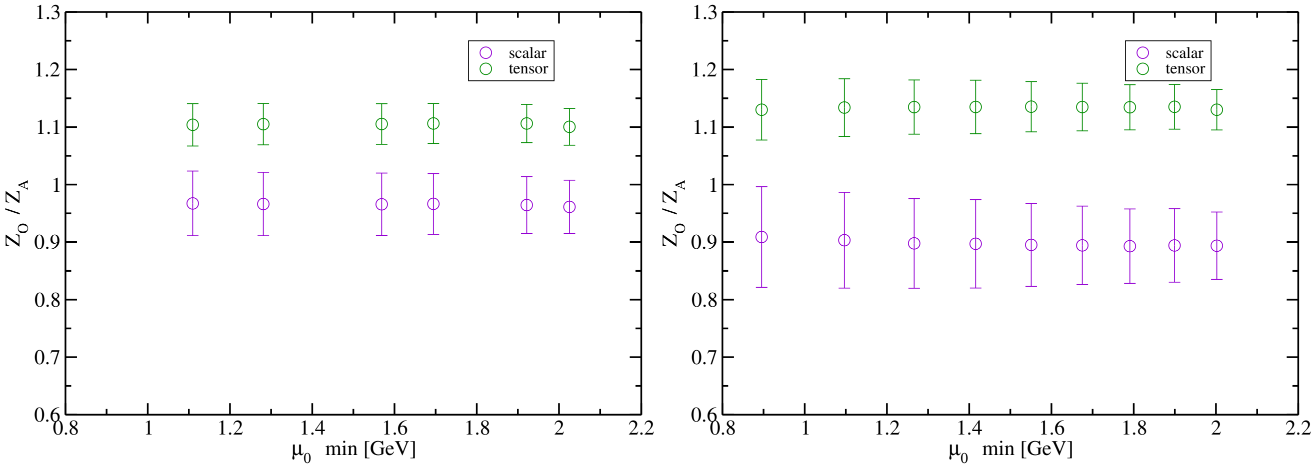

Fig. 4.11: The fit result for $\beta = 2.13$ (left) and $\beta = 2.25$ (right) as the function of μ_0 minimum

ID	g_A	g_S	g_T
ml0005	$1.224(66)_{\mathrm{stat}}$	$0.8551(2253)_{\mathrm{stat}}$	$1.155(66)_{\mathrm{stat}}$
ml0010	$1.164(48)_{\mathrm{stat}}$	$0.9633(1315)_{\mathrm{stat}}$	$1.084(49)_{\mathrm{stat}}$
ml0020	$1.189(38)_{\mathrm{stat}}$	$1.005(693)_{\mathrm{stat}}$	$1.169(45)_{\mathrm{stat}}$
ml0004	$1.300(88)_{\mathrm{stat}}$	$1.045(306)_{\mathrm{stat}}$	$1.161(82)_{\mathrm{stat}}$
ml0006	$1.214(40)_{\mathrm{stat}}$	$0.8728(1531)_{\mathrm{stat}}$	$1.105(45)_{\mathrm{stat}}$
ml0008	$1.148(34)_{\mathrm{stat}}$	$0.9928(1032)_{\mathrm{stat}}$	$1.089(41)_{\mathrm{stat}}$

Table 4.6: The renormalized coupling constants evaluated at each lattice spacing and fermion mass.

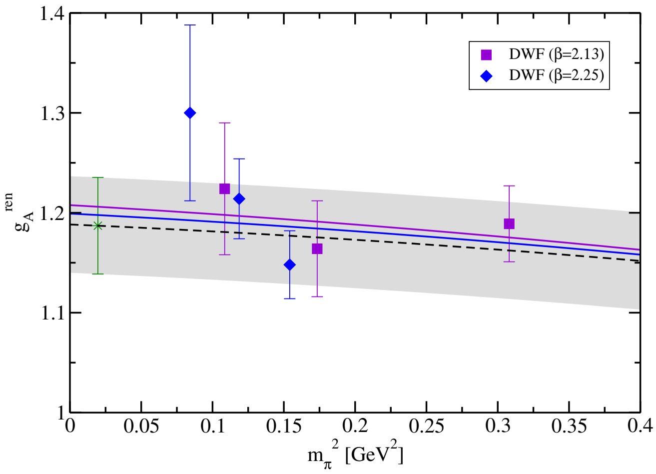

Fig. 4.12: The chiral & continuum extrapolated axial coupling.

where there is no a-odd term thanks to the absence of $\mathcal{O}(a)$ lattice artifact in DWFs. We use this formula to extract the continuum coupling constant at the physical pion mass.

Axial couplings

Our results of g_A as a function of the simulated pion mass show an upward trend as m_π decreases in the left panel of Fig. 4.12, although g_A in a chiral perturbation theory (ChPT) based formula used in [62, 63] always show a downward trend. This is one of the reason why we did not use the fit form expected in ChPT. We finally get

$$g_A = 1.19 \pm 0.05_{\mathrm{stat}}. \tag{4.23}$$

Scalar couplings

As shown in Fig. 4.13, the scalar coupling is known to receive the relatively large statistical error, since the scalar channel is highly sensitive to the vacuum fluctuation due to the non-zero value of the quark condensate. After the combined chiral-continuum extrapolation we finally get

$$g_S = 0.89 \pm 0.22_{\mathrm{stat}}. \tag{4.24}$$

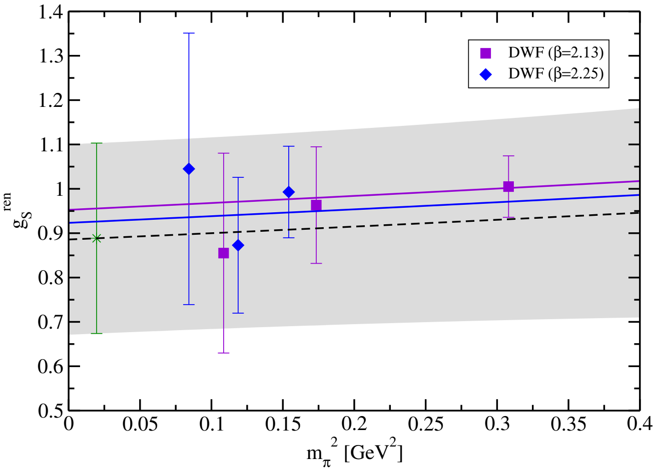

Fig. 4.13: The chiral & continuum extrapolated scalar coupling. In the left figure, we used the renormalized coupling constant determined by the μ_0-independent renormalization constant while we use the renormalized coupling constant determined at $\mu_0 = 2$ GeV.

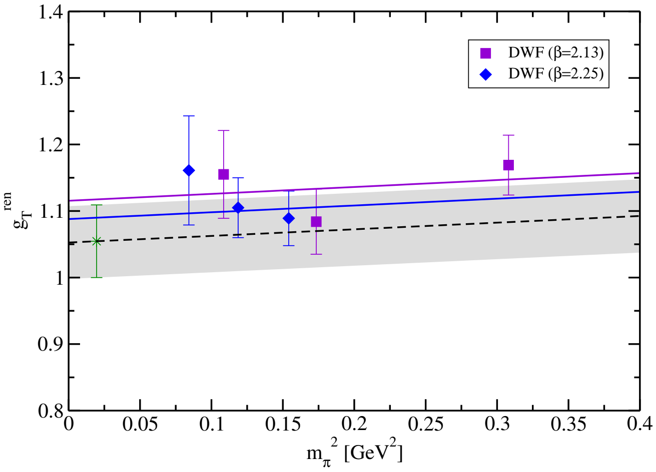

Fig. 4.14: The chiral & continuum extrapolated tensor coupling. In the left figure, we used the renormalized coupling constant determined by the μ_0-independent renormalization constant while we use the renormalized coupling constant determined at $\mu_0 = 2$ GeV.

Tensor couplings

Although we have only poor knowledge about the tensor coupling experimentally, the tensor coupling in lattice QCD can be measured precisely as well as the axial coupling. This is simply because the Dirac gamma structure is quite similar to the axial channel in the non-relativistic approximation. We obtain the continuum value of the tensor coupling at the physical pion mass as shown in Fig. 4.14 and get

$$g_T = 1.05 \pm 0.05_{\rm stat}. \tag{4.25}$$

Lattice artifact

A size of the lattice artifact on the isovector couplings can be estimated by the term of C' and A' appearing in Eq. (4.22). In the right panels of Fig. 4.12, 4.13 and 4.14 , purple and blue lines obtained from Eq. (4.22) with finite lattice spacing a while black solid line obtained with vanishing lattice spacing $a = 0$. The discrepancy between three lines indicates the magnitude of lattice artifact, and then the magnitude of lattice artifact is roughly estimated to be 10^{-2} which is consistent with the canonical estimation of $\mathcal{O}(a^2)$ lattice artifacts as $(a\Lambda_{\mathrm{QCD}})^2 \sim 10^{-2}$ with $\Lambda_{\mathrm{QCD}} \approx 0.2$ [GeV] as a typical scale parameter in QCD. On the other hand, the lattice artifact can be observed through the non-zero value of c_{A-V} whose typical size is estimated to be about 10^{-4} as shown in Fig. (4.7). Let us summarize the estimation of $\mathcal{O}(a^2)$ lattice artifacts:

- coupling constant : $\mathcal{O}(a^2) \sim 10^{-2}$
- canonical estimation : $\mathcal{O}(a^2) \sim 10^{-2}$
- c_{A-V} : $\mathcal{O}(a^2) \sim 10^{-4}$

4.3 Summary

We have calculated the nucleon isovector couplings, which are non-perturbatively renormalized using the RI/SMOM scheme, with three different light quark masses at two different lattice spacings using 2+1 flavor domain-wall fermions ensembles generated by RBC+UKQCD Collaborations. We finally obtain the results of the nucleon renormalized couplings in the axial, scalar and tensor channels as below.

$$g_A = 1.19 \pm 0.05_{\mathrm{stat}} \qquad g_S = 0.89 \pm 0.22_{\mathrm{stat}} \qquad g_T = 1.05 \pm 0.05_{\mathrm{stat}} \tag{4.26}$$

Chapter 5

Numerical results (Wilson-Clover Fermions)

In this chapter, we will show results calculated in 2+1 flavor QCD with Wilson-Clover fermions at the physical point. Although Wilson-clover fermions in general breaks chiral symmetry explicitly, the non-perturbative $\mathcal{O}(a)$-improvement with the stout smearing method would restore the chiral symmetry efficiently. Therefore the smeared Wilson clover fermions action are regarded as the fermion action with no doubler, and the chiral symmetry restored up to $\mathcal{O}(a^2)$.

5.1 Simulation Details

We mainly used the PACS10 configurations [64] generated by the PACS Collaboration with the stout-smeared $\mathcal{O}(a)$ improved Wilson-clover fermion and Iwasaki gauge action. Two lattice sizes are used for this study, 128^4 and 64^4, corresponding to linear spatial extent of approximately 10 and 5 fm (See also Tab. 5.1). The smaller volume ensembles are used only for computing the renormalization constant which is known to be less sensitive to the finite volume effects, while our main results of the nucleon matrix elements are obtained from the larger volume ensembles. We also show results of the bare nucleon coupling constants from the previous calculation [65, 66] of the PACS Collaboration using the HPCI configuration.

The simulation details are summarized in Tab. 5.1.

$L^3 \times T$	a^{-1} [GeV]	κ_l	κ_s	M_π [GeV]	configuration
$128^3 \times 128$	2.3	0.126117	0.124902	0.135 [67]	PACS10
$64^3 \times 64$	2.3	0.126117	0.124902	0.139 [64]	PACS10
$96^3 \times 96$	2.3	0.126117	0.124790	0.146 [66]	HPCI

Table 5.1: Simulation Details: $\kappa_{l(s)}$ denotes the hopping parameter of the light (strange) quark.

5.1.1 Improvement

Non-perturbative evaluation of $c_{SW} = 1.11$ for the smeared Wilson clover fermion and Iwasaki gauge action is reported in Ref. [68] and also the improved factor c_A for the axial-vector current is found to be close to zero within the statistical error. Although non-perturbative determination of c_T has not been performed yet, we do not consider $\mathcal{O}(a)$ improvement of the quark bilinear currents in this thesis.

$L^3 \times T$	t_{sep}/a	N_{conf}	# of meas.	$L^3 \times T$	t_{sep}/a	N_{conf}	# of meas.
$128^3 \times 128$	10	20	2560	$96^3 \times 96$	15	200	6400
	12	20	5120				
	14	20	6400				
	16	20	10240				

Table 5.2: The total number of measurements at each source-sink separation with two simulations

5.1.2 PACS10 configuration and measurement technique

The PACS Collaboration is now generating 2+1 flavor QCD configurations on very large lattice over (10 fm)^4. The PACS10 configurations are a series of such projects. At present the coarse 128^4 and fine 160^4 gauge configurations had been already generated. Once the relevant physical observables are measured with several different lattice spacings, the corresponding continuum values will be determined. The aim of the PACS10 project is to provide a comprehensive understanding over the the subjects associated the elemental particle and nuclear physics including the structure of the nucleon. Therefore, these configurations are the one of the milestones in fully dynamical lattice QCD simulations at the physical point.

Although the total number of the accumulated gauge configurations is not large, the huge lattice volume allows us to reduce the statistical error drastically. Since the nucleon three-point function can be evaluated only in a small part of the whole volume (typically $t_{\mathrm{sep}} \sim$ 1–1.5 fm), we can increase the number of measurements by calculating in spatially separated regions. Furthermore, we employ the all-mode-averaging (AMA) technique to reduce the statistical error significantly without increasing the computational costs. The measurement of the nucleon couplings are on going and currently achieved only with the coarse 128^4 configuration.

5.2 Nucleon matrix element

The nucleon matrix element measured on the PACS10 configurations in the vector and axial channels had been reported in Ref. [67]. In this thesis we focus on the scalar and tensor couplings constants. The bare coupling constant had been also measured on the HPCI configurations [64]. We summarize the details of all measurement that are performed in this thesis in Tab. 5.2.

We calculate the three-point functions with four different source-sink separations $t_{\mathrm{sep}}/a = 10, 12, 14, 16$ with the PACS10 configurations while the three-point functions had been calculated with a single source-sink separation $t_{\mathrm{sep}}/a = 15$ on the HPCI configurations. The saturation of the ground state contribution in the three-point functions can be confirmed in the conventional plateau method through the variation of t_{sep}.

5.2.1 Exponential smearing

As similar to the case of DWFs, we use the smearing method in order to statistically improve the nucleon interpolating operator

$$N(x) = \int d\mathbf{y}_1 \int d\mathbf{y}_2 \int d\mathbf{y}_3 \left(q(\mathbf{y}_1, x_4)^T C\gamma_5 q(\mathbf{y}_2, x_4)\right) q(\mathbf{y}_3, x_4) \prod_{i=1}^{3} \theta(\mathbf{x} - \mathbf{y}_i). \tag{5.1}$$

$L^3 \times T$	t_{sep}	g_S	g_T	Fit-range	$L^3 \times T$	t_{sep}	g_S	g_T	Fit-range
$128^3 \times 128$	10	0.8225(2741)	1.0894(191)	[3:7]	$96^3 \times 96$	15	1.117(407)	0.985(55)	[6:9]
	12	0.8889(1865)	1.0250(222)	[4:8]					
	14	0.8098(5588)	0.9851(436)	[5:9]					
	16	0.9691(4366)	0.9997(633)	[6:10]					

Table 5.3: The measured bare coupling constant.

In these simulations, we adopt the exponential source $\theta(\mathbf{x}-\mathbf{y}_i) = A\exp\left(-B\left|\mathbf{x}-\mathbf{y}_i\right|\right)$ with $\{A, B\} = \{1.2, 0.16\}$ for PACS10 and $\{1.2, 0.11\}$ for HPCI. One of the differences between the Gaussian smearing used for the DWFs calculations and the exponential smearing is that the exponential smearing used here is not performed in the gauge-covariant way. In order to obtain the expectation value, we fix the gauge by imposing Coulomb gauge. We then can compute the relevant three- and two-point correlation functions using the exponentially smeared source and the sink.

5.2.2 Bare couplings

The bare coupling constants can be evaluated using the smeared three- and two- point functions C_{3pt}^{SS} and C_{2pt}^{SS}

$$\frac{C_{\mathrm{3pt}}^{SS}(t_{\mathrm{sink}}, t, t_{\mathrm{src}})}{C_{\mathrm{2pt}}^{SS}(t_{\mathrm{sink}} - t_{\mathrm{src}})} \to g_O \qquad \text{for} \qquad t_{\mathrm{sink}} \gg t \gg t_{\mathrm{src}} \tag{5.2}$$

as similar to the case of the DWFs. We show an example for the insertion time dependence on the three-point correlation functions divided by the nucleon two-point function in Fig. 5.1. The measured values are tabulated in Tab. 5.3 and their t_{sep} dependences are shown in Fig. 5.2.

5.3 Renormalization constant

Although we repeat the similar analysis to the case of the DWF, the details of the analysis are bit different. We list differences :

- Both of the Z_A and Z_V are determined by the Schrödinger functional method.
- Since the chiral symmetry is not manifest for Wilson-clover fermions, we have to examine how much the chiral symmetry is broken.
- As reported in Ref. [50], the quark propagator computed with Wilson-clover fermions is less affected by the hypercubic artifacts in comparison with the chiral fermions such as the DWFs or overlap fermions. Since the chiral fermions does not receive $\mathcal{O}(a)$ lattice artifact, it sounds strange. This issue is still opened.
- The calculations presented in this chapter are performed only at a single lattice spacing. Thus we can not take the continuum limit.

The last point is crucial. Although we have the results obtained at the single lattice spacing, we would like to estimate some discretized error by comparing the renormalization constant measured in other schemes since the scheme dependence can be regarded as a size of uncertainties stemming from the lattice artifacts. Therefore we adopt the both of the RI/SMOM and RI/SMOMγ schemes. Moreover, the individual renormalization constant will be obtained from both of two ratios Z_O/Z_A and Z_O/Z_V. Then the renormalization constant will be evaluated

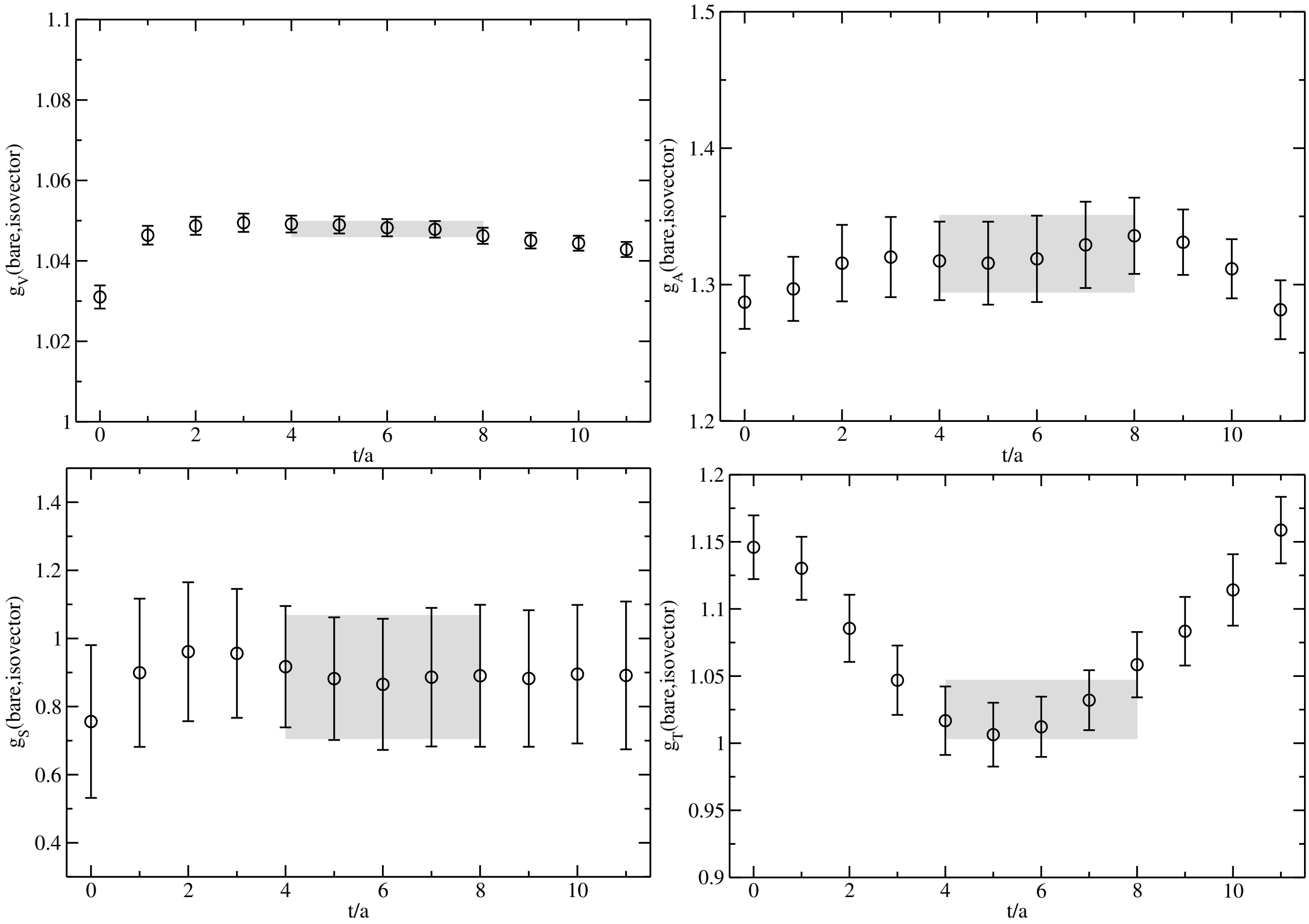

Fig. 5.1: The insertion time dependence on the ratio of the nucleon three-point and two-point function for the vector (upper, left), axial (upper, right) scalar(bottom, left), tensor(bottom, right) channels in the case of $t_{\text{sep}}/a = 12$. The values in the plateau region correspond to the respective bare couplings.

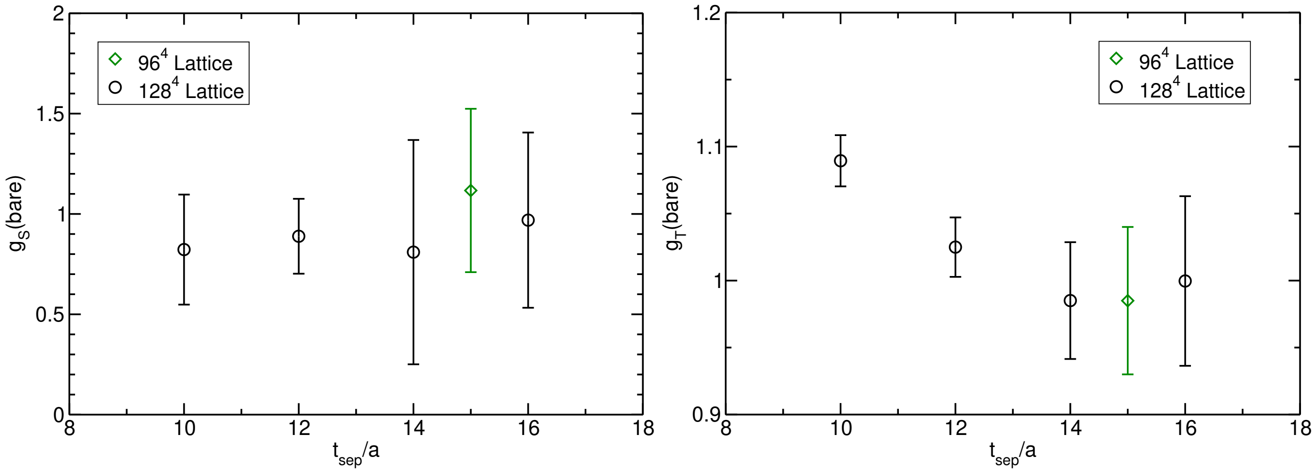

Fig. 5.2: The measured bare coupling constant with the several t_{sep}.

in four different ways,

$$Z_O^{\mathrm{RI/SMOM}(\gamma),V(A)} = \frac{\Lambda_{V(A)}^{\mathrm{Tr,RI/SMOM}(\gamma)}}{\Lambda_O^{\mathrm{Tr,RI/SMOM}(\gamma)}} Z_{V(A)}, \tag{5.3}$$

where we define $\Lambda_O^{\mathrm{Tr},i}$ as the traced three-point functions

$$\Lambda_O^{\mathrm{Tr},i} = \frac{1}{3\cdot 4}\mathrm{Tr}\left[\mathcal{P}_O\Lambda_O\right]_i \qquad\qquad i = \mathrm{SMOM}, \mathrm{SMOM}\gamma. \tag{5.4}$$

We can estimate the systematic uncertainties due to the lattice artifacts by comparing the results obtained from different procedures.

5.3.1 Hypercubic artifact

In order to estimate the hypercubic artifact, we first compare the results given by the averaging method with the raw data (Fig. 5.3). Recall that the vertex function is described by a function of two external momenta p_1 and p_2. Therefore, it depends not only on the scale μ_0 which is defined as $\mu_0 = p_1^2 = p_2^2 = (p_1 - p_2)^2$ but also on the hypercubic parameters as described in Chap. 3. The averaged data are obtained from averaging over the hypercubic parameters. The figures show no clear difference between the raw data and averaged data within the statistical errors unlike the case of DWFs. This implies that the hypercubic artifacts are negligibly small for the simulations studied in this chapter and the averaged data may be regarded as the single-valued function of the scale μ_0. Then the analysis where the hypercubic effect is taken into account is not necessary in this chapter.

5.3.2 Test for the chiral symmetry

In the case of Wilson-clover fermions, the chiral symmetry is not manifest with vanishing fermion mass, and the relation of $Z_V = Z_A$ may not be exactly satisfied as shown in Fig. 5.4. In fact, Z_V and Z_A measured by the Schrödinger functional method (denoted as Z_V^{SF} and Z_A^{SF}) are not fully consistent with each others. Indeed, it is found that c_{A-V} defined in Eq. (4.13) is -0.01405 ± 0.00714 for the SF scheme. In Fig. 5.5, we show c_{A-V} calculated with the RI schemes together with the corresponding value from the SF scheme (blue horizontal line). Although there is some scheme dependence on c_{A-V}, a typical size of c_{A-V} is quite small as being an order of 10^{-2}. This implies the chiral symmetry is efficiently restored in the stout-smeared Wilson-clover fermions adopted for the PACS10 and HPCI gauge configurations.

Note that the magnitude of lattice artifact can be roughly estimated by determination of the typical size of c_{A-V}. According to Fig. 5.5, c_{A-V} is estimated to be less than 5×10^{-2} in the RI/SMOM and SF schemes while c_{A-V} is estimated to be about 10^{-2} in the RI/SMOM$_\gamma$ scheme. Therefore, the typical size of lattice artifacts is given by $\mathcal{O}(a) \sim 10^{-1}$–$10^{-2}$ which is consistent with $\mathcal{O}(a^2) \sim 10^{-2}$–$10^{-4}$ estimated in the cases of DWFs.

5.3.3 Scheme and channel dependence

We show the renormalization constant as a function of the matching scale μ_0 in Fig. 5.6 for the scalar channel, 5.7 for the tensor channel. Each panel in both of Fig. 5.6 and Fig. 5.6 is given with the different RI scheme and input value of Z_V or Z_A from the SF scheme. We also compare the individual renormalization constants of Z_T

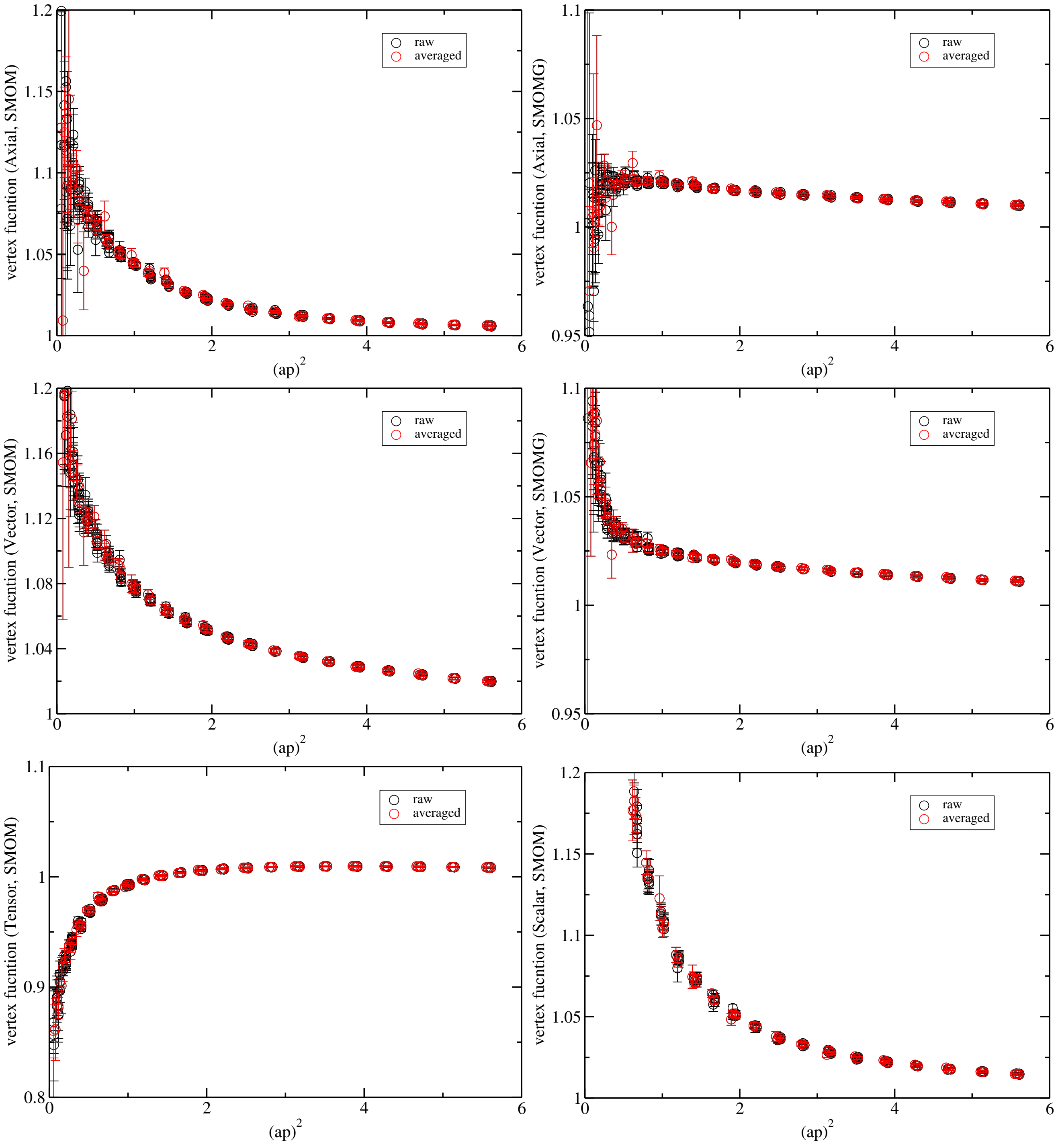

Fig. 5.3: The vertex function as the function of the scale. The black circle represents the raw data while the red circle is obtained after averaging the momentum configurations at the same $(ap)^2$.

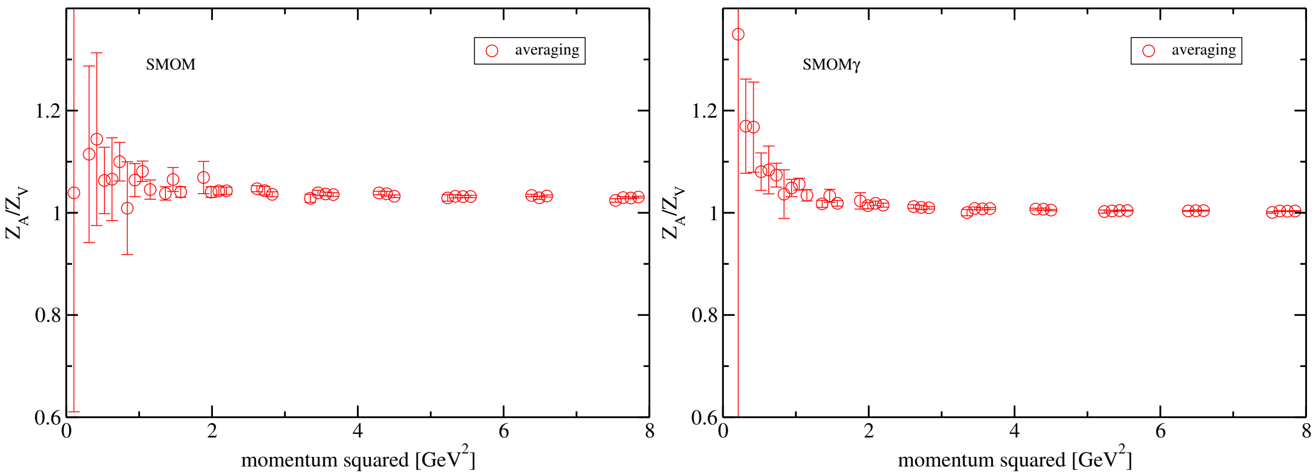

Fig. 5.4: The ratio of renormalization constants $\frac{Z_A}{Z_V}$ as the function of the scale. We used the RI/SMOM(left) and RI/SMOM$_\gamma$(right) schemes. The red circle is obtained by averaging the momentum configurations at the same μ_0. If the chiral symmetry is manifest, the ratios $\frac{Z_V}{Z_A}$ and $\frac{Z_A}{Z_V}$ are may be unity in any scheme. In the case of the Wilson-clover fermions, these ratios are supposed to be close to unity because of the restored chiral symmetry.

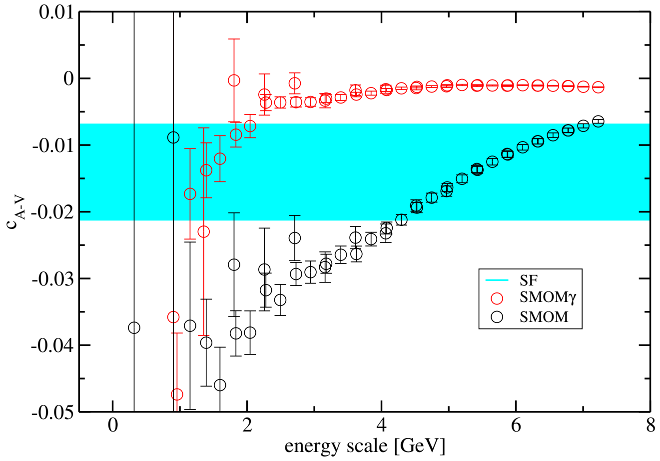

Fig. 5.5: The energy scale dependence of c_{A-V}.

and Z_S determined by four different ways in Fig 5.8. As shown in these figures, the renormalization constant still depends on the matching scale as same as the case of DWFs. Since the pole-like structure is observed in the renormalization constant measured especially in the RI/SMOM scheme, we then adopt the following functional form of the residual matching scale dependence so as to determine the μ_0 independent contribution

$$Z_O = \frac{c_{-2}}{(a\mu_0)^2} + c_0 + c_2(a\mu_0)^2 + c_4(a\mu_0)^4 \tag{5.5}$$

which includes a negative power term of $(a\mu_0)^2$. In the case of the DWFs, we examined the contributions from the higher order terms and found that the inclusion of the higher order terms beyond $\mathcal{O}(\mu_0^6)$ is not sensitive to the estimation of μ_0-independent term c_0 within the statistical uncertainties. Moreover, in the case of Wilson-clover fermions, it is observed that the renormalization constants seem to mildly depend on μ_0 in the high μ_0 region. Therefore the higher order contributions were not included in Eq. (5.5).

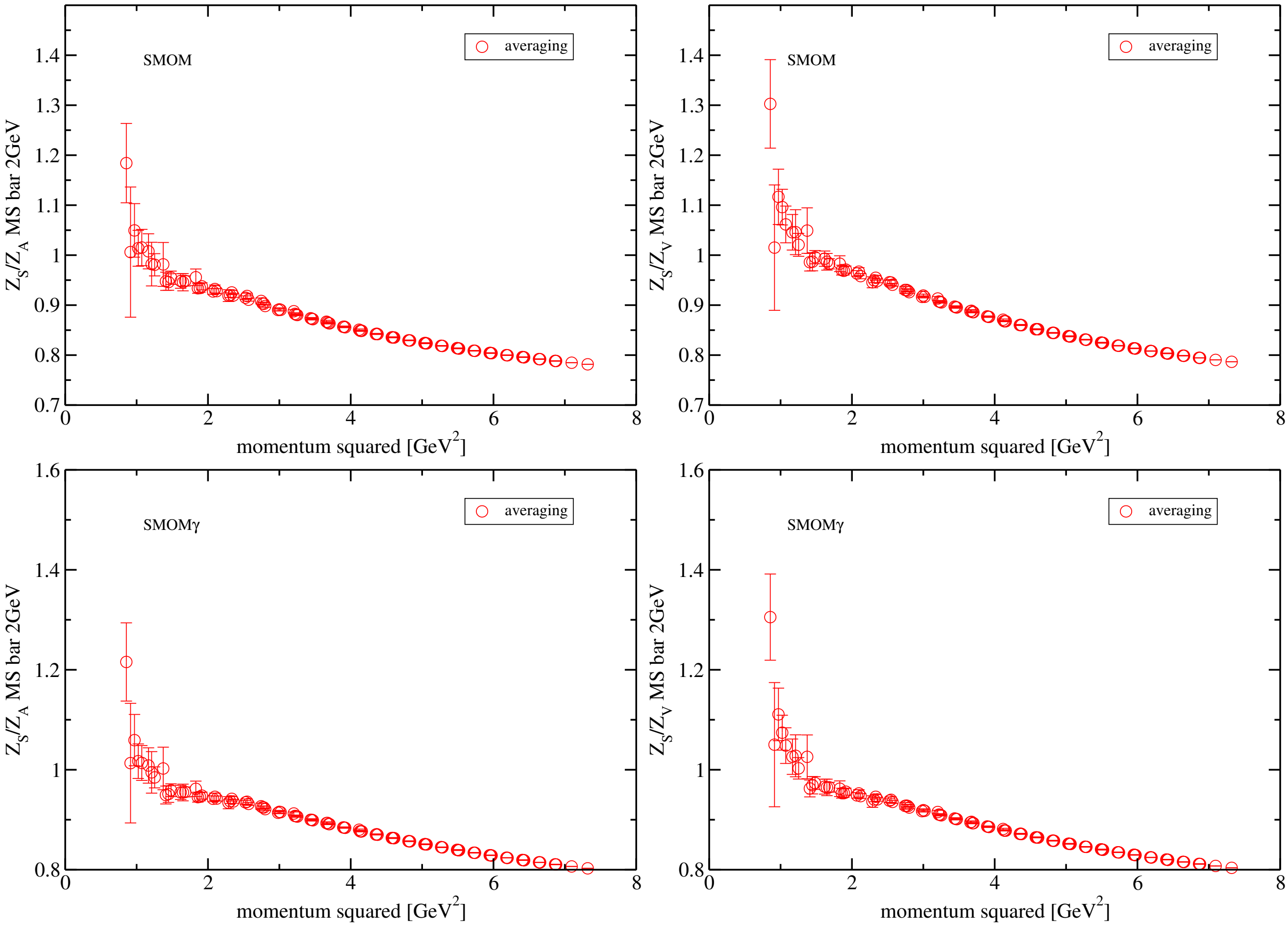

Fig. 5.6: The ratios of renormalization constants $\frac{Z_S}{Z_A}$(left), $\frac{Z_S}{Z_V}$(right) as the function of the intermediate scale μ_0. We used the RI/SMOM(upper) and RI/SMOM$_\gamma$(bottom) schemes as the intermediate scheme.

We first performed the global fit using Eq. (5.5) in the range of $1 < \mu_0 < (\mu_0)_{\rm max}$ with variations of $(\mu_0)_{\rm max}$. We evaluate the μ_0-independent term c_0 in each combination as summarized in Tab. 5.4. In Fig. 5.9, we show typical fit results for SMOM and SMOM$_\gamma$ with $Z_V^{\rm SF}$ given with the fit range $1 < \mu_0 < 4$ [GeV]. The fit results with the form Eq. (5.5) are represented by gray shaded curves. Blue dashed curves are given after the pole contribution is subtracted. The constant term c_0 can be read off from the blue dashed curve as y-axis intercept in each panel.

We next examine the model-dependence of the negative power terms. Here we use the simple form $c_0 + c_1\mu_0^2 + c_2\mu_0^4$ to find an appropriate fitting range of $\mu_{\rm min} < \mu_0 < \mu_{\rm max}$ where the effect of the negative power term should be negligible. We show the results of c_0 as the function of $\mu_{\rm min}$ in Fig. 5.10 5.11 5.12 5.13. In these figures, the red, green and blue circles represent the extracted c_0 using the simple form $c_0 + c_1\mu_0^2 + c_2\mu_0^4$ in the range of $\mu < \mu_0 < \mu_{\rm max}$ while the black circle represents the extracted c_0 using the global fit form Esq. (5.5) in the range of $1 < \mu_0 < \mu$ as tabulated in Tab. 5.4. In general, the obtained c_0 are consistent with the global analysis with the negative power term if $\mu_{\rm max}$ is set large enough. In this sense, the contribution from the pole term is enough small to neglect except for the low μ_0 region.

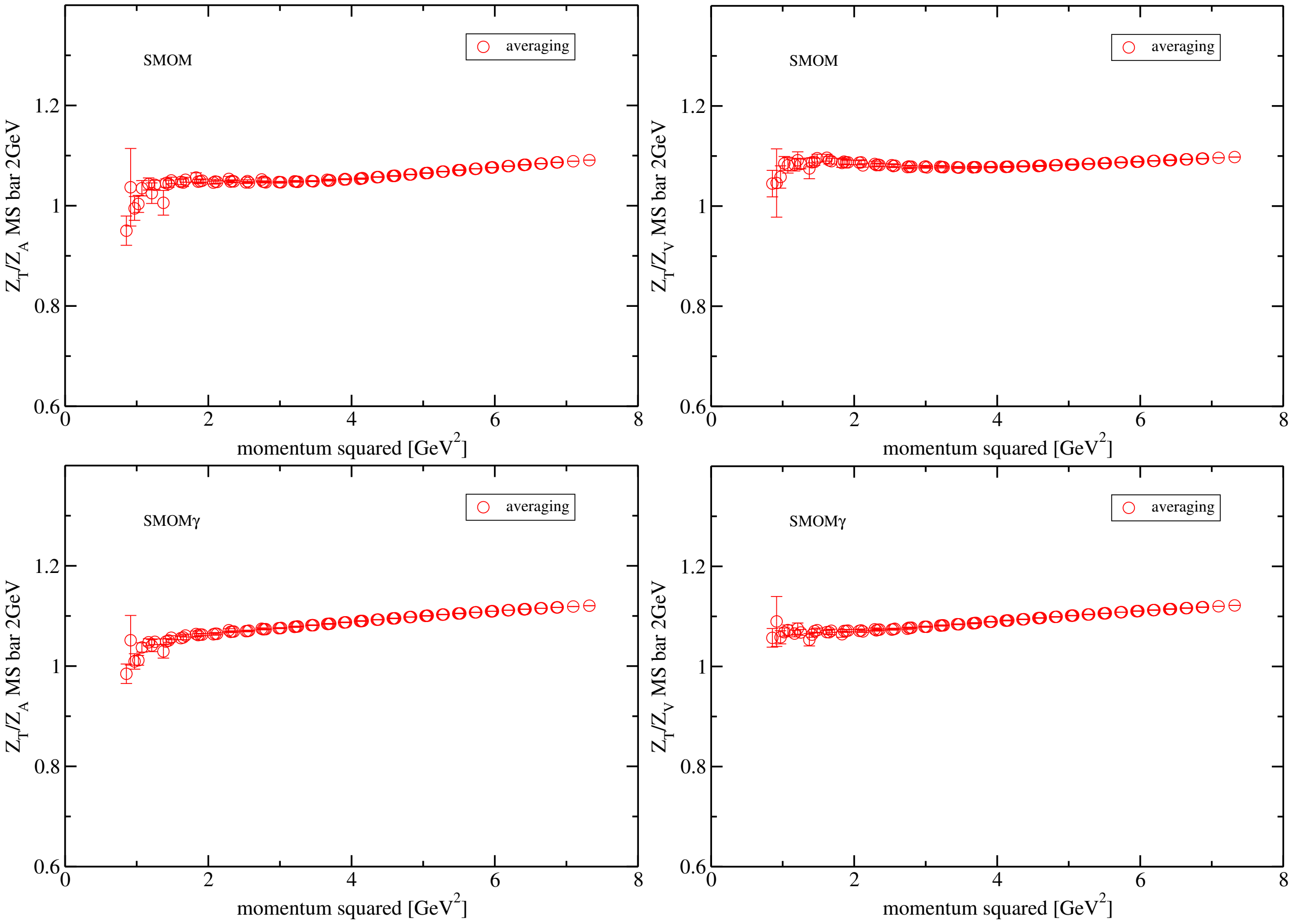

Fig. 5.7: The ratio of renormalization constants $\frac{Z_T}{Z_A}$(left), $\frac{Z_T}{Z_V}$(right) as the function of the intermediate scale μ_0. We used the RI/SMOM(upper) and RI/SMOM$_\gamma$(bottom) schemes as the intermediate scheme.

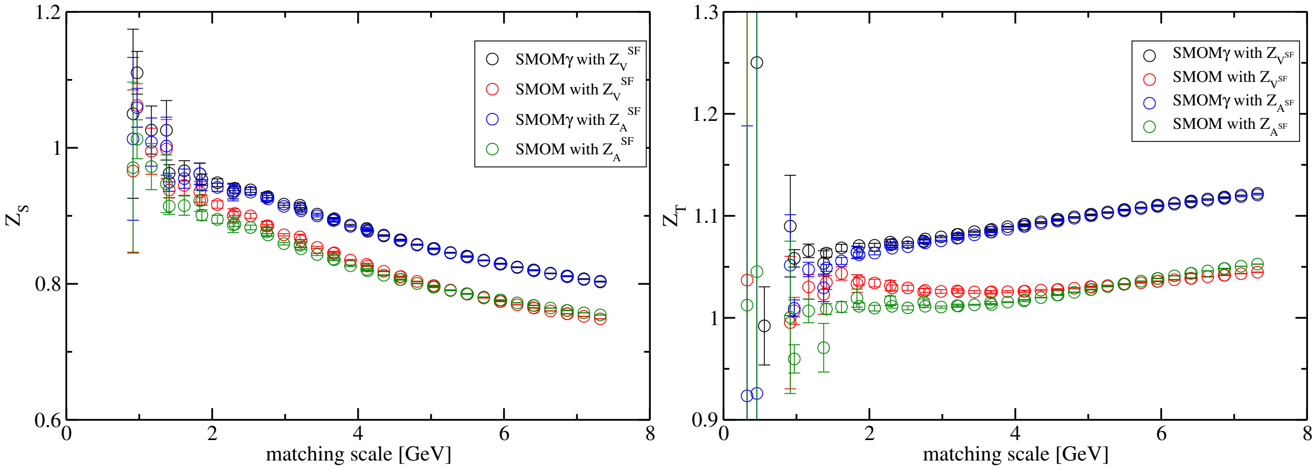

Fig. 5.8: The renormalization constant in the four different scheme and channels. We observed that the difference between the result using the axial and vector channel is slight in the case of the RI/SMOM$_\gamma$ scheme. On the other hand, in the case of RI/SMOM scheme, the renormalization constants which are obtained from two ratio Z_O/Z_A and Z_O/Z_V apparently differ from each others.

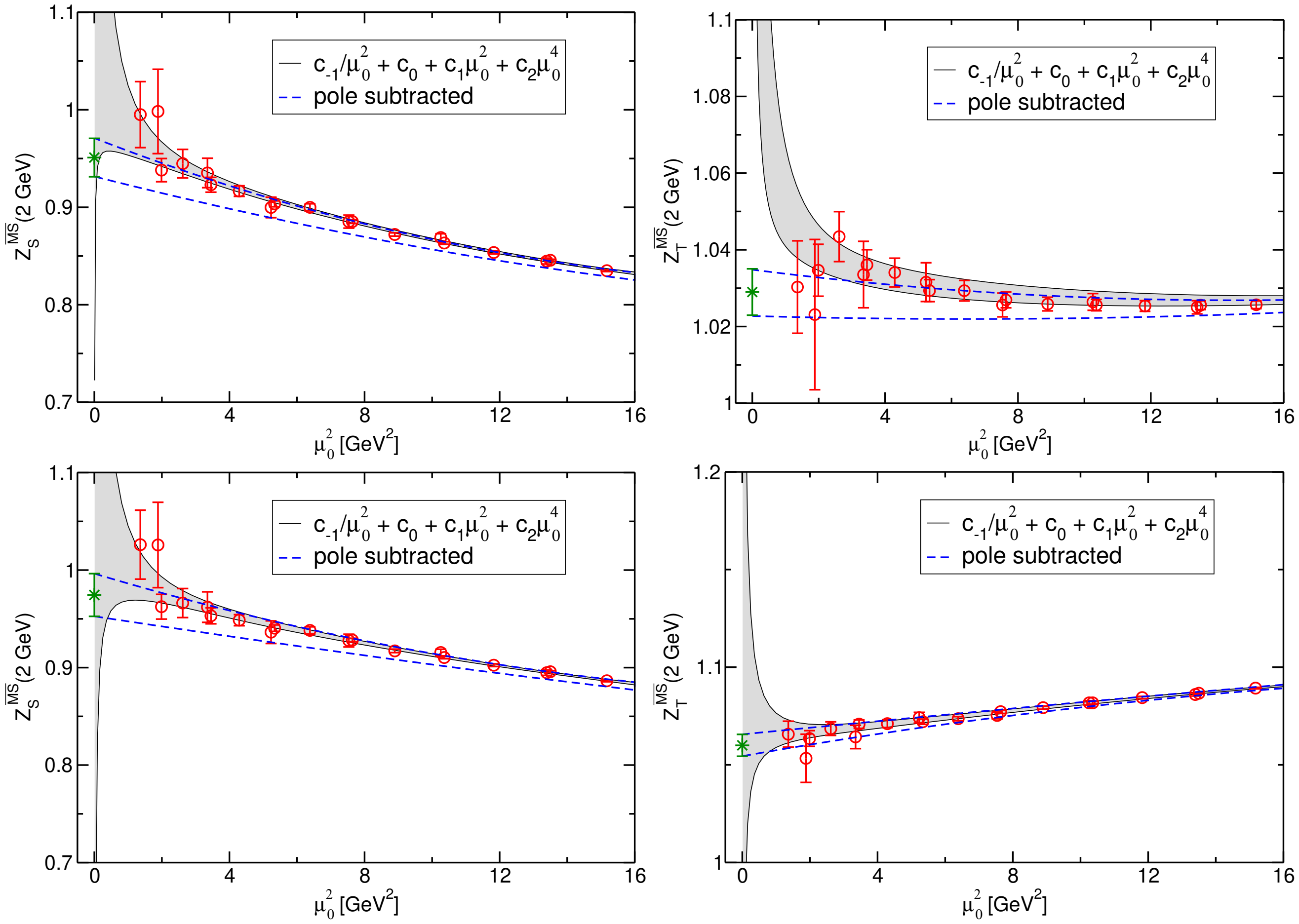

Fig. 5.9: Fit results using the RI/SMOM (upper) and RI/SMOM$_\gamma$(bottom) schemes with Z_V^{SF}. The green star corresponds the value of c_0. We chose these results as the central values of our final evaluation. Inner and outer error-bars of the green star represent the statistical and systematical uncertainties respectively.

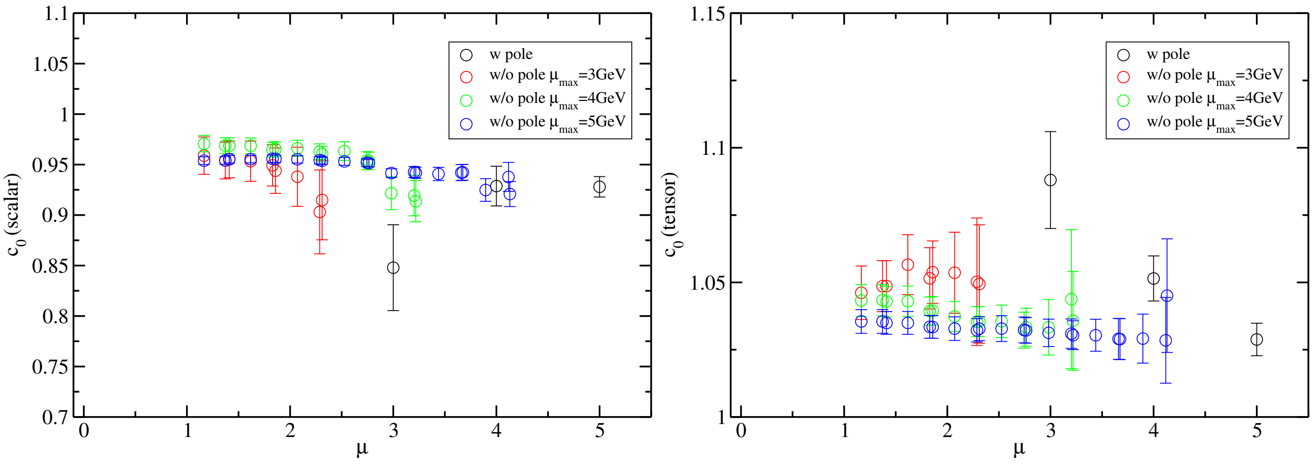

Fig. 5.10: Extracted μ_0-independent Z_S (left) and Z_T (right) using the RI/SMOM scheme with Z_V^{SF}.

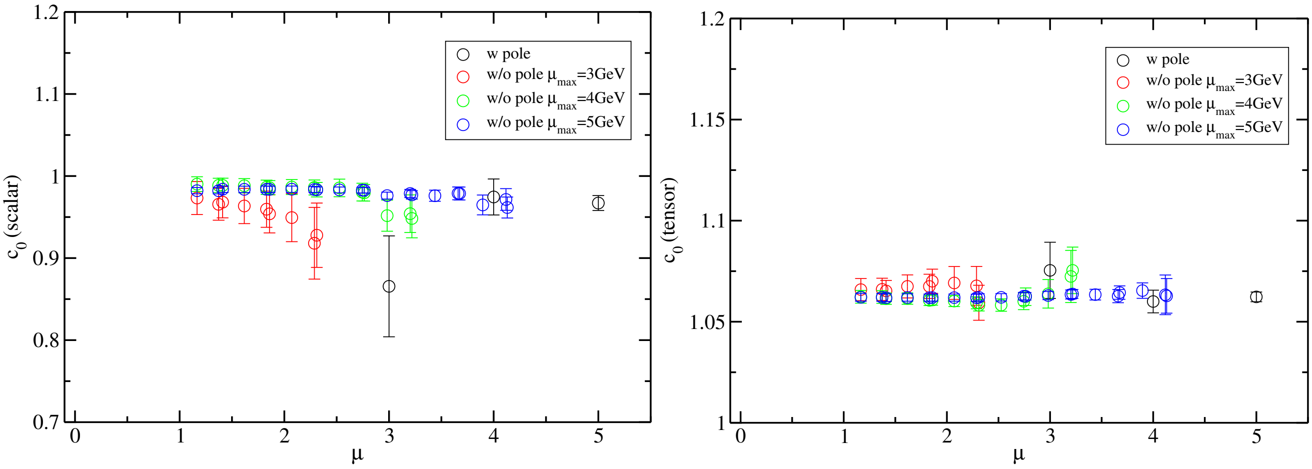

Fig. 5.11: Extracted μ_0-independent Z_S (left) and Z_T (right). using the RI/SMOM$_\gamma$ scheme with $Z_V^{\rm SF}$.

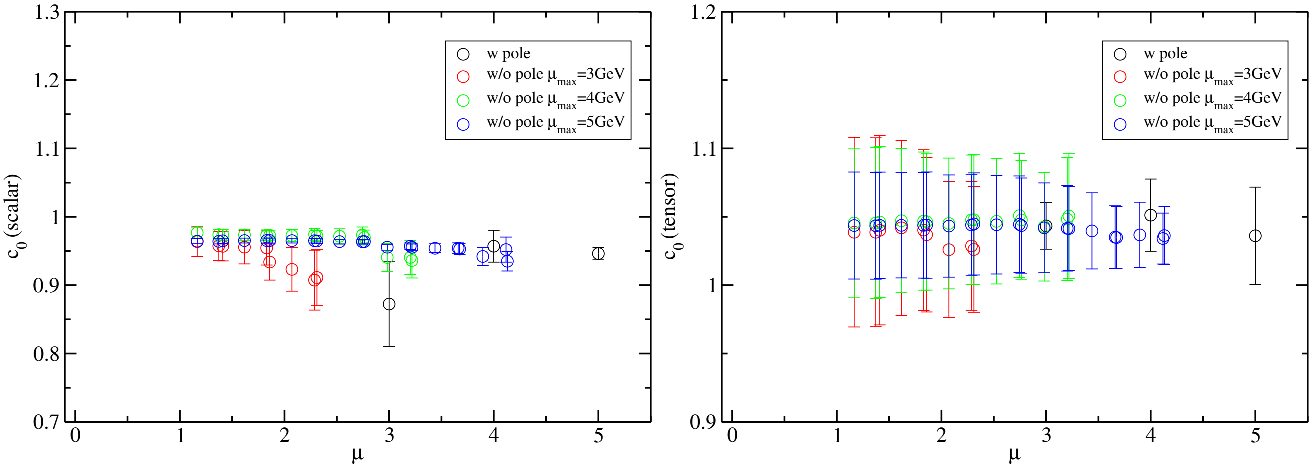

Fig. 5.12: Extracted μ_0-independent Z_S (left) and Z_T (right) using the RI/SMOM scheme with $Z_A^{\rm SF}$.

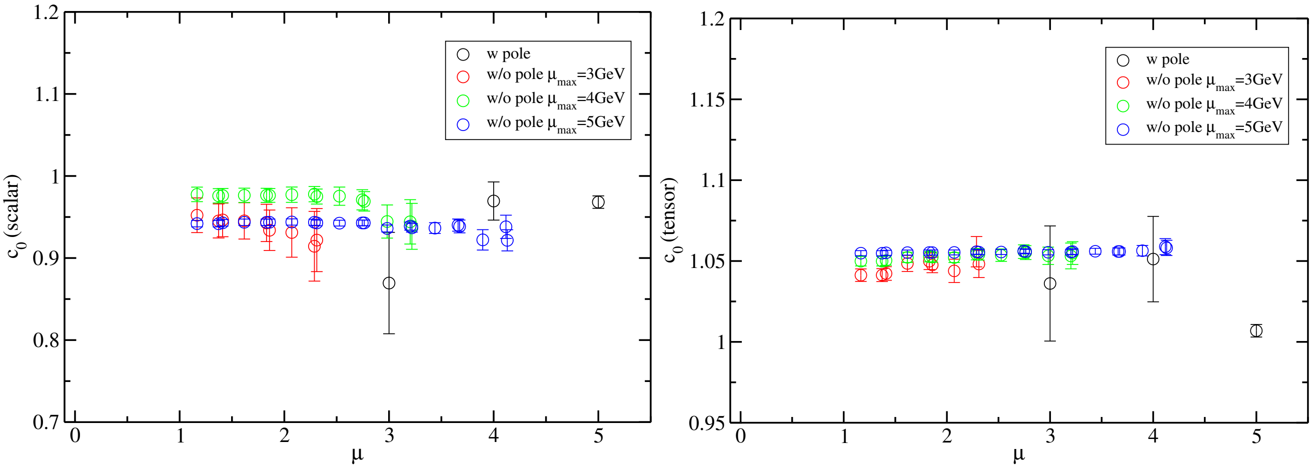

Fig. 5.13: Extracted μ_0-independent Z_S (left) and Z_T (right). using the RI/SMOM$_\gamma$ scheme with $Z_A^{\rm SF}$.

Γ	Type of SF input	Type of scheme	range	c_0	χ^2 / DOF
S	V	SMOM	1-5 GeV	0.9280(101)	2.51
			1-4 GeV	0.9512(197)	2.32
			1-3 GeV	0.8479(425)	0.852
S	V	SMOMγ	1-5 GeV	0.9671(91)	1.78
			1-4 GeV	0.9745(219)	1.61
			1-3 GeV	0.8656(615)	0.619
S	A	SMOM	1-5 GeV	0.9131(72)	1.97
			1-4 GeV	0.9570(223)	1.33
			1-3 GeV	0.8724(618)	0.728
S	A	SMOMγ	1-5 GeV	0.9682(76)	2.33
			1-4 GeV	0.9695(233)	1.47
			1-3 GeV	0.8695(618)	0.608
T	V	SMOM	1-5 GeV	1.0288(60)	1.16
			1-4 GeV	1.0397(93)	0.770
			1-3 GeV	1.0879(185)	0.341
T	V	SMOMγ	1-5 GeV	1.0623(24)	1.11
			1-4 GeV	1.0600(56)	1.30
			1-3 GeV	1.0754(139)	0.796
T	A	SMOM	1-5 GeV	1.0069(39)	2.28
			1-4 GeV	1.0512(264)	1.67
			1-3 GeV	1.0361(356)	1.41
T	A	SMOMγ	1-5 GeV	1.0620(28)	0.634
			1-4 GeV	1.0331(43)	1.08
			1-3 GeV	1.0381(110)	1.29

Table 5.4: Results of the μ_0 independent term c_0 from the global fit with (Eq. 5.5).

Statistical and systematic error

Recall that the deviation between the results obtained from the different variants of RI schemes should be regarded as the lattice artifact. Therefore if the deviation is observed, we cannot evaluate the corresponding continuum value without the systematic uncertainties associated with lattice artifact. However, we may reduce the statistical uncertainties by an appropriate choice of the scheme. Among the various combinations of the RI schemes, the SF input and the fit procedure, we find that the choice of the SMOM$_\gamma$ scheme with Z_V^{SF} using the fit ansatz (Esq. 5.5) in the range of $1 < \mu_0 < 4$ [GeV] yield more stable fit so as to get good accuracy of the c_0 value. We finally get

$$Z_S^{\overline{\mathrm{MS}}}(2\ \mathrm{GeV}) = 0.975 \pm 0.022_{\mathrm{stat}} \pm 0.018_{\mathrm{sys}} \qquad Z_T^{\overline{\mathrm{MS}}}(2\ \mathrm{GeV}) = 1.060 \pm 0.006_{\mathrm{stat}} \pm 0.027_{\mathrm{sys}} \tag{5.6}$$

where the first errors denote the statistical one, while the second errors are quoted as the systematic uncertainty that is estimated by the maximum difference between the central values obtained from other combinations.

5.3.4 Renormalized couplings

We finally obtain the results of the nucleon renormalized couplings in the scalar and tensor channels as summarized in Tab .5.5 and Fig. 5.14. In order to the evaluate the final value of the coupling constant, we have to combine the results measured with $t_{\mathrm{sep}} = \{10, 12, 14, 16\}$.

$L^3 \times T$	t_{sep}	g_S	g_T
$128^3 \times 128$	10	$0.802(268)_{\mathrm{stat}}(15)_{\mathrm{sys}}$	$1.155(21)_{\mathrm{stat}}(29)_{\mathrm{sys}}$
	12	$0.889(183)_{\mathrm{stat}}(16)_{\mathrm{sys}}$	$1.087(24)_{\mathrm{stat}}(28)_{\mathrm{sys}}$
	14	$0.790(545)_{\mathrm{stat}}(15)_{\mathrm{sys}}$	$1.044(47)_{\mathrm{stat}}(27)_{\mathrm{sys}}$
	16	$0.945(426)_{\mathrm{stat}}(17)_{\mathrm{sys}}$	$1.060(67)_{\mathrm{stat}}(27)_{\mathrm{sys}}$
$96^3 \times 96$	15	$1.089(398)_{\mathrm{stat}}(20)_{\mathrm{sys}}$	$1.044(59)_{\mathrm{stat}}(27)_{\mathrm{sys}}$

Table 5.5: Summary of renormalized coupling constants

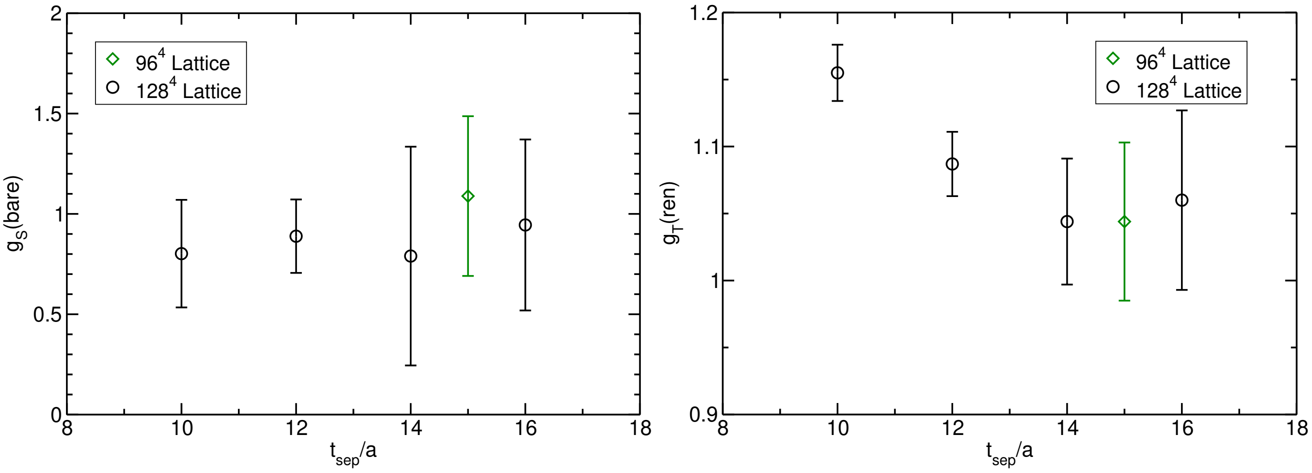

Fig. 5.14: Renormalized coupling constant g_S (left) and g_T (right) with several t_{sep}.

Axial couplings

The axial coupling had been reported in Ref. [67]. The results in all the t_{sep} cases agree with the experimental value $g_A^{\mathrm{expr}} = 1.2732(23)$ [20]. Then, the axial coupling was determined from the combined value with $t_{\mathrm{sep}}/a = \{12, 14, 16\}$ so as to be $g_A = 1.273(24)$ that reaches two percent-level precision and consistent with the experimental value. Recall that the quoted value is not yet taken the continuum limit. That implies that systematical uncertainties due to the lattice discretization are expected to be small in our simulations. Therefore, it is expected that the present calculations in other channels also accurately predict the other nucleon couplings.

Scalar couplings

As similar as the case of DWFs the statistical uncertainties of the scalar couplings are much larger than those of the other coupling constant. However the measured values are consistent with each other, this implies that the excited state contamination seems to be negligible within the current statistical precision. We then get the final estimation from combined value with $t_{\mathrm{sep}} = \{12, 14, 16\}$ as

$$g_S^{\mathrm{ren}} = 0.871 \pm 0.161_{\mathrm{stat}} \pm 0.016_{\mathrm{sys}}. \qquad \text{(PACS10)} \tag{5.7}$$

The scalar coupling calculated with the HPCI configurations is also obtained as

$$g_S^{\mathrm{ren}} = 1.089 \pm 0.398_{\mathrm{stat}} \pm 0.020_{\mathrm{sys}}. \qquad \text{(HPCI)} \tag{5.8}$$

Tensor couplings

The statistical uncertainty of g_T is comparable with that of g_A as well as the case of DWFs. The g_T measured with $t_{\text{sep}} = 10$ is not consistent with other results. Unlike the case of g_S, the measured value with $t_{\text{sep}} = 10$ is highly contaminated from excited states beyond the statistical uncertainties. Therefore, combining the results with $t_{\text{sep}} = \{12, 14, 16\}$, we get

$$g_T^{\text{ren}} = 1.076 \pm 0.021_{\text{stat}} \pm 0.027_{\text{sys}} \qquad \text{(PACS10)} \tag{5.9}$$

We also get the tensor coupling constant from the HPCI configurations,

$$g_T^{\text{ren}} = 1.044 \pm 0.059_{\text{stat}} \pm 0.027_{\text{sys}}. \qquad \text{(HPCI)} \tag{5.10}$$

5.4 Summary

We have calculated the nucleon non-perturbative renormalized iso-vector couplings using two-types of the Wilson-Clover fermions ensembles generated by PACS Collaborations called as PACS10 and HPCI configurations. We finally obtain the results of the nucleon renormalized couplings as below

$$g_S = 0.871(161)_{\text{stat}}(16)_{\text{sys}} \qquad g_T = 1.076(21)_{\text{stat}}(27)_{\text{sys}} \qquad \text{(PACS10)} \tag{5.11}$$

$$g_S = 1.089(398)_{\text{stat}}(20)_{\text{sys}} \qquad g_T = 1.044(59)_{\text{stat}}(27)_{\text{sys}} \qquad \text{(HPCI).} \tag{5.12}$$

Note that both results are calculated at the same lattice spacing. Therefore, we can not take the continuum limit or directly evaluate the discretization error on the results from these simulations with Wilson-clover fermions. As we mentioned previously, we expect that the systematic uncertainties due to the lattice discretization error are small since the axial coupling before taking the continuum limit reaches good agreement with the experimental value at high accuracy, and also the violation of the chiral symmetry detected by c_{A-V} is an order of 10^{-2} which is related to the size of the discretization error.

Chapter 6

Discussion

6.1 Summary of the nucleon couplings

We summarize all obtained results of the isovector coupling constants in both cases of DWFs and the Wilson-clover fermions in Tab. 6.1 and compare our results with the results from other groups in Fig. 6.1. Although we have separately shown the statistical and systematic uncertainties in the previous chapters, we use the combined error which is evaluated by the squared average as $\sigma_{\text{comb}} = \sqrt{\sigma_{\text{stat}}^2 + \sigma_{\text{sys}}^2}$ in this chapter.

In the case of DWFs, simulations are performed with three different fermion masses at each of two different lattice spacings. Since our simulated values of the pion mass range from 290 MeV to 557 MeV, we have evaluated the continuum value of g_A, g_S and g_T at the physical point using the combined chiral-continuum extrapolation method.

On the other hand, the simulations using Wilson-clover fermions are performed with the physical pion mass. Our simulations are carried out only at a single lattice spacing though additional future calculations at two finer lattice spacings are planned. Thus, the systematic error due to the cutoff effects is not yet evaluated.

Especially in the case of tensor couplings, our result is slighly larger than both of two previous results. This difference could be explained by hidden systematic uncertainties in the previous studies:

- Mainz group : Their simulations are performed only in the unphysical regime for the quark masses, corresponding to M_π down to 200 MeV.
- PNDME collaboraion : Their results are obtained by *partially quenched* simulations where the different fermion actions are used for the sea and valence quarks.

On the other hand, our simulation using the PACS10 configurations corresponds to *fully dynamical* one at the physical point.

Type of simulations	g_A	g_S	g_T
Wilson-Clover (PACS)	$1.273(24)_{\text{stat}}$ [67]	$0.871(161)_{\text{stat}}(16)_{\text{sys}}$ $0.871(162)_{\text{comb}}$	$1.076(21)_{\text{stat}}(27)_{\text{sys}}$ $1.076(34)_{\text{comb}}$
Wilson-Clover (HPCI)	$1.163(75)_{\text{stat}}(14)_{\text{ren}}$ [66]	$1.089(398)_{\text{stat}}(20)_{\text{sys}}$ $1.089(399)_{\text{comb}}$	$1.044(59)_{\text{stat}}(27)_{\text{sys}}$ $1.044(65)_{\text{comb}}$
DWF	$1.19(5)_{\text{stat}}$	$0.89(22)_{\text{stat}}$	$1.05(5)_{\text{stat}}$

Table 6.1: Summary for the results of the isovector renormalized couplings obtained in this thesis.

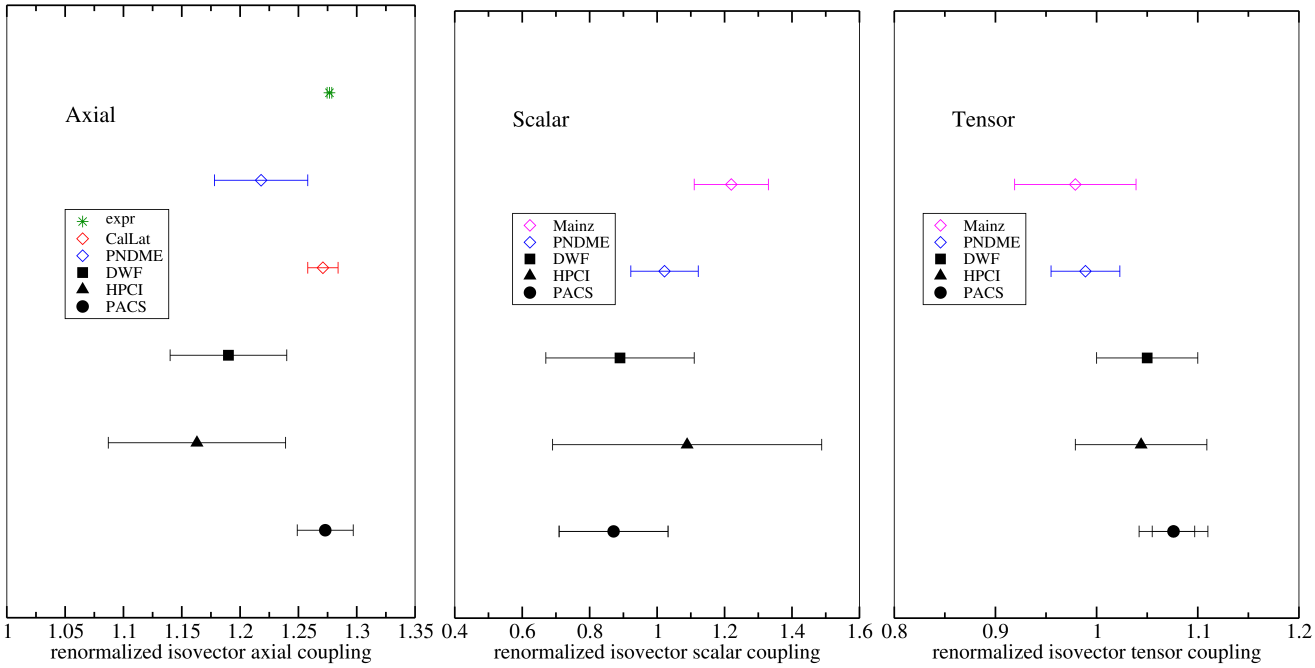

Fig. 6.1: Compared with the results from CalLat collaboration [70], PNDME collaboration [71] and Mainz group [72]. The inner error-bars for the result from the PACS10 ensembles represent the statistical uncertainties while the outer error-bars present the combined uncertainties. Combined uncertainties of our calculation using the Wilson-clover fermions seems to be comparable with the results from other groups. Moreover, we will be able to exclude the further systematic uncertainty after the measurements at the different lattice spacing are done. In the case of the tensor coupling, the systematic uncertainty is comparable with the statistical uncertainty. Therefore we expect the result with smaller uncertainty in our future work.

6.2 Bounds for the new physics parameters

Using our results for the scalar and tensor coupling constants, we estimate the bounds for the new physics parameters:

- $\epsilon_{S,T}$: contributions from scalar (tensor) BSM interaction to the weak decay lagrangian. These parameters are associated with the inverse mass of the undiscovered gauge boson.
- ϵ_R : correction to the right-handed couplings in the weak decay lagrangian.
- $d_{u,d}$: intrinsic EDMs of u and d quark.

Although these parameters can not be directly obtained from lattice QCD simulations, these parameters can be read off from the experimental data with reference to the size of the scalar and tensor coupling constants which are poorly known (experimentally as well as theoretically). Since the uncertainties of ϵ_i and d_q are proportional to the uncertainties of g_S and g_T, the accurate determination of g_S and g_T is highly demanded.

6.2.1 Neutron β-decay and the constraint for the BSM channels

Recall that the ratio $\frac{C_i}{C_V}, i = A, S, T$ can be rewritten with the couplings obtained from lattice QCD simulations $g_i^{\mathrm{QCD}}, i = A, S, T$ [15]. Assuming $1 \gg \epsilon_R + \epsilon_L$,

$$\frac{C_A}{C_V} = -g_A^{\mathrm{QCD}} \left(\frac{1 + \epsilon_L + \epsilon_R - 2\epsilon_R}{1 + \epsilon_L + \epsilon_R} \right) = -g_A^{\mathrm{QCD}} \left(1 - 2\Re\left(\epsilon_R\right) + \mathcal{O}(\epsilon^2) \right) \tag{6.1}$$

$$\frac{C_S}{C_V} = g_S^{\mathrm{QCD}} \epsilon_S \tag{6.2}$$

$$\frac{C_T}{C_A} = \frac{C_T}{C_V} \left(\frac{C_A}{C_V} \right)^{-1} = 4 g_T^{\mathrm{QCD}} \epsilon_T \frac{1}{g_A^{\mathrm{QCD}}} \left(1 + 2\Re\left(\epsilon_R\right) + \mathcal{O}(\epsilon^2) \right) \tag{6.3}$$

As a result, we obtain

$$\begin{pmatrix} \frac{C_A}{C_V} \\ \frac{C_S}{C_V} \\ \frac{C_T}{C_A} \end{pmatrix} = \begin{pmatrix} -g_A^{\mathrm{QCD}} \left(1 - 2\Re\left(\epsilon_R\right) + \mathcal{O}(\epsilon^2) \right) \\ g_S^{\mathrm{QCD}} \epsilon_S \\ 4 g_T^{\mathrm{QCD}} \epsilon_T \times \frac{C_V}{C_A} \end{pmatrix} = \begin{pmatrix} -1.2728 \\ 0.0014 \\ 0.0020 \end{pmatrix} \pm \begin{pmatrix} 0.0017 \\ 0.0012 \\ 0.0022 \end{pmatrix} \tag{6.4}$$

Neglecting the covariance, we estimate the bounds for $\epsilon_i, i = S, T$,

$$\epsilon_S = \begin{cases} 0.00161(138)_{\mathrm{expr}}(30)_{\mathrm{lat}} & \text{for PACS10} \\ 0.00129(110)_{\mathrm{expr}}(47)_{\mathrm{lat}} & \text{for HPCI} \\ 0.00157(135)_{\mathrm{expr}}(39)_{\mathrm{lat}} & \text{for DWFs} \end{cases} \tag{6.5}$$

$$\epsilon_T = \begin{cases} -0.000591(651)_{\mathrm{expr}}(19)_{\mathrm{lat}} & \text{for PACS10} \\ -0.000610(671)_{\mathrm{expr}}(38)_{\mathrm{lat}} & \text{for HPCI} \\ -0.000606(667)_{\mathrm{expr}}(29)_{\mathrm{lat}} & \text{for DWFs} \end{cases} \tag{6.6}$$

and for $\Re\epsilon_R$

$$\Re(\epsilon_R) = \begin{cases} 10^{-5} \times (7.86 \pm 66.8_{\mathrm{expr}} \pm 943_{\mathrm{lat}}) & \text{for PACS10} \\ -0.0472(7)_{\mathrm{expr}}(358)_{\mathrm{lat}} & \text{for HPCI} \\ -0.0299(7)_{\mathrm{expr}}(234)_{\mathrm{lat}} & \text{for DWFs} \end{cases} \tag{6.7}$$

with their 1σ-uncertainties from the experimental data and our results (“expr” and “lat” stand for “experimental” and “lattice” respectively). Currently, the uncertainties of $\epsilon_{S,T}$ are dominated by the experimental error in all cases of DWFs and Wilson-clover fermions and $\epsilon_{S,T}$ are consistent with $\epsilon_{S,T} = 0$ within this precision while the uncertainty from lattice QCD is kept at about 25 % of the central values of $\epsilon_{S,T}$. Needless to say, the further experimental effort is required to draw a firm conclusion.

In the case of g_A, the experiment value is an order more precise than the result from lattice QCD at present. Therefore the uncertainties in ϵ_R are dominated by the uncertainties on g_A measured in lattice QCD.

6.2.2 Tensor couplings and bounds for the quark EDM

Recall that the nucleon EDMs can be expressed in terms of quark EDMs

$$d_p = d_u g_T^u + d_d g_T^d + d_s g_T^s \qquad\qquad d_n = d_u g_T^d + d_d g_T^u + d_s g_T^s, \tag{6.8}$$

neglecting the contribution from the θ-vacuum and the chromo-magnetic coupling. The determination of d_q essentially requires individual values of g_T^u, g_T^d and g_T^s. Although only the isovector couplings are calculated in this thesis, we can estimate the bound for the quark EDM by considering a difference between d_p and d_n which is rewritten as the function of $g_T = g_T^u - g_T^d$

$$d_p - d_n = (d_u - d_d)\left(g_T^u - g_T^d\right) = (d_u - d_d)\, g_T. \tag{6.9}$$

Using the inequality $|d_p - d_n| < |d_p| + |d_n|$ with the experimental bounds for d_p and d_n

$$|d_u - d_d|\, g_T < 2.4 \times 10^{-25} e\text{cm}. \tag{6.10}$$

From the our results of g_T obtained from fully dynamical lattice QCD simulations with DWFs and Wilson-clover fermions, we estimate the 1-σ lower bounds for the tensor charge

$$g_T > 1.04, \qquad \text{for PACS10} \tag{6.11}$$

$$g_T > 0.98, \qquad \text{for HPCI} \tag{6.12}$$

$$g_T > 1.00 \qquad \text{for DWFs} \tag{6.13}$$

Combined with these results, we finally get the following upper bounds

$$|d_u - d_d| < 2.3 \times 10^{-25} e\text{cm} \qquad \text{for PACS10} \tag{6.14}$$

$$|d_u - d_d| < 2.4 \times 10^{-25} e\text{cm} \qquad \text{for HPCI} \tag{6.15}$$

$$|d_u - d_d| < 2.4 \times 10^{-25} e\text{cm} \qquad \text{for DWFs} \tag{6.16}$$

To estimate individual components of g_T^u, g_T^d and g_T^s require calculation of the disconnected contributions of three-point correlation functions, that demand huge computational cost. Therefore, the flavor diagonal tensor charges are not calculated in this thesis. The constraint on the individual quark EDMs will be a future research issue.

Chapter 7

Summary

We have calculated the nucleon isovector couplings g_A, g_S and g_T in fully dynamical lattice QCD simulations using DWFs and Wilson-clover fermions.

In Chap. 4, we show results from 2+1 flavor lattice QCD using DWFs. The simulations are performed at three different quark masses with two different lattice spacings with the same spatial volume of about 2.7 fm lattice. The chiral symmetry is kept manifest in DWFs. Indeed, we observed that the parameter of the chiral symmetry breaking defined by a difference of Z_V and Z_A is close to zero within the statistical uncertainties. The typical size of c_{A-V} is estimated to be about 10^{-4} that should be regarded as the contribution from $\mathcal{O}(a^2)$ lattice artifacts.

We also calculated the renormalization constants for the scalar and tensor using the RI/SMOM scheme as a function of the intermediate scale μ_0 and demonstrated that the renormalization constants are highly affected by the hypercubic lattice artifacts. In other words, the renormalization constants depend not only on a single scale parameter μ_0 but also on hypercubic parameters specified by the choice of the momentum configuration due to breaking of the SO(4) symmetry on the lattice. Therefore, we attempted to eliminate the hypercubic artifact using the subtracting method introduced in Chap. 3 and then found that the χ^2 values of fits are efficiently reduced after removing the hypercubic artifacts. This implies that we can obtain the renormalization constant as the smooth function of μ_0 that enables us to precisely determine the μ_0 independent contribution.

Together with the bare coupling constants, we finally evaluated the renormalized nucleon coupling constants calculated from the relevant ratio of three and two-point correlation functions in the continuum limit at the physical point by combining the chiral-continuum extrapolation. We also read off a size of $\mathcal{O}(a^2)$ lattice artifacts during the extrapolation with the fit ansatz. It is estimated to be an order of about 10^{-2} which is consistent with the canonical estimation of the lattice artifacts. Together with the estimation from c_{A-V}, we finally estimate the size of lattice artifact to be 10^{-4}–10^{-2}.

In Chap. 5, we show results from 2+1 lattice QCD using Wilson-clover fermions. The simulations are performed at the physical point on a $(10.8\ \mathrm{fm})^4$ lattice at a single lattice spacing. The chiral symmetry in Wilson-clover fermions is not manifest. However, we observed that the value of c_{A-V} is estimated to be an order of 10^{-1}–10^{-2} and this implied that the chiral symmetry is efficiently restored in the $\mathcal{O}(a)$-improved Wilson-clover fermions. The size of c_{A-V} is also barely consistent with a rough estimate of $\mathcal{O}(a)$ lattice artifacts that is square of the results of c_{A-V} from DWFs.

In the case of Wilson-clover fermions, we determined the renormalization constants for the scalar and tensor using both of the RI/SMOM and RI/SMOM$_\gamma$ schemes. We also observed that the renormalization constants are less affected by the hypercubic lattice artifacts unlike the case of DWFs. The fact that quark two-point correlation

	g_A	g_S	g_T
PACS	$1.273(24)_{\rm stat}$ [67]	$0.871(161)_{\rm stat}(16)_{\rm sys}$	$1.076(21)_{\rm stat}(27)_{\rm sys}$
HPCI	$1.163(75)_{\rm stat}(14)_{\rm ren}$ [66]	$1.089(398)_{\rm stat}(20)_{\rm sys}$	$1.044(59)_{\rm stat}(27)_{\rm sys}$
DWF	$1.19(5)_{\rm stat}$	$0.89(22)_{\rm stat}$	$1.05(5)_{\rm stat}$

Table 7.1: Measured renormalized coupling constant.

	ϵ_S	ϵ_T	$\Re\left(\epsilon_R\right)$
PACS10	$0.00161(138)_{\rm expr}(30)_{\rm lat}$	$-0.000591(651)_{\rm expr}(19)_{\rm lat}$	$10^{-5} \times (7.86 \pm 66.8_{\rm expr} \pm 943_{\rm lat})$
HPCI	$0.00129(110)_{\rm expr}(47)_{\rm lat}$	$-0.000610(671)_{\rm expr}(38)_{\rm lat}$	$-0.0472(7)_{\rm expr}(358)_{\rm lat}$
DWF	$0.00157(135)_{\rm expr}(39)_{\rm lat}$	$-0.000606(667)_{\rm expr}(29)_{\rm lat}$	$-0.0299(7)_{\rm expr}(234)_{\rm lat}$

Table 7.2: Bounds for $\epsilon_{S,T,R}$.

	bound for quark EDMs
PACS10	$\lvert d_u - d_d \rvert < 2.3 \times 10^{-25} e\mathrm{cm}$
HPCI	$\lvert d_u - d_d \rvert < 2.4 \times 10^{-25} e\mathrm{cm}$
DWF	$\lvert d_u - d_d \rvert < 2.4 \times 10^{-25} e\mathrm{cm}$

Table 7.3: Bounds for d_u and d_d.

functions calculated in Wilson-clover fermions receive the less hypercubic artifacts compared with chiral fermions such as DWFs is also reported in Ref. [50]. Therefore, we neglected the contributions of the hypercubic artifacts. Since we cannot take the continuum limit, unlike the case of DWFs, we examined the scheme dependence as the systematic uncertainties associated with the lattice artifacts. This estimated systematic uncertainty is roughly comparable with a rough estimation of the lattice artifacts converted from the lattice discretization error measured in the DWFs simulations. We finally evaluated the renormalized coupling constants as summarized in Tab. 7.1. We stress that the axial coupling calculated with the PACS10 configurations $g_A = 1.273(24)$ [67] is in good agreement with the experimental value $g_A = 1.2732(23)$ [20]. Recall that the quoted value of g_A is also not yet taken the continuum limit. That implies that systematical uncertainties due to the lattice discretization are expected to be small in our simulations. Therefore, it is expected that the present calculations in other channels also accurately predict the other nucleon couplings. Although all result are barely consistent with the previous results, our result using the PACS10 configuration is slightly larger than both of two previous results especially in the case of the tensor coupling. This difference could be explained by hidden systematic uncertainties in the previous studies. Note that the difference between this work and previous studies was observed thanks to 4%-level precision in the tensor channel. The combined uncertainties of our results are comparable with the results obtained from other groups. Moreover we will be able to reduce uncertainties of our results after taking the continuum limit since their uncertainties are also contributed by the systematic uncertainties associated with the lattice artifacts. Therefore we expect the more accurate results in our future work after all measurements of the nucleon bare coupling constants at the finer lattice spacing will be achieved.

We evaluated the bound for new physics parameters such as $\epsilon_{S,T,R}$ (summarized in Tab. 7.2) and quark intrinsic EDMs $d_{u,d}$ (summarized in Tab. 7.3) by using our numerical results of the scalar and tensor coupling constants. We then found that all of them are consistent with zero.

Especially in the case of $\epsilon_{S,T}$, the uncertainties from the experiment are quite large while the uncertainty from lattice QCD does not exceed the central values. Therefore, the further precise experiments are needed in the case of $\epsilon_{S,T}$. On the other hand, the experimental value of the axial coupling is much more precise than our results. Then the quoted uncertainties of ϵ_R are mostly propagated from lattice QCD our results of g_A. Therefore the more precise determination of g_A in lattice QCD is also desired, however the mass deference between u and d quarks should be taken into account for achievement of sub-percent level accuracy on the coupling constant.

Since we have not calculated the flavor diagonal values of g_T^u, g_T^d and g_T^s, we can not determine the bound for the individual quark EDMs $d_{u,d}$. The calculation of flavor diagonal values of the coupling constants will be needed in the future works.

Acknowledgement

I would like to thank Prof. Shoichi Sasaki for the continuous support of my Ph.D study and fruitful discussion. I also would like to thank the members of PACS Collaboration, especially Prof. Yasumichi Aoki, Prof. Yoshinobu Kuramashi, Dr. Eigo Shintani and Prof. Takeshi Yamazaki. They devoted their time to the discussion with me. This work is done in collaboration with them.

I want to thank staff in the nuclear theory group for encouraging me not to give up writing this thesis. I also thank my colleagues. It was my pleasure to talk with them.

I am supported in part by the Joint Research Program of RIKEN Center for Computational Science (R-CCS) and Graduate Program on Physics for the Universe (GP-PU), Tohoku University. Numerical calculations reported here were partially carried out on the COMA (PACS-IX) system at the CCS, University of Tsukuba, LX406Re-2 at the Cyberscience Center, Tohoku University, and Oakforest-PACS in Joint Center for advanced high performance computing.

Finally, I'm grateful to my family for supporting me during my life.

A

Excited state analysis

A.1 spectral representaion of the hadron two-point function

$$\langle \mathcal{O}_H(t)\mathcal{O}_H^\dagger(0)\rangle = \int dm\rho(m)K(m,t) \tag{A.1}$$

In general, the hadron correlator is rewritten in the convolution of $\rho(m)$ so called by “spectral fucntion” and the appropriate kernel $K(M_i, t)$. The spectral function is regarded as the probability density function of m, mass of the hadron state. Therefore $\rho(m_i)$ is corresponding to the amplitude of m_i-state and the hadron operator [73]. Although $\rho(m)$ is the smooth function of m, the correlator is the discrete function with typically 100 data points. Therefore the determination of the shape of the spectral function $\rho(m)$ is illposed problem.

Replacing the integral for m with the summation of i, the integral equation results in the linear inverse problem.

$$\langle \mathcal{O}_H(t)\mathcal{O}_H^\dagger(0)\rangle = \sum_i K(t, m_i)\rho(m_i) \tag{A.2}$$

where $\rho(m_i)$ is the discretize spectral function with typically $\mathcal{O}(1000)$ data points.

This equation is an illposed inversion problem. In order to extract the spectral function $\rho(m)$ as the smooth function of m from the correlator with no more than 256 data points, the researchers had invented the various methods for a long time. In a modern sense, these methods are based on Bayesian inference.

- Maximum Entropy Method (MEM) [74, 75]
- Bayesian Reconstruction [76]
- Sparse Modeling [77]

A.2 Excited state contamination in the three-point function

Since the ratio of the three-point function and three-point function is independent on the operator insertion time t in the case of $t_{\mathrm{sink}} \gg t, t \gg t_{\mathrm{src}}$, we can evaluate the expectation value of the operator J in terms of the ground state, if the ratio becomes constant as the function of t. Although this method called “plateau” method is the conventional and intutive, the contribution from excited states may be non-negligible. Even if we found the operator insertion time-independent region, we cannot exclude the excited state contribution which is independent on t as shown in the following formula.

$$\langle \mathcal{O}(t_{\rm sink}) J(t) \mathcal{O}^\dagger(t_{\rm src}) \rangle = \sum_{i,j} \langle \mathcal{O}(t_{\rm sink})|j\rangle \langle j|J(t)|i\rangle \langle j|\mathcal{O}(t_{\rm src})\rangle \tag{A.3}$$

$$= \sum_{i,j} \langle \mathcal{O}|j\rangle \langle j|J|i\rangle \langle i|\mathcal{O}\rangle \exp\left[-M_i(t_{\rm sink}-t) - M_j(t-t_{\rm src})\right] \tag{A.4}$$

$$= |\langle N|0\rangle|^2 \langle 0|J|0\rangle e^{-M_0 t_{\rm sep}} + |\langle \mathcal{O}|1\rangle|^2 \langle 1|J|1\rangle e^{-M_1 t_{\rm sep}} + \mathcal{O}(e^{-M_2 t_{\rm sep}})$$

$$+ \sum_{i\neq j} \langle \mathcal{O}|j\rangle \langle j|J|i\rangle \langle i|\mathcal{O}\rangle \exp\left[-M_i(t_{\rm sink}-t) - M_j(t-t_{\rm src})\right] \tag{A.5}$$

$$\to |\langle \mathcal{O}|0\rangle|^2 \langle 0|J|0\rangle e^{-M_0 t_{\rm sep}} + |\langle \mathcal{O}|1\rangle|^2 \langle 1|J|1\rangle e^{-M_1 t_{\rm sep}} + \mathcal{O}(e^{-M_2 t_{\rm sep}}) \tag{A.6}$$

To eliminate the excited state contanimation, we also have to examine the $t_{\rm sep}$-dependence. After taking the $t_{\rm sep} \to \infty$ limit, we finally obtain the matrix element sandwitched by the ground states.

B

Schrödinger functional method

B.1 Formulation

The Schrödinger functional method also give us the powerful formulation to evaluate the the distritution functional with the temporal Dirichlet boundary condition. Since the scale is naturally introduced as the temporal and spatial size of the system, this approach is quite appricatable to the renormalization.

The Schrödinger functional (SF in short) is defined as a transition amplitude between the two states (described in C, C' for the gauge field and ζ, ζ' for the fermion field) in the Schrödinger representaion [78, 79]

$$\langle C', \zeta', x_0 = T | C, \zeta, x_0 = 0 \rangle = \int DAD\overline{\psi}D\psi e^{-S\left[A,\overline{\psi},\psi\right]} \tag{B.1}$$

with boundary conditions for the fields given as

$$A_k(x)|_{x_0=0} = C_k(\vec{x}) \qquad A_k(x)|_{x_0=T} = C'_k(\vec{x}) \tag{B.2}$$

$$P_+\psi(x)|_{x_0=0} = \zeta(\vec{x}) \qquad P_-\psi(x)|_{x_0=T} = \zeta'(\vec{x}) \tag{B.3}$$

$$\overline{\psi}(x)P_-\big|_{x_0=0} = \overline{\zeta}(\vec{x}) \qquad \overline{\psi}(x)P_+\big|_{x_0=T} = \overline{\zeta}'(\vec{x}). \tag{B.4}$$

In the SF formalism, we can evaluate the operators as the same as the path integral formalism,

$$\langle \mathcal{O} \rangle = \int DAD\overline{\psi}D\psi\mathcal{O}\left[A, \overline{\psi}, \psi\right] e^{-S\left[A,\overline{\psi},\psi\right]} / \int DAD\overline{\psi}D\psi e^{-S\left[A,\overline{\psi},\psi\right]} \tag{B.5}$$

with the above boundary conditions.

B.2 Renormalization and improvement

In Ref. [80, 81, 82] they define the correlators

$$f_{XY}(t,s) = -\frac{2}{N_f^2\left(N_f^2-1\right)}\sum_{\vec{x},\vec{y}} f^{abc}f^{cde}\langle O'^d X^a(\vec{x},t)Y^b(\vec{y},s)O^e\rangle \tag{B.6}$$

$$f_X(t) = -\frac{1}{\left(N_f^2-1\right)}\sum_{\vec{x}}\langle X^a(\vec{x},t)O^a\rangle \tag{B.7}$$

$$f_1 = -\frac{1}{\left(N_f^2-1\right)}\langle O'^a O^a\rangle \tag{B.8}$$

$$f_V(t) = -\frac{1}{N_f\left(N_f^2-1\right)}\sum_{\vec{x}} if^{abc}\langle O'^a V_4^b(\vec{x},t)O^c\rangle \tag{B.9}$$

where O, O' are the operators defined in the boundary,

$$O^a = \frac{1}{(L/a)^3}\sum_{\vec{y},\vec{z}}\overline{\zeta}(\vec{y})\gamma_5 T^a\zeta(\vec{z}) \qquad O'^a = \frac{1}{(L/a)^3}\sum_{\vec{y},\vec{z}}\overline{\zeta}'(\vec{y})\gamma_5 T^a\zeta'(\vec{z}) \tag{B.10}$$

and X or Y can be one of the local operators

$$A_4^a(x) = \overline{q}(x)\gamma_4 T^a\gamma_5 q(x) \qquad V_4^a(x) = \overline{q}(x)\gamma_4 T^a\gamma_5 q(x) \qquad P^a(x) = \overline{q}(x)\gamma_5 T^a q(x). \tag{B.11}$$

Using above correlators, the renormalization constants are determined by

$$Z_A = \sqrt{\tilde{Z}_A(2T/3)} \qquad \tilde{Z}_A(t) = f_1\left[f_{AA}(t,T/3) - 2m_f f_{PA}(t,T/3)\right]^{-1} \tag{B.12}$$

$$Z_V = \sqrt{\tilde{Z}_V(T/2)} \qquad \tilde{Z}_V(t) = \frac{f_1}{f_V(t)} \tag{B.13}$$

$$Z_P = \sqrt{\tilde{Z}_P(T/2)} \qquad \tilde{Z}_P(t) = \frac{\sqrt{3f_1}}{f_P(t)} \tag{B.14}$$

with the vanishing fermion mass m_f. This method can be easily expanded to the tensor current [83]. The improvement factors c_i for the currents are also determined using the Schrödinger functional method [35].

C

Perturbation theory

C.1 α_s determination

$$\frac{d\ln\alpha_s}{d\ln\mu^2} = \beta(\alpha_s), \qquad \beta(\alpha_s) = \sum_{i=0}\beta_i\left(\frac{\alpha_s}{4\pi}\right)^{i+2} \tag{C.1}$$

where $\alpha_s = \frac{g_s^2}{4\pi^2}$. The renormalization group equation leads

$$2\ln\frac{\mu}{\mu'} = \int_{\alpha_s(\mu')}^{\alpha_s(\mu)}\frac{d\alpha_s}{\beta(\alpha_s)}. \tag{C.2}$$

α_s at the scale of μ is obtained by solving for $\alpha_s(\mu)$ with $\alpha_s(\mu')$ as the input. The reference values of α_s at the scale of the mass of Z and τ are given by

$$\alpha_s^{N_f=5}(M_Z) = 0.1181 \pm 0.0011 \tag{C.3}$$

$$\alpha_s^{N_f=3}(M_\tau) = 0.325 \pm 0.0015 \tag{C.4}$$

in [20].

Imposing the boundary conditions as

$$\alpha_s^{N_f=5}(m_b) = \alpha_s^{N_f=4}(m_b) \tag{C.5}$$

$$\alpha_s^{N_f=4}(m_c) = \alpha_s^{N_f=3}(m_c) \tag{C.6}$$

at the scale of m_b, m_c corresponding to the bottom and charm threshold, we obtain the $\alpha^{N_f=3}$ at any scale.

C.2 Evolution factor

The anomalous dimension of the bilinear current $\overline{\psi}\Gamma\psi$ is defined as

$$\frac{d\ln Z_\Gamma}{d\ln\mu^2} = \gamma_\Gamma \tag{C.7}$$

$$\frac{d\ln Z_\Gamma}{d\alpha_s}\frac{d\alpha_s}{d\ln\mu^2} = \frac{d\ln Z_\Gamma}{d\alpha_s}4\pi\beta(\alpha_s) = \gamma_\Gamma \tag{C.8}$$

which can be expanded in the terms of α_s,

$$\gamma_\Gamma = -\sum_{i=1} \gamma_i \left(\frac{\alpha_s}{4\pi}\right)^i . \tag{C.9}$$

By solving the integral equation

$$\int d \ln Z_\Gamma = \int d\frac{\alpha_s}{4\pi} \beta(\alpha_s)^{-1} \gamma_\Gamma \tag{C.10}$$

where

$$\begin{aligned} \frac{\gamma_\Gamma}{\beta} &= \frac{1}{\beta_0}\gamma_1 \left(\frac{\alpha_s}{4\pi}\right)^{-1} \\ &+ \frac{1}{\beta_0}\left(\gamma_2 - \frac{\gamma_1\beta_1}{\beta_0}\right)\left(\frac{\alpha_s}{4\pi}\right)^0 \\ &+ \frac{1}{\beta_0}\left(\gamma_3 - \frac{\gamma_2\beta_1}{\beta_0} - \frac{\beta_2\gamma_1}{\beta_0} + \frac{1}{\beta_0}\frac{\beta_1^2\gamma_1}{\beta_0^2}\right)\left(\frac{\alpha_s}{4\pi}\right)^1 + \mathcal{O}({\alpha_s}^2) \end{aligned} \tag{C.11}$$

we obtain the running factor

$$\begin{aligned} \frac{Z_\Gamma^{\overline{\mathrm{MS}}}(2\mathrm{GeV})}{Z_\Gamma^{\overline{\mathrm{MS}}}(\mu)} &= \left(\frac{\alpha_s(2\mathrm{GeV})}{\alpha_s(\mu)}\right)^{\frac{\gamma_1}{\beta_0}} \exp\left(\frac{\alpha_s(2\mathrm{GeV})}{4\pi} - \frac{\alpha_s(\mu)}{4\pi}\right)^{\left\{\frac{\gamma_2}{\beta_0} - \frac{\gamma_1}{\beta_0^2}\beta_1\right\}} \\ \times \exp\left\{\left(\frac{\alpha_s(2\mathrm{GeV})}{4\pi}\right)^2 - \left(\frac{\alpha_s(\mu)}{4\pi}\right)^2\right\}^{\frac{1}{2}\left\{\frac{\gamma_3}{\beta_0} - \frac{\gamma_2\beta_1}{\beta_0^2} - \frac{\beta_2\gamma_1}{\beta_0^2} + \frac{\beta_1^2\gamma_1}{\beta_0^3}\right\}} &\times \exp \mathcal{O}({\alpha_s}^3). \end{aligned} \tag{C.12}$$

The five-loop calculation of β-function is available in [84]. The anomalous dimensions for the current scalar [85] and the tensor current [86] are also available.

D

Singular Value Decomposition

The singular value decomposition (SVD) is the generalized eigenvalue decomposition which is only appliable to a square matrix. A complex valued $i \times j$ matrix A can be decomposed into a product of matrices

$$\mathrm{A} = \mathrm{U}\mathrm{S}\mathrm{V}^{\dagger} \tag{D.1}$$

where

$$\mathrm{U} = \big(\mathbf{u}_1, \cdots, \mathbf{u}_{\min(i,j)}\big) \qquad \mathbf{u}_a^{\dagger}\mathbf{u}_b = \delta_{ab} \tag{D.2}$$

$$\mathrm{S} = \mathrm{diag}(\lambda_1, \cdots, \lambda_{\min(i,j)}) \qquad \lambda_k > \lambda_{k+1} \tag{D.3}$$

$$\mathrm{V} = \big(\mathbf{v}_1, \cdots, \mathbf{v}_{\min(i,j)}\big) \qquad \mathbf{v}_a^{\dagger}\mathbf{v}_b = \delta_{ab}. \tag{D.4}$$

$$\mathrm{A} = \sum_{k=1}^{\min(i,j)} \mathbf{u}_k \lambda_k \mathbf{v}_k^{\dagger} \tag{D.5}$$

D.1 Low-rank approxiamation and criterions

N-rank approximation of A can be given by

$$\tilde{\mathrm{A}} = \sum_{k=1}^{N} \mathbf{u}_k \lambda_k \mathbf{v}_k^{\dagger}. \tag{D.6}$$

There are two criterions of determinating N.

D.1.1 Tolerance

One of the criterions is that λ_k is set to be 0 if $\lambda_k < \epsilon$. If ϵ is enough small, the residual squared is also small.

$$\|\tilde{\mathrm{A}} - \mathrm{A}\|^2 = \sum_{k=N+1} \lambda_k^2 \sim \epsilon^2 \tag{D.7}$$

D.1.2 Contribution rate

The residual squared is obtained from

$$||\tilde{\mathrm{A}} - \mathrm{A}||^2 = \sum_{k=N+1} \lambda_k^2 = D(N). \tag{D.8}$$

Therefore $D(N)$ indicates how deviated the approximated matrix from the original matrix. The cumulative contribution rate (CCR) which is a criterion of approximation is defined as

$$\frac{D(0) - D(N)}{D(0)} = \begin{cases} 0 & N = 0 \\ 1.0 & N = \min(i, j) \\ x; 0 < x < 1.0 & otherwise \end{cases} . \tag{D.9}$$

if N is set to be 0, the deviation is maximized then $D(0) = \|A\|^2$. So CCR describe the rate of the completeness of our approximation. if N is chosen so that the CCR is above 0.9, the aprroximation matrix and original matrix agree for the percentage of no less than 90.

The SVD decomposition also give a reasonable way to solve an ill-conditioned linear equation by inverting the approximated matrix. The inversion of the approximation matrix corresponds to Moore-Penrose generalized inverse matrix.

Reference

[1] A. Romer, Am. J. Phys. **65**, 707 (1997).

[2] A. Czarnecki, W. J. Marciano and A. Sirlin, Phys. Rev. Lett. **120**, 202002 (2018), [1802.01804].

[3] V. Cirigliano, S. Gardner and B. R. Holstein, Prog. Part. Nucl. Phys. **71**, 93 (2013).

[4] A. Courtoy, S. Baeßler, M. González-Alonso and S. Liuti, Phys. Rev. Lett. **115**, 162001 (2015), [1503.06814].

[5] M. González-Alonso and J. Martin Camalich, Phys. Rev. Lett. **112**, 042501 (2014), [1309.4434].

[6] B. Yoon *et al.*, Phys. Rev. D **95**, 074508 (2017).

[7] N. Hasan *et al.*, Phys. Rev. D **99**, 114505 (2019).

[8] C. Alexandrou *et al.*, Phys. Rev. D **95**, 114514 (2017), [1703.08788].

[9] S. Dürr, PoS LATTICE **2005**, 021 (2006), [0509026].

[10] S. R. Sharpe, PoS LATTICE **2006**, 022 (2006), [0610094].

[11] S. Aoki *et al.*, 1902.08191.

[12] S. Weinberg, Phys. Rev. **112**, 1375 (1958).

[13] T. Bhattacharya *et al.*, Phys. Rev. D **85**, 054512 (2012), [1110.6448].

[14] T. Lee and C. Yang, Phys. Rev. **104**, 254 (1956).

[15] M. González-Alonso, O. Naviliat-Cuncic and N. Severijns, Prog. Part. Nucl. Phys. **104**, 165 (2019), [1803.08732].

[16] M. Anselmino *et al.*, Nucl. Phys. B - Proc. Suppl. **191**, 98 (2009).

[17] I. Bedlinskiy *et al.*, Phys. Rev. Lett. **109**, 112001 (2012).

[18] C. Adolph *et al.*, Phys. Lett. B **736**, 124 (2014).

[19] V. M. Belyaev, B. L. Ioffe and Y. I. Kogan, Phys. Lett. B **151**, 290 (1985).

[20] M. Tanabashi *et al.*, Phys. Rev. D **98**, 030001 (2018).

[21] A. Airapetian *et al.*, Phys. Rev. D **71**, 1 (2005), [0407032].

[22] C. A. Baker *et al.*, Phys. Rev. Lett. **97**, 131801 (2006), [0602020].

[23] E. Farhi, V. V. Khoze and R. Singleton, Phys. Rev. D **47**, 5551 (1993).

[24] R. Martínez, M. A. Pérez and N. Poveda, Eur. Phys. J. C **53**, 221 (2008).

[25] M. Srednicki, *Quantum Field Theory* (Cambridge University Press, 2007).

[26] P. Weisz and R. Wohlert, Nucl. Phys. B **236**, 397 (1984).

[27] M. Lüscher and P. Weisz, Commun. Math. Phys. **97**, 59 (1985).

[28] Y. Iwasaki, 1111.7054.

[29] K. Symanzik, Nucl. Phys. B **226**, 187 (1983).

[30] S. Chandrasekharan and U. J. Wiese, Prog. Part. Nucl. Phys. **53**, 373 (2004), [0405024].

[31] B. Sheikholeslami and R. Wohlert, Nucl. Phys. B **259**, 572 (1985).

[32] S. Aoki and Y. Kuramashi, Phys. Rev. D **68**, 094019 (2003), [0306015].

[33] M. Lüscher, S. Sint, R. Sommer, P. Weisz and U. Wolff, Nucl. Phys. B **491**, 323 (1997).

[34] S. Sint and P. Weisz, Nucl. Phys. B - Proc. Suppl. **63**, 856 (1998).

[35] M. Lüscher and P. Weisz, Nucl. Phys. B **479**, 429 (1996).

[36] Y. Taniguchi and A. Ukawa, Phys. Rev. D **58**, 114503 (1998), [9806015].

[37] C. Morningstar and M. Peardon, Phys. Rev. D **69**, 054501 (2004), [0311018].

[38] H. B. Nielsen and M. Ninomiya, Nucl. Phys. B **185**, 20 (1981).

[39] K. Jansen, Phys. Rep. **273**, 1 (1996), [9410018].

[40] D. B. Kaplan, Phys. Lett. B **288**, 342 (1992).

[41] T. Blum *et al.*, Phys. Rev. D **69**, 074502 (2004), [0007038].

[42] N. Metropolis, A. W. Rosenbluth, M. N. Rosenbluth, A. H. Teller and E. Teller, J. Chem. Phys. **21**, 1087 (1953).

[43] K. Sasaki and S. Sasaki, Phys. Rev. D **72**, 034502 (2005), [0503026].

[44] F. Fucito, G. Martinelli, C. Omero, G. Parisi and R. Petronzio, Nucl. Phys. B **210**, 407 (1982).

[45] G. Martinelli, C. Pittori, C. T. Sachrajda, M. Testa and A. Vladikas, Nucl. Phys. B **445**, 81 (1995), [9411010].

[46] Y. Aoki *et al.*, Phys. Rev. D **78**, 054510 (2008).

[47] C. Sturm *et al.*, Phys. Rev. D **80**, 014501 (2009), [0901.2599].

[48] L. G. Almeida and C. Sturm, Phys. Rev. D **82**, 054017 (2010), [1004.4613].

[49] P. Boucaud *et al.*, Phys. Lett. B **575**, 256 (2003), [0307026].

[50] P. Boucaud *et al.*, Phys. Rev. D **74**, 034505 (2006).

[51] B. Blossier *et al.*, Phys. Rev. D **91**, 114507 (2015).

[52] D. Becirevic *et al.*, Phys. Rev. D **60**, 094509 (1999).

[53] C. Roiesnel, J. P. Leroy, J. Micheli, O. Pène and J. Rodríguez-Quintero, Phys. Rev. D **61**, 14508 (2000).

[54] Y. Aoki *et al.*, Phys. Rev. D **83**, 074508 (2011).

[55] S. Sasaki, Phys. Rev. D **96**, 074509 (2017), [1708.04008].

[56] S. Sasaki, K. Orginos, S. Ohta and T. Blum, Phys. Rev. D **68**, 054509 (2003), [0306007].

[57] C. Alexandrou, S. Güsken, F. Jegerlehner, K. Schilling and R. Sommer, Nucl. Phys. B **414**, 815 (1994).

[58] C. Allton *et al.*, Phys. Rev. D **78**, 114509 (2008), [0804.0473].

[59] T. Yamazaki *et al.*, Phys. Rev. D **79**, 114505 (2009), [0904.2039].

[60] Y. Aoki *et al.*, Phys. Rev. D **82**, 014501 (2010).

[61] C. Alexandrou, G. Koutsou, J. W. Negele, Y. Proestos and A. Tsapalis, Phys. Rev. D **83**, 014501 (2011), [1011.3233].

[62] W. Detmold, W. Melnitchouk and A. W. Thomas, Eur. Phys. J. A **18**, 269 (2003).

[63] N. Yamanaka, S. Hashimoto, T. Kaneko and H. Ohki, Phys. Rev. D **98**, 054516 (2018).

[64] K. I. Ishikawa *et al.*, Phys. Rev. D **99**, 014504 (2019), [1807.06237].

[65] K. I. Ishikawa *et al.*, PoS LATTICE **2015**, 075 (2015), [1511.09222].

[66] K. I. Ishikawa *et al.*, Phys. Rev. D **98**, 074510 (2018), [1807.03974].

[67] E. Shintani, K.-I. Ishikawa, Y. Kuramashi, S. Sasaki and T. Yamazaki, Phys. Rev. D **99**, 014510 (2019), [1811.07292].

[68] Y. Taniguchi, PoS LATTICE **2012**, 236 (2013), [1303.0104].

[69] C. C. Chang *et al.*, Nature **558**, 91 (2018), [1805.12130].

[70] R. Gupta *et al.*, Phys. Rev. D **98**, 034503 (2018), [1806.09006].

[71] T. Harris *et al.*, Phys. Rev. D **100**, 034513 (2019), [1905.01291].

[72] H. Ohno *et al.*, Phys. Rev. D **84**, 094504 (2011), [1104.3384].

[73] P. M. Cardoso Dias and A. Shimony, Adv. Appl. Math. **2**, 172 (1981).

[74] M. Asakawa, Y. Nakahara and T. Hatsuda, Prog. Part. Nucl. Phys. **46**, 459 (2001).

[75] Y. Burnier and A. Rothkopf, Phys. Rev. Lett. **111**, 182003 (2013).

[76] J. Otsuki, M. Ohzeki, H. Shinaoka and K. Yoshimi, Phys. Rev. E **95**, 061302 (2017), [1702.03056].

[77] M. Lüscher and P. Weisz, Nucl. Phys. B **384**, 168 (1992), [9207009v1].

[78] S. Sint, Nucl. Phys. B - Proc. Suppl. **42**, 835 (1995), [9312079].

[79] M. Della Morte, R. Hoffmann and R. Sommer, JHEP **07**, 689 (2005), [0503003].

[80] M. Della Morte, R. Sommer and S. Takeda, Phys. Lett. B **672**, 407 (2009), [0807.1120].

[81] K. I. Ishikawa *et al.*, PoS LATTICE **2015**, 271 (2016), [1511.08549].

[82] L. Chimirri *et al.*, PoS LATTICE **2019**, 212 (2019), [1910.06759].

[83] P. A. Baikov, K. G. Chetyrkin and J. H. Kühn, Phys. Rev. Lett. **118**, 082002 (2017), [1606.08659].

[84] P. A. Baikov, K. G. Chetyrkin and J. H. Kühn, JHEP **10**, 076 (2014), [1402.6611].

[85] J. A. Gracey, Phys. Lett. B **488**, 175 (2000), [0007171v1].